DISSERTATION

SPATIAL SIMULATION OF SNOW AND FROZEN GROUND USING A MODIFIED TEMPERATURE-BASED MODEL

Submitted by

Michael Lee Follum

Department of Civil and Environmental Engineering

In partial fulfillment of the requirements

For the Degree of Doctor of Philosophy

Colorado State University

Fort Collins, Colorado

Fall 2018

Doctoral Committee:

Advisor: Jeffrey Niemann

Steven Fassnacht
Pierre Julien
Stephanie Kampf

Copyright by Michael Lee Follum 2018

All Rights Reserved

ABSTRACT

SPATIAL SIMULATION OF SNOW AND FROZEN GROUND USING A MODIFIED TEMPERATURE-BASED MODEL

Volume and timing estimates of snowpack and subsequent streamflow are vital for water management and flood forecasting in snow-dominated regions. Numerical models are often employed to estimate the depth of snowpack and presence of frozen ground for assessment of the resulting streamflow. Air temperature based models, such as temperature-index (TI) snow models and degree-day (DD) frozen ground models, are commonly used due to their simplicity and low data requirements. However, because air temperature (a surrogate for available energy) is the main forcing variable, the snowpack and frozen ground in TI and DD models vary spatially based only on elevation. The overall objective of this research is to improve the representation of spatial variations in snowpack and frozen ground within watersheds in order to improve streamflow simulations. To accomplish this goal, this study replaces air temperature in a TI snow model and a DD frozen ground model with a proxy temperature for available energy. The proxy temperature is calculated using a simplified radiation energy balance (requiring precipitation, air temperature, and cloud cover data) that accounts for spatial heterogeneity in both shortwave and longwave radiation due to topography and vegetation. The modified-TI model, referred to as the Radiation-derived Temperature-Index (RTI) snow model, is tested at Senator Beck basin (SBB) in Colorado and at Sleepers River Experimental Watershed (SREW) in Vermont. The RTI model outperforms a pre-existing TI model in simulation of snow water equivalent (SWE) and improves simulation of snow covered area (SCA) at both SBB and SREW. The improvements in snow simulation using the RTI model also improve the streamflow simulation at SBB. The modifications to the DD model, referred to as the modified Continuous Frozen Ground Index (modCFGI) model, also account for insulation of soil by ground cover and simulate frost depth. When tested at SREW, the modCFGI model more accurately captures the variations in frozen ground between the sites, inter-annual variations in frozen ground depths at a given site, and the occurrence of frozen ground than the pre-existing Continuous Frozen Ground Index model. Overall, the modifications made to the snow and frozen ground methods increase the spatial accuracy without requiring much additional data. The RTI and modCFGI methods are also readily transferrable to other hydrologic models.

ACKNOWLEDGEMENTS

This project was funded by the Flood and Coastal Research Program at the U.S. Army Corps of Engineers, Engineering Research and Development Center, Coastal and Hydraulics Laboratory in Vicksburg, Mississippi.

DEDICATION

To Tara and Adelyn.

TABLE OF CONTENTS

LIST OF TABLES

LIST OF FIGURES

CHAPTER 1. INTRODUCTION

1.1 Background

Accurate estimation of snow and frozen ground are important in hydrology. Streamflow generated by snowmelt constitutes approximately 70% of the annual runoff in the western United States, providing 50-80% of the annual downstream water supply (Wahl, 1992). Seasonal frozen ground (also known as frozen soil and soil frost) occurs over approximately 55% of the exposed land surface in the Northern Hemisphere (Zhang et al., 2004) and can affect runoff production by reducing the infiltration capacity of the soils (Bayard et al., 2005; Dunne and Black, 1971; Stähli et al., 1999). This increase in runoff production can lead to severe flood events, as experienced in New England (Diebold, 1938), the upper Midwest (Cherkauer and Lettenmaier, 1999; Stoner et al., 1993), and the Pacific Northwest of the United States (Johnson and McArthur, 1973).

The spatial pattern of snow and frozen ground are also important. The shape, peak, and duration of the snowmelt hydrograph are often controlled by the spatial pattern of the snowpack (Luce et al., 1998; Pomeroy et al., 2009). The large-scale distribution of snowpack is often controlled by elevation, land cover, and slope/aspect (Fassnacht et al., 2017; Jost et al., 2007). The spatial distribution of frozen ground is highly-variable temporally and spatially (Campbell et al., 2010; Stähli, 2017), which affects the amount and type of runoff (Wilcox et al., 1997). Dunne and Black (1971) found that almost 50% of the meltwater leaving three research plots within Sleepers River Experimental Watershed (SREW), Vermont, as overland flow is due to a thin layer of non-uniform frozen ground. Although the frozen ground layer is thin, it affects the diurnal fluctuations of streamflow in the 0.47 km^2 catchment. Using frost tube measurements at over 35 locations within SREW during a 15 year period, Shanley and Chalmers (1999) found that frost depths have considerable interannual variation (between 7 cm and 39 cm at one test location). They also found that frost depth depends on land cover type, with open field sites having the deepest frost depth, followed by coniferous forest, mixed canopy forest, and deciduous forest sites.

The spatial patterns of snow and frozen ground are controlled by fundamental laws of mass (water) and energy. Snowfall occurs when ice crystals in clouds combine, become heavy, and fall towards the ground. Depending on atmospheric conditions (air temperature and humidity) some of the snowfall melts or sublimates before reaching the land surface. The snow that does fall to the land surface can be intercepted by vegetation canopy (up to 60% of midwinter cumulative snowfall in cold boreal forests (Pomeroy et al., 1998)) where it generally has higher rates of sublimation than snowpack on the ground surface (Pomeroy and Schmidt, 1993; Pomeroy and Gray, 1995; Harding and Pomeroy, 1996) due to higher wind speeds and exposure to sunlight (Lundberg and Halldin, 1994). Snow that lands on the ground surface accumulates and is subject to redistribution by the wind.

The snowpack has an internal temperature that can vary considerably in time and between the ground interface and the atmosphere interface. In a USACE (1956) study, an internal snowpack temperature fell below -8°C for a California snowpack, while Bergen (1968) measured an internal snowpack temperature of -24°C in a Colorado snowpack. Melting of the snowpack occurs once the snowpack becomes isothermal (snowpack has a temperature of 0°C). The amount of energy required to bring the snowpack to an isothermal state is often referred to as heat deficit or cold content. After a snowpack becomes isothermal, additional energy from the ground or atmosphere can melt the snowpack. As shown in Figure 1, the energy fluxes (Q) affecting the snowpack include net longwave radiation ($Q_{longwave}$), net shortwave radiation ($Q_{shortwave}$), advected heat removed by meltwater (Q_{melt}), advected heat from precipitation ($Q_{precipitation}$), ground heat flux (Q_{ground}), latent heat flux (Q_{latent}), and sensible heat flux ($Q_{sensible}$). Turbulent heat fluxes (Q_{latent} and $Q_{sensible}$) can be dominant in some watersheds (e.g., warm temperate mountain climates (Sade et al., 2014)), especially in areas susceptible to sublimation.

The convective transfer of moisture Q_{latent} and thermal energy $Q_{sensible}$ between the atmosphere and snowpack can also be dominant during rain-on-snow events (DeWalle and Rango, 2008). However, most studies indicate that net radiation (combination of $Q_{longwave}$ and $Q_{shortwave}$) is the primary source of energy for reducing the cold content of the snowpack and inducing melt (Aguado, 1985), with $Q_{shortwave}$ often the dominant source of energy (DeWalle and Rango, 2008; Sicart et al., 2006). Locations with higher $Q_{shortwave}$ also tend to have higher sublimation rates (Gustafson et al., 2010). Topography (Bloschl et al., 1991; Kirnbauer et al., 1994) and vegetation (Musselman et al., 2008; Rinehart et al., 2008) influence the spatial heterogeneity of the snowpack because they affect the net radiation balance. Energy available to melt the snowpack from $Q_{longwave}$ is most closely related to air temperature (Ohmura, 2001), so changes in air temperature with elevation affect the net radiation balance. Vegetation canopy emits longwave radiation and therefore also affects $Q_{longwave}$ (DeWalle and Rango, 2008). $Q_{shortwave}$ is associated with solar radiation, so shading from clouds, vegetation canopy, and surrounding terrain affects the net radiation balance. The solar radiation emitted from the sun rarely strikes the land surface at a perpendicular angle, so the slope and aspect of the terrain also affect $Q_{shortwave}$ (Duffie and Beckman, 1980). The albedo of the snowpack further reduces the amount of $Q_{shortwave}$ absorbed by the snowpack.

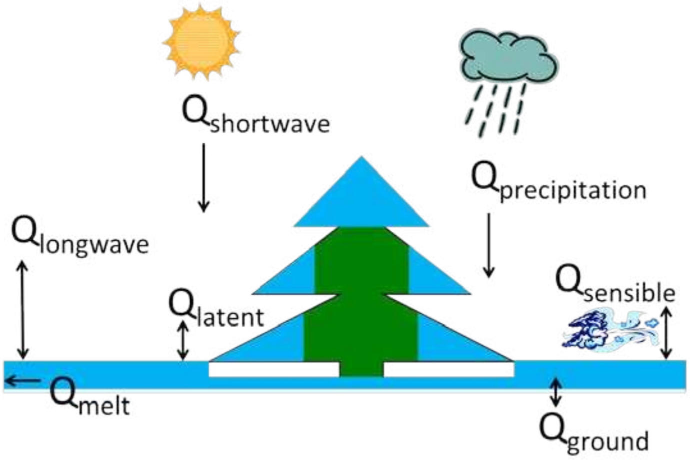

Figure 1. Diagram of the energy fluxes (Q) affecting the snowpack.

Seasonal frozen ground occurs when sufficient energy is lost from the soil and the moisture within the soil becomes pore ice. Energy and mass (water) fluxes between the soil, atmosphere, ground cover, and snowpack (if present) are complex (Dun et al., 2010; Kennedy and Sharratt, 1998; Lin and McCool, 2006). The energy available from the atmosphere to thaw the soil is affected by the insulating properties of the snowpack (Pearson, 1920; Willis et al., 1961). A deep snowpack can insulate the ground and prevent freezing. Open areas often exhibit greater depths of frozen ground than forested areas (Diebold, 1938; Kienholz, 1940; Shanley and Chalmers, 1999) because open areas receive more $Q_{shortwave}$, which melts the snow faster. This reduction in snow pack reduces the insulation of the ground (Campbell et al., 2010), subjecting the ground to greater radiational cooling at night and cold air temperatures (Willis et al., 1961). Ground cover (e.g. vegetation, woody debris, and leaf litter) also provides insulation to the ground (Brown, 1966; Diebold, 1938; Fahey and Lang, 1975; Sartz, 1973). MacKinney (1929) found that insulation from ground cover can reduce the depth of frost penetration by 40% at a test site in Connecticut. Shading of $Q_{shortwave}$ also impacts the depth of frozen ground. For example, Wilcox et al. (1997) found that ground shaded by trees has greater frost depth than surrounding areas for a ponderosa pine hillslope in northern New Mexico. The aspect of a hillslope (which affects $Q_{shortwave}$) has also been shown to cause differences in timing of frozen ground, with more rapid soil freezing and slower thawing on north-facing slopes in a research watershed in China (Zhenniang et al., 1994). Soil properties, including thermal conductivity (Farouki, 1981; Johansen, 1977) and soil moisture (Fox, 1992), also affect the presence and depth of frozen ground. Willis et al. (1961) observed that dry soils tend to freeze faster and deeper than wet soils in the Fall. This difference occurs largely because the heat capacity of water is relatively high, requiring more energy extraction to occur before a wet soil can freeze.

Water managers, hydrologists, and engineers commonly utilize numerical models to estimate the volume of snow water equivalent (SWE), determine the presence of frozen ground, and estimate the resulting streamflow in order to plan for operations of reservoirs and other water control structures. Accurate estimation of the spatial distribution of snow and frozen ground within hydrologic models is difficult due to the complex energy and mass interactions and data limitations. Energy-balance approaches can provide accurate spatial distributions of snow and frozen ground, but they have large data requirements (e.g., wind speed, relative humidity, and short- and long-wave radiation) that are not available at many sites and not at the necessary spatial resolution where they are available. Air temperature based snow and frozen ground models are commonly used within hydrologic models due to their simplicity and smaller data requirements (primarily temperature and precipitation). Two issues arise from using air temperature as the primary source of energy. First, air temperature is typically estimated throughout the basin based on the local elevation and specified lapse rate, thus limiting the spatial variability of available energy to a relationship with elevation, which does not account for land cover or other topographic attributes such as slope, aspect, and topographic shading. Second, air temperature is most related to $Q_{longwave}$, whereas $Q_{shortwave}$ is often the dominant source of energy at the snow surface. Additionally, air temperature based frozen ground models (referred to as degree-day (DD) models) typically do not account for the insulating effects of the ground cover, which has shown to often control the presence and depth of frozen ground (MacKinney, 1929). DD models typically vary depth of frozen ground with elevation (through temperature-elevation relationship), but Stähli (2017) found no clear connection between elevation and the presence of frozen ground at test sites in the Swiss pre-alpine zone.

1.2 Objectives

The overall goal of this research is to improve the spatial representation of available energy at the snow surface and ground surface using limited forcing data, thus resulting in improved spatial simulation of snow, frozen ground, and the resultant streamflow. To achieve this goal, an existing air temperature based snow model (referred to as temperature-index (TI) model) and an existing DD frozen ground model will be modified to better account for the spatial heterogeneity of available energy while preserving the strengths of the TI and DD approaches, particularly their small data requirements and widely-used mathematical structure. The GSSHA model is used as the fully-distributed hydrologic model to test the modified snow and frozen ground models and to test if those modifications lead to improved hydrograph simulations.

This dissertation includes three journal papers (Chapters 2, 3, and 4) that accomplish the three main tasks of this research. Each of the three journal papers is briefly described below:

(1) Modify an existing TI model to better account for spatial heterogeneity of energy and improve simulated snowpack patterns. A new radiation-derived temperature index (RTI) approach is presented that uses a spatially-varying proxy temperature in place of air temperature within the commonly used SNOW-17 model (a TI model) (Anderson 1973; 2006). The RTI is derived from a radiation balance (requiring precipitation, air temperature, and cloud cover data) and includes spatial heterogeneity in both shortwave and longwave radiation. Thus, the RTI accounts for more local variation in the available energy than air temperature alone. The RTI model in GSSHA is tested at the Senator Beck basin (SBB) in southwestern Colorado where observations for SWE and LandSat-derived images of snow covered area (SCA) are available.

(2) Determine if use of the RTI snow model improves streamflow estimation when used within a distributed hydrologic model. Streamflow simulations are compared between the TI and RTI snow models when coupled within a process-based and fully-distributed hydrologic model. This research tests if improved SCA simulations using the RTI model result in improved streamflow simulations. This chapter also tests the TI and RTI model performance (snow and flow simulations) when they are calibrated to point SWE measurements or SCA images. The models account for vertical and lateral flow through the snowpack, overland flow, and flow through the channel network. Flow simulations are tested for 6 water years at SBB.

(3) Modify existing DD model to better account for spatial heterogeneity of energy to improve spatial frozen ground simulation. The widely-used Continuous Frozen Ground Index (CFGI) model (a DD model) (Molnau and Bissell, 1983) is modified by replacing air temperature (a surrogate for the available energy) with a radiation-derived temperature that aims to better represent spatial variations in available energy. Ground cover is also included as an additional insulator of the soil. Furthermore, the modified Berggren Equation, which accounts for soil thermal conductivity and soil moisture, is used to convert the frost index into frost depth. The modified CFGI model (modCFGI) is tested by application at six test sites within SREW.

CHAPTER 2. A RADIATION-DERIVED TEMPERATURE-INDEX SNOW ROUTINE FOR THE GSSHA HYDROLOGIC MODEL

2.1 Introduction

Snow accumulation and ablation are important hydrologic processes in the western United States as well as many other regions of the world. For example, Barros and Lettenmaier (1993) estimated that snowmelt from headwater catchments that compose less than 25% of the total land area provide approximately 70% of the annual runoff in the western United States. Wahl (1992) estimated runoff from snowmelt contributes 50 to 80% of the annual downstream water supply. While the volume of water held within the snowpack is important, the timing of the release of water from the snowpack is also important for flood protection as well as agricultural and municipal water supplies. Furthermore, accurate estimation of the spatial pattern of snowpack is vital to determining the seasonal volume of snow water equivalent (SWE) and the shape, peak, and duration of the basin outflow due to snowmelt (Luce et al., 1998; Pomeroy et al., 2009).

Snow accumulation and melt are both driven by the fundamental laws of conservation of mass and energy. As described in Aguado (1985), the majority of studies indicate that net radiation is the primary source of energy for snowmelt, while turbulent heat transfer is of secondary importance. Spatial variations in net radiation due to cloud cover (Aguado, 1985; Sicart et al., 2006), sun position, topography (Blöschl et al., 1991; Kirnbauer et al., 1994), and vegetation result in heterogeneous snow accumulation and melt patterns throughout a basin. For example, Jost et al. (2007) found that elevation, forest cover, and aspect explain most of the large-scale variability in snowpack within a watershed in the Kootenay Mountains in southeastern British Columbia, Canada. Adequately simulating the accumulation and ablation processes within snow models, including spatial variability (e.g. forested and non-forested), is currently of much interest, as evidenced by the Snow Model Intercomparison Projects (SnowMIP 1 and 2) (Etchevers et al., 2004; Essery et al., 2009).

Water managers, hydrologists, and engineers commonly utilize numerical models to estimate the volume of SWE in headwater areas in order to plan for operations of reservoirs and other water control structures. One such model is the Gridded Surface Subsurface Hydrologic Analysis (GSSHA) model (Downer and Ogden, 2004), which has been widely-used for various military, civilian, and research applications (Downer et al., 2006; Sharif et al., 2010; Wright et al., 2014). GSSHA is a fully-distributed hydrologic model that simulates physically-based equations of mass and energy conservation on a structured grid. For snowpack simulation, the model can utilize either an energy-balance or a temperature-index (TI) method (Follum and Downer, 2013), with the TI model being based upon *SNOW-17* (Anderson, 1973, 2006). Energy-balance approaches can outperform TI models in representing the spatial heterogeneity of the snowpack (Kumar et al., 2013), but suffer from the need for highly-accurate forcing data (Lei et al., 2007) that are not available in most watersheds. Large-scale energy balance models, such as the National Weather Service's Snow Data Assimilation (SNODAS) model (Carroll et al., 2001; Barrett, 2003), simulate snow over the coterminous United States but do so at a 1 km^2 spatial resolution, which is coarser than the resolution used in many distributed hydrologic models. TI models are advantageous when forcing data are limited because they require only precipitation and air temperature data as drivers.
TI snow models have long been used within hydrologic models due to their simplicity of relating air temperature to snowmelt through the use of a melt factor. In these models, air temperature is used as an index (i.e. proxy) to determine the energy exchange across the snow-air interface (Anderson, 2006), where air temperature is typically estimated throughout the basin based on the local topographic elevation and a specified lapse rate. The use of TI models within fully-distributed models has increased due to the availability of air temperature data and gridded elevation data (Daly et al. 2000; Zeinivand and De Smedt, 2009; Jost et al. 2012; Kumar et al. 2013). However, TI approaches typically do not account for the effects of slope, aspect, and vegetation cover, which have been shown to control snowpack and snowmelt

patterns. It has also led to inaccuracies when comparing simulated snowpack to satellite-derived estimates of snow covered area (SCA), which are often the only validation dataset available (Mhawej et al. 2014; Vuyovich and Jacobs, 2011).

More recently, methods have been utilized to better account for topographic and vegetative differences within TI models (Hock (2003) provides a thorough overview). Simple approaches, such as empirically adjusting the temperature based on aspect and the location of forested areas, have had some success (Kang, 2005). Other approaches use a melt factor that varies based on monthly (Cazorzi and Dalla Fontana, 1996; Dunn and Colohan, 1999) or hourly (Hock, 1999) radiation calculations over the discretized area. Shamir and Georgakakos (2006) modified melt factors based on the aspect of each cell in the model domain to simulate a distributed snowpack using a TI model. Another common method (Brubaker et al., 1996; Bookhagen and Burbank, 2010; Kustas et al., 1994; Molotch and Bales, 2006) is to separate the drivers of melt into two terms. The first term estimates the melt due to turbulent heat flux based on the melt factor and air temperature. The second term converts a radiation amount to an amount of melt. In this approach, the melt factor is only used to estimate melt due to turbulent heat flux instead of the total melt. Butcher (2009) incorporated this method into the *SNOW-17* model (producing *SNOW-17 EB*) but found that *SNOW-17* outperformed *SNOW-17 EB* when deployed at the Reynolds Creek Experimental Watershed in Idaho, USA. This result likely occurs because *SNOW-17 EB* requires high-quality spatiotemporal forcing data (e.g., temperature, precipitation, cloud cover, relative humidity, shortwave radiation, longwave radiation), which is an issue shared by full energy-balance snow models (Franz et al., 2008).

The objective of this paper is to better account for spatial heterogeneity of available energy within the GSSHA TI model while preserving the strengths of this approach, particularly its limited data requirements and widely-used mathematical structure. In TI models, air temperature is used as a proxy for the energy available for heating or melting the snowpack. This approach is relatively successful due to the high correlation between air temperature and energy balance components (Ohmura, 2001). In this paper, we propose an alternative proxy temperature that is derived from the radiation balance including simple calculations of the net shortwave radiation (which includes the effects of topography, clouds, vegetation, and albedo) and net longwave radiation (which includes contributions from the air, vegetation, cloud cover, and approximate snow temperature). This radiation-derived temperature index (RTI) approach is explored because radiation is typically the primary driver of snowmelt in many locations, data are available to incorporate spatial variations in the components of the radiation balance (and thus the RTI), and this approach retains the widely-used TI model structure.

2.2 Methodology

2.2.1 Existing GSSHA TI Model

The existing TI model in GSSHA (from now on, referred to as TI) is based on *SNOW-17* (Anderson, 1973, 2006) and was implemented into GSSHA by Follum and Downer (2013). *SNOW-17* is typically operated by the National Weather Service using a time step (dt) of 6 hours but can be used at various time intervals (Anderson, 2006). GSSHA allows for a variable time step for various processes (e.g., flow routing, infiltration, and evaporation), but it uses an hourly time step for snow simulation. In the TI model, precipitation (P) in each cell is considered to fall as snow when $T_a \leq PXTEMP$, where T_a is the air temperature (°C) and $PXTEMP$ is the temperature (°C) at which precipitation is considered snow. An under-catch adjustment factor (SCF) can be used to account for inaccuracies in precipitation data (Anderson, 2006). Each cell of the GSSHA model can have varying values of T_a and P, and therefore each cell can accumulate and melt snow independently from the surrounding cells.

The change in heat deficit (ΔD_t, mm of SWE) within the snowpack due to differences between the temperature of the air and snow surface is accounted for as:

$$\Delta D_t = NMF \cdot (ATI - T_{sur}) \tag{1}$$

where ATI is the antecedent temperature index (°C) (as calculated in Anderson, 2006), T_{sur} is the snow surface temperature (as in Anderson (2006), T_{sur} is assumed to be equal to T_a or 0°C, whichever is less), and NMF is the negative melt factor (mm °C^{-1} dt^{-1}). NMF is calculated as:

$$NMF = NMF_{max} \cdot (dt/6) \cdot \left(M_f / M_{f,max}\right) \tag{2}$$

where NMF_{max} is the maximum negative melt factor (mm °C^{-1} (6 hr)$^{-1}$), M_f is the melt factor (mm °C^{-1} dt^{-1}), and $M_{f,max}$ is the maximum melt factor (mm °C^{-1} (6 hr)$^{-1}$), which is usually calibrated. An additional calibration parameter, $TIPM$, is included in the calculation of ATI and ranges between 0.0 and 1.0 (Anderson, 2006). The change in heat deficit due to snowfall is also accounted for within the TI model using the approach from Anderson (2006).

Melt occurs once the energy input into the snowpack overcomes the heat deficit. When little or no rain occurs (less than 1.5 mm during the previous 6 hours), the amount of melt in a time step is calculated as:

$$M = \left[M_f \cdot (T_a - MBASE) + 0.0125 \cdot P \cdot f_r \cdot T_r\right] \cdot \ dt \tag{3}$$

where M is the melt in mm, P is in mm, $MBASE$ is the temperature above which snow begins to melt (typically set to 0°C), f_r is the fraction of precipitation in the form of rain when T_a>0°C, and T_r is the precipitation temperature in °C (taken as equal to T_a or 0°C, whichever is greater). The melt factor is calculated as:

$$M_f = (dt/6) \cdot \left[S_v \cdot A_v \cdot \left(M_{f,max} - M_{f,min}\right) + M_{f,min}\right] \tag{4}$$

where S_v is a sine curve that accounts for seasonal melt variation, A_v is a seasonal melt variation adjustment (for the Northern Hemisphere, it is set to 1.0 when lower than 54°N latitude, and it varies linearly between 0.0 and 1.0 as a function of time of year when above 54°N latitude), and $M_{f,min}$ is a calibrated minimum melt factor (mm °C^{-1} (6 hr)$^{-1}$). Using S_v and A_v, the model varies M_f seasonally between $M_{f,min}$ and $M_{f,max}$, which empirically accounts for the seasonal variations in solar radiation and snow albedo.

When at least 1.5 mm of rainfall occurs during the previous 6 hours an energy balance is used to calculate the amount of snowmelt with the assumption that snow surface temperature is 0°C, incoming solar radiation is negligible, and incoming longwave radiation is equal to black body radiation (Anderson 2006):

$$M = \sigma \cdot dt \cdot \ [(T_a + 273)^4 - 273^4] + 0.0125 \cdot P \cdot f_r \cdot T_r + 8.5 \cdot f_u \cdot (dt/6) \cdot [(rh \cdot e_{sat} - 6.11) + 0.00057 \cdot P_a \cdot T_a] \tag{5}$$

where σ is the Stefan-Boltzmann Constant ($6.12 \cdot 10^{-10}$ mm K^{-1} hr^{-1}), f_u is the average wind function (mm mb^{-1} $(6\ hr)^{-1}$), rh is the relative humidity (assumed to be 0.9 during rain-on-snow events) (Anderson, 1973, 2006), P_a is atmospheric pressure (mb, calculated based on elevation) (Anderson, 2006), and e_{sat} is the saturated vapor pressure (mb, calculated based on Smith, 1993). Water leaves the snowpack when the liquid water content exceeds the liquid holding capacity, which is calculated as a calibrated percentage ($PLWHC$) of the ice portion of the snow cover (Anderson, 2006).

2.2.2 New GSSHA RTI Model

In the RTI model, a radiation-derived temperature (T_{rad}, °C) replaces T_a in the equations that are used to calculate snowmelt (Eq. (3) and (5)), while rainfall and snowfall continue to be distinguished using T_a. T_{rad} is calculated based on a radiation balance at the surface of the snowpack. If one neglects all terms in the snow surface energy balance aside from radiation, one can write:

$$LW_{\uparrow} = SW_{\downarrow,net} + LW_{\downarrow} \tag{6}$$

where $LW_{\uparrow}$ is outgoing longwave radiation, $SW_{\downarrow,net}$ is the net shortwave radiation, and $LW_{\downarrow}$ is the downwelling longwave radiation. Equation 6 neglects any advected heat from precipitation, ground heat flux, sensible heat flux, latent heat flux, heat lost from melt water leaving the snowpack, or changes in the thermal energy of the snowpack (i.e. heat deficit). Using the Stefan-Boltzmann Law to relate the radiated energy to temperature, one can calculate an estimate of the snow surface temperature, which is T_{rad} (°C), as:

$$T_{rad} = \left[\frac{LW_{\downarrow} + SW_{\downarrow,net}}{\varepsilon_{snow}\,\sigma}\right]^{1/4} - 273.15 \tag{7}$$

where all radiation terms are in units of W m^{-2}, ε_{snow} is the emissivity of snow (assumed to be 1.0), and σ is the Stefan-Boltzmann constant (approximated as $5.6704 \cdot 10^{-8}$ W m^{-2} K^{-4}). T_{rad} is not expected to represent the actual temperature of the snow surface because of the assumptions described earlier. In addition, the calculation of T_{rad} does not consider the ice/water phase transition, so T_{rad} can exceed 0°C. Instead, T_{rad} is interpreted as an index of energy that is available to heat or melt the snowpack. Although it is simplistic, this approach considers more elements of the energy balance than the TI model. T_a in the TI model is only directly associated with the downwelling longwave radiation from the air ($LW_{\downarrow,air}$), which is a component of $LW_{\downarrow}$ ($LW_{\downarrow}$ includes longwave contributions from the air, canopy, and cloud cover). T_{rad} in the RTI model considers both $SW_{\downarrow,net}$ and $LW_{\downarrow}$ (Figure 2)

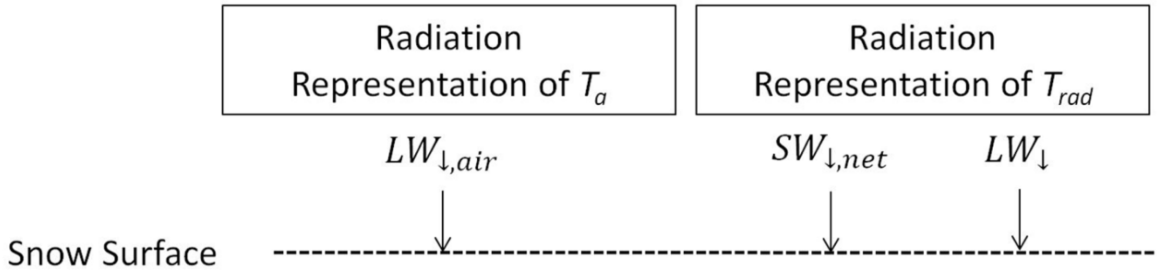

Figure 2. Radiation components included in the proxy temperatures T_a and T_{rad}.

Methods were selected to calculate $SW_{\downarrow,net}$ and $LW_{\downarrow}$ that introduce as few parameters and data requirements as possible. $LW_{\downarrow}$ is determined by first calculating the downwelling longwave radiation at the top of canopy ($LW_{\downarrow,toc}$), which includes longwave radiation from the air and clouds. Neglecting the impact of the surrounding terrain on $LW_{\downarrow}$, GSSHA (Downer and Ogden, 2006) uses methods developed and tested by TVA (1972) to estimate $LW_{\downarrow,toc}$ as:

$$LW_{\downarrow,toc} = \sigma\varepsilon_a(T_a + 273.15)^4 \cdot (1.0 + 0.17\,N^2) \tag{8}$$

where ε_a is the air emissivity, and N is the fractional cloud cover. Various methods are available for calculating ε_a (TVA, 1972; Idso, 1981; Prata, 1996), but they often require additional data such as relative humidity. To keep the forcing data requirements low, ε_a is estimated as 0.757 when snow is present (Bras, 1990). T_a is linearly adjusted for local variation in elevation based on Bras (1990):

$$T_a = T_g + \theta\left(Elev_g - Elev_c\right) \quad (9)$$

where T_g is the measured air temperature at a gage (°C), θ is a positive lapse rate (°C m^{-1}), and $Elev_g$ and $Elev_c$ are the elevations of the temperature gage and the cell of interest (m), respectively. Following the parsimonious approach of Liston and Elder (2006), the incident longwave radiation at the snow surface ($LW_{\downarrow}$) can then be estimated as:

$$LW_{\downarrow} = LW_{\downarrow,toc}(1 - F_c) + F_c \varepsilon_c \sigma\left(T_{canopy} + 273.15\right)^4 \quad (10)$$

where T_{canopy} is the canopy temperature (°C) (assumed equal to the air temperature following DeWalle and Rango, 2008), ε_c is the canopy emissivity (assumed equal to 1 following Sicart et al., 2004), and F_c is the fractional canopy cover, which is 0 if no forest is present. Otherwise, F_c is estimated as (Liston and Elder, 2006):

$$F_c = f_a + f_b\, ln(LAI) \quad (11)$$

where f_a and f_b are set to 0.55 and 0.29, respectively (Pomeroy et al., 2002), and LAI is the leaf area index within the cell. LAI data are required for the RTI model but not the TI model. However, LAI is already used to estimate the canopy resistance for evapotranspiration calculations in GSSHA, so it is not a new data requirement for the model as a whole. Liston and Elder (2006) also provides a table of LAI values for tree types that are common in cold climates.

The amount of downwelling shortwave radiation that is absorbed by the snow surface is:

$$SW_{\downarrow,net} = (1 - \alpha)SW_{\downarrow} \quad (12)$$

where $SW_{\downarrow}$ is the incident shortwave radiation and α is the albedo of the snowpack. Measurements of $SW_{\downarrow}$ are rarely available, and if available, they are typically from a single location. Therefore, $SW_{\downarrow}$ for each grid cell is estimated:

$$SW_{\downarrow} = S_0\,K_r\,K_{atm}\,K_c\,K_v\,K_s\,K_t \tag{13}$$

where S_0 is the solar constant (1366 W m^{-2} from Liou, 2002) and the K factors are the reductions in the shortwave radiation due to distance from the earth to the sun (K_r), atmospheric scattering (K_{atm}), absorption by clouds (K_c), vegetation (K_v), slope/aspect of terrain (K_s), and topographic shading (K_t). The adjustment K_r accounts for the effects of the distance from the sun based on the Julian day (JD) (TVA, 1972):

$$K_r = \left[1.0 + 0.017\,\cos\left(\frac{2\pi}{365}(186 - JD)\right)\right]^{-2} \tag{14}$$

The reduction in shortwave radiation due to atmospheric thickness as well as aerosols and moisture (K_{atm}) is estimated for each cell based on its elevation (Allen et al., 2005):

$$K_{atm} = 0.75 + \left(2 \cdot 10^{-5}\right) \cdot Elev_c \tag{15}$$

Other methods of calculating K_{atm} are available (e.g., Eagleson, 1970; Bras, 1990; Shuttleworth, 1993), but they require additional parameters or data. The reduction in shortwave radiation (K_c) due to absorption and reflection by clouds is determined as (TVA, 1972):

$$K_c = 1.0 - 0.65\,N^2 \tag{16}$$

where N is the fractional cloud cover. Other methods have been suggested for estimating the effects of clouds on $SW_{\downarrow}$ (see DeWalle and Rango, 2008), but the TVA (1972) method was selected to be consistent with the source used for calculation of $LW_{\downarrow}$.

The reduction in shortwave radiation reaching the ground surface due to vegetation (K_v) is set equal to the vegetation transmission coefficient, a parameter that is vegetation-type specific and represents a fraction of the shortwave radiation that is not intercepted by the vegetation canopy (see Bras, 1990). The vegetation transmission coefficient is a standard input for evaporation calculations within GSSHA, and has values ranging between 0 for complete canopy coverage and 1 for no canopy coverage.

The solar radiation emitted from the sun rarely strikes the land surface at a perpendicular angle, which results in a reduction (K_s) in the incident shortwave radiation per unit area. K_s can be calculated based on the angle of incidence (φ), which is the angle between the solar beam on the surface and a vector that is normal to that surface (Figure 3). Duffie and Beckman (1980) calculate φ using the latitude, slope, and azimuth angle of the grid cell, and the solar declination (Shuttleworth, 1993) and hour (Duffie and Beckman, 1980) angles. K_s is then calculated as

$$K_s = \cos(\varphi) \tag{17}$$

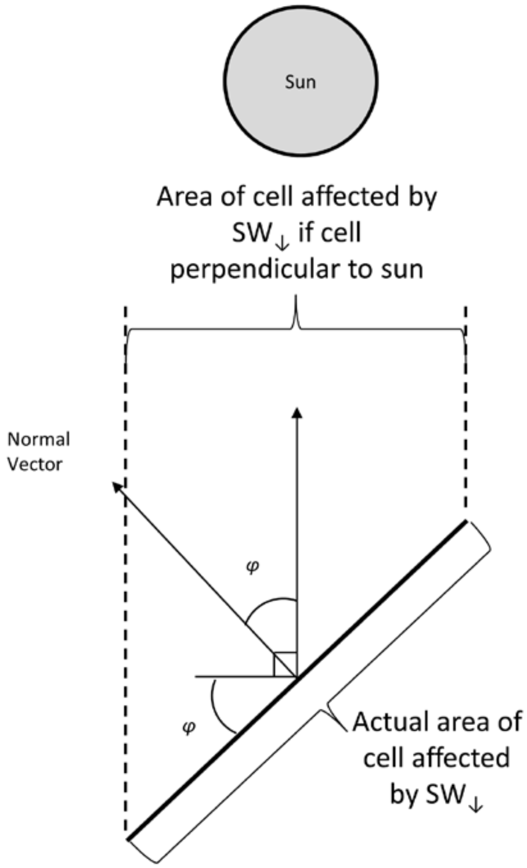

Figure 3. Two-dimensional representation of the reduction in $SW_{\downarrow}$ due to the angle of incidence (φ) between the sun and the normal vector of the terrain. The TI model does not account for this reduction in $SW_{\downarrow}$. The RTI model calculates the reduction in three-dimensional space.

Direct solar radiation can also be blocked by nearby topography, such as when mountains shade valleys. This effect is represented by K_t. Hourly values of solar azimuth (Duffie and Beckman, 1980) and solar elevation angles (Eagleson, 1970) are calculated and used in combination with geometry of the topography to determine if any cell within the simulation domain blocks the direct line between the solar location and the cell surface. If the sun is blocked during an hour, then K_t is set to 0.0 for that hour (indicating complete shading). Otherwise, K_t is set to 1.0 (indicating no shading). This approach is similar to that of the *GEOTOP* model (Zanotti et al., 2004).

Most equations used to calculate snow albedo (α) assume that α gradually declines over time and then suddenly increases when fresh snow falls on the snowpack. A summary of different methods used to calculate α can be found in DeWalle and Rango (2008). Here, daily values of snow albedo (α) are computed based on the number of days since the last snowfall (d) following Henneman and Stefan (1999). For periods when no melt is occurring, α for the current day (t) is:

$$\alpha_t = 0.83 - 0.011 \cdot d \tag{18}$$

When melt is occurring:

$$\alpha_t = \alpha_{t-1} - w \tag{19}$$

where w is 0.17 if the average daily temperature is above 0°C, and 0.013 when it is not. The minimum allowed value for α is 0.38. This albedo model does not account for dust or other particulates, which can have important effects on snow ablation (Painter et al., 2007; Skiles et al., 2012; Skiles et al., 2015). However, the RTI model can potentially include dust impacts in the future by adjusting α, whereas the TI model does not directly consider the albedo.

2.3 Model Application

2.3.1 Study Area

The TI and RTI snow models in GSSHA are tested at the 2.9 km^2 Senator Beck Basin (SBB) in southwestern Colorado. The study period is 1 July 2006 through 30 Sept 2012, which is approximately water year (WY) 2007 through WY 2012. The SBB is in the Ouray Ranger District of the Uncompahgre National Forest in the western San Juan Mountains (Figure 4). It is located at 37° 54' 24.8" N x 107° 43' 34.6" W and has an elevation range from 3362 m to 4118 m. The basin is primarily alpine terrain with bare rock and tundra as well as some forested areas below 3600 m. It is extensively gaged for both hydrometeorology and hydrology by the Center for Snow and Avalanche Studies. Additional basin information and data are provided by Landry et al. (2014).

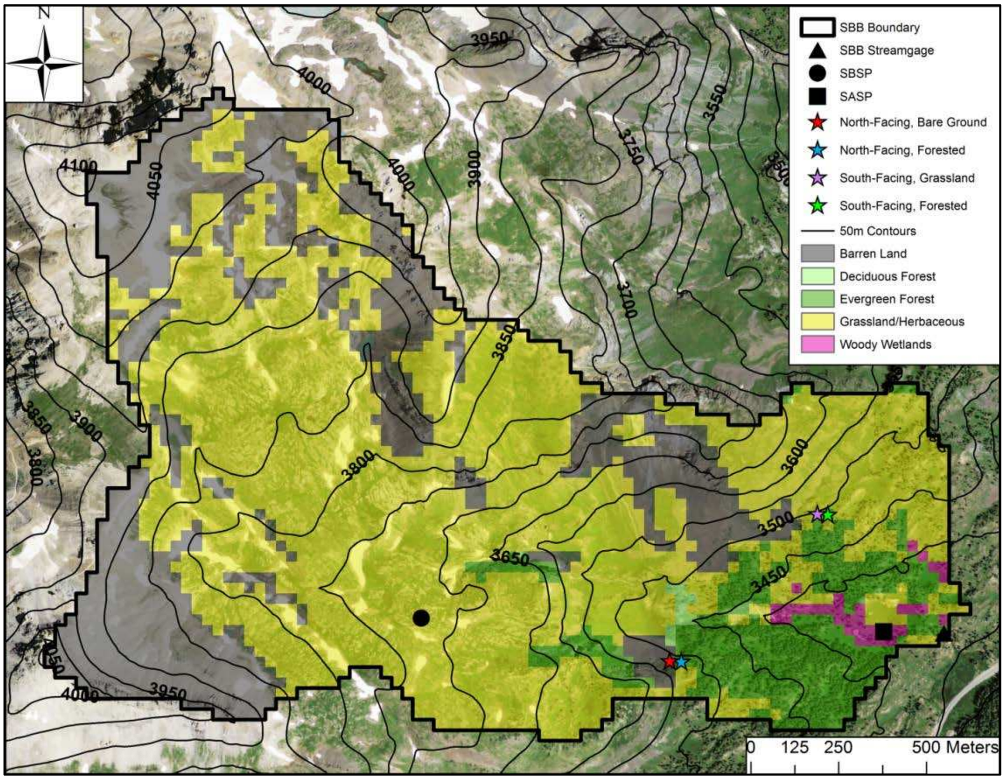

Figure 4. SBB, Colorado, USA. Land cover classifications are from the 2006 National Land Cover Database and are overlain on United States Geological Survey 1-m orthoimagery data. Elevation contours (50 m) are from the 1/3-arc-second National Elevation Dataset. Sites considered in this study are shown by black symbols and colored stars.

The Swamp Angel Study Plot (SASP) and Senator Beck Study Plot (SBSP) are monitored within the basin. SASP has a lower elevation (3371 m) and is located in a large forest clearing with surrounding terrain that provides shelter from wind effects on precipitation and snowpack measurements. SBSP is a more-exposed and higher-elevation site (3714 m) that is located in alpine tundra where the effects of wind are more prevalent. Temperature, shortwave radiation, longwave radiation, and snow depth data are available for SASP and SBSP (Figure 4), but precipitation data are only available for SASP.

The Center for Snow and Avalanche Studies uses formal snow cover profiles adjacent to the SASP and SBSP sites to measure SWE, snow depth, and snow density. Measurements are taken monthly in the early winter and weekly during the late winter and spring at SASP, and they are taken as feasible at SBSP. As discussed in Skiles et al. (2012), measurements of SWE are taken several meters away from the SBSP weather station and may not reflect the SWE exactly at the weather station site. Therefore, rather than using the SWE measurements from the snow cover profiles, the densities from the snow cover profiles are used with automated depth measurements at the SBSP weather station to determine more accurate SWE estimates at the SBSP weather station site itself (Skiles et al., 2012). For consistency, the same approach is used at SASP, but the differences are smaller at this site. These SWE estimates will be used throughout this study.

2.3.2 Additional Comparative Snow Data

The SNow THERmal Model (SNTHERM; Jordan, 1991) was previously used to model the SWE at SASP and SBSP (Landry et al., 2014). Thus, the TI and RTI results can be compared to a multilayer energy-balance snow model, which is based on the mass and energy balance model by Anderson (1976). It should be noted, however, that the SNTHERM parameters were not calibrated but set to published values in those simulations.

To supplement the data from the SBSP and SASP sites, LandSat 5 imagery was used to derive snow covered area (SCA) maps of the basin. LandSat 5 includes six spectral bands (blue, green, red, near-infrared, and two shortwave infrared) at a 30 m resolution, which create unique spectral signatures that can be used in the mapping of snow cover within a basin (Dozier and Marks, 1987). The Iterative Self-Organizing Data Analysis Techniques (ISODATA) (Ball and Hall, 1965; Tou and Gonzalez, 1974) within the ERDAS (1999) software was used to group pixels with similar spectral signatures into thematic classes, which were then assigned a designation as snow, no-snow, or snow fringe based on the ISODATA thematic classes and visual interpretation of the classes compared to orthoimagery. Snow fringe was defined as the transition between the snow/no-snow classes and likely represents partial snow coverage within the pixel. In total, 32 LandSat images are available for the study period, but most images were collected when the snow cover was either absent or nearly complete, which greatly reduces their value for testing the models. Thus, only 12 images were used in the study, all of which indicate between 25% and 75% coverage of snow within the basin.

2.3.3 Model Forcing Data

The Watershed Modeling System (Aquaveo, 2013) was used to develop a 30-m structured grid for GSSHA. This resolution was judged to adequately capture the spatial heterogeneity of the basin while remaining computationally efficient. The basin was delineated using the 1/3-arc-second (~9 m) National Elevation Dataset (Gesch et al., 2002), and elevation data were then mapped onto the structured grid of the basin, which contains 3207 grid cells.

Land cover classifications were derived from the 2006 National Land Cover Database (Fry et al., 2011). Approximately 62.1% of the basin is classified as grass/herb, 27.2% as barren land, 9.4% as evergreen forest, 0.3% as deciduous forest, and 1.1% as wooded wetlands (Figure 4). Comparisons between the land cover map and United States Geological Survey 1-m orthoimagery data (from 28 May 2014) show that the wooded wetlands are actually grass/herb and were therefore reclassified.

The precipitation data from SASP are assumed to apply to the entire SBB. Although the basin is relatively small, the topographic relief likely produces uncaptured variations in precipitation. The temperature data from SASP and SBSP were used to calculate hourly values of lapse rate, which was restricted to the range from 0.0 to 0.00981 °C m^{-1} to avoid occasional anomalous temperature patterns. Once the lapse rate was determined, the temperature for each grid cell was calculated relative to SBSP using Eq. (9). Cold air drainage from higher elevations into the sheltered terrain pocket at SASP does occur, which sometimes causes colder overnight low temperatures at SASP than SBSP (Landry et al., 2014). This negative lapse rate is assumed to be local to the SASP terrain pocket and not representative of the temperature profile throughout the majority of the basin and therefore neglected in the model. Satellite-derived and locally observed cloud cover data are available from the National Centers for Environmental Information (NCEI, https://www.ncdc.noaa.gov/). Observed cloud cover measurements, which vary in temporal resolution, are often taken at airports as part of the local climatological data archived at the NCEI. These surface aviation cloud cover data are available throughout the day and night from the Telluride Regional Airport (TEX), which is approximately 16 km to the northwest of SBB. This dataset consists of five classifications of cloud cover. Each classification is associated with a range of eighths (or oktas) of the sky that are covered by clouds (e.g., the scattered clouds classification ranges from 3 to 4 oktas). Based on the range of each classification, we determined cloud cover percentages as follows: clear (CLR) – 0%, few clouds (FEW) – 12.5%, scattered clouds (SCT) – 43.75%, broken sky (BKN) – 75%, and overcast (OVC) – 100%. When multiple classifications were recorded for the same time period, the average of the associated percentages was used. The cloud cover was measured at irregular time intervals, but was interpolated to produce hourly data for this project. Cloud cover data are not available from 08 Apr 2009 through 11 Nov 2009, which provides an opportunity to investigate the importance of this data (recall that the TI model does not require cloud cover data, while the RTI model does). For this period, the cloud cover values were determined by randomly sampling the observations from the same day and hour during the other years in the dataset. This approach aims to capture realistic variations in cloud cover, but it is not expected to reproduce the actual cloud cover in 2009. The effects of this approach will be examined later.

2.3.4 Parameter Estimation and Calibration

The Model-Independent Parameter Estimation and Uncertainly Analysis (PEST) method (Doherty et al., 1994) was used to calibrate the parameters within the TI and RTI models. PEST is a nonlinear parameter estimator that calibrates numerous parameters simultaneously to produce the best fit between observed and simulated results. In this study, the TI and RTI models were calibrated to reproduce SCA, which characterizes the extent of snowpack across the watershed (not the SWE observations, which are available only at a few points). In particular, the error between the model and the observations is calculated:

$$Error = \frac{A_{over} + A_{under}}{A_{obs}} \tag{20}$$

where A_{over} is area where the model predicts snow cover but no snow is observed, A_{under} is the area where the model predicts no snow cover but snow is observed, and A_{obs} is the total observed SCA. An error value of 0 indicates perfect fit between simulated and observed SCA. In this comparison, cells that are classified as snow-fringe from the LandSat analysis are considered snow. The six LandSat SCA estimates from the first three water years (1 July 2006 through 30 Sept 2009) were used as the calibration period, and the remaining six SCA estimates from the last three water years were used as the validation period.

The allowable range, starting value, calibrated value, and sensitivity ranking of each parameter for the TI and RTI models are shown in Table 1. Precipitation and temperature data are expected to be accurate at SBB, therefore the *SCF* and *MBASE* parameters were assigned to their default values of 1.0 and 0°C, respectively, and not calibrated. *PXTEMP* was also set to 0°C. The lower limit of the calibration limit was set to 0.001 for all other parameters, with the starting value being approximately the average of the allowable range. The upper limit of the allowable range for $TIPM$ was set based on physical ranges from Anderson (2006), while the upper limit for $PLWHC$ was set to 0.1 based on typical values found in the field (Singh et al., 1997; Gerdel, 1954). The upper limits for $M_{f,min}$ and $M_{f,max}$ were set to double their approximate values within the conterminous United States from Anderson (2006). The physical range of K_v is between 0.0 and 1.0, but only K_v values for deciduous trees ($K_{v,deciduous}$) and evergreen trees ($K_{v,evergreen}$) are used as calibration parameters. The starting value for both $K_{v,deciduous}$ and $K_{v,evergreen}$ was set to 0.4 based on USACE (1956) and an estimated 25% fractional vegetation cover in the forested areas of SBB. Due to the sparse and patchy vegetation in other land cover classifications as well as the tendency of snow to cover all vegetation except for trees in SBB, K_v for all other classifications was set to 1.0.

Recall that the original TI model partially accounted for seasonal changes to α and $SW_{\downarrow}$ by empirically varying M_f with time. Because both α and $SW_{\downarrow}$ are now incorporated into the RTI model and vary seasonally, M_f is assumed to remain constant in the RTI model. The original TI model uses the ratio of M_f to $M_{f,max}$ to indirectly account for seasonal changes in the calculation of ΔD_t (Eq. (1) and (2)). Because M_f is constant in the RTI model, the RTI model instead accounts for seasonal changes in ΔD_t by replacing the previous ratio with the ratio of $SW_{\downarrow,\text{day,noon}}$ to $SW_{\downarrow,\text{year,noon}}$, where $SW_{\downarrow,\text{day,noon}}$ is the shortwave radiation at noon on a flat surface for the day of interest and $SW_{\downarrow,\text{year,noon}}$ is the maximum shortwave radiation at noon on a flat surface over the entire year. Calculation of $SW_{\downarrow,\text{day,noon}}$ and $SW_{\downarrow,\text{year,noon}}$ only requires S_0, K_s, K_r, and K_{atm}, which are already used by the RTI model. Using common values of 1.2 for $M_{f,max}$ and 0.4 for $M_{f,min}$ (Anderson, 2006), the ratios $M_f/M_{f,max}$ and $SW_{\downarrow,\text{day noon}}/SW_{\downarrow,\text{year noon}}$ are compared in Figure 5 for SBB during the year 2008. Although not exact, the ratio of $SW_{\downarrow,\text{day noon}}/SW_{\downarrow,\text{year noon}}$ resembles the ratio of $M_f/M_{f,max}$, indicating that seasonal changes are still included in the calculation of ΔD_t within the RTI model. These modifications in the RTI model replace the need to calibrate both $M_{f,min}$ and $M_{f,max}$ with only M_f.

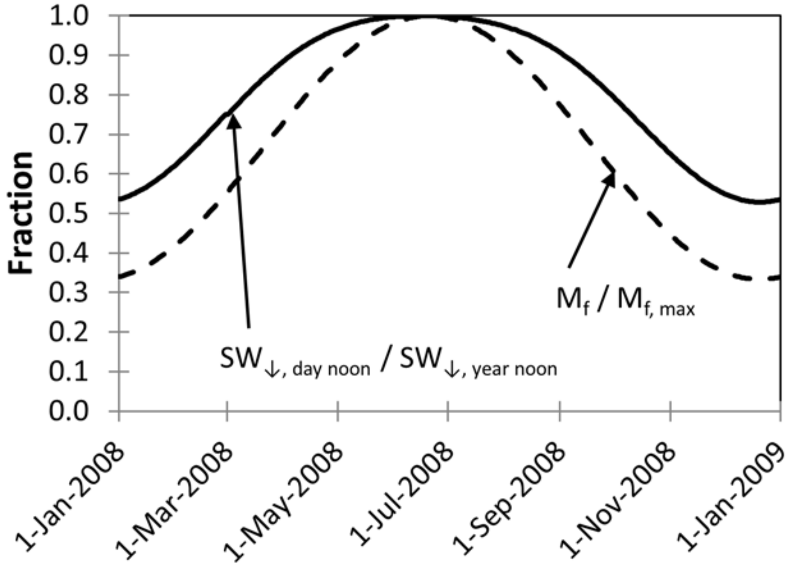

Figure 5. Ratio of M_f to $M_{f,max}$ (used in TI model) compared to the ratio of $SW_{\downarrow,day\ noon}$ to $SW_{\downarrow,year\ noon}$ (used in RTI model). These ratios are used in their respective models to account for seasonal changes in the calculation of ΔD_t.

PEST indicates that the parameters related to melt factors are the most sensitive in both the TI ($M_{f,min}$ and $M_{f,max}$ parameters) and RTI (M_f parameter) simulations (Table 1) $K_{v,evergreen}$ in the RTI model calibrates to 1.000, essentially nullifying any reduction in shortwave radiation due to canopy cover from evergreen trees. The model is insensitive to $K_{v,deciduous}$ likely due to the relatively small area (0.3% of basin) that is classified as deciduous forest, and $K_{v,deciduous}$ calibrates to a value of 0.400 (the starting value).

Table 1. Allowable range, starting value, and calibrated values for the TI and RTI model parameters using PEST. Dashes indicate parameters that are not required in the associated model. The sensitivity ranking for each parameter is shown in parentheses.

Parameter	Units	Allowable Range	Starting Value	TI	RTI
$M_{f,\ max}$	mm °C^{-1} (6 hr)$^{-1}$	0.001-2.400	1.200	1.103 (1st)	--
$M_{f,\ min}$	mm °C^{-1} (6 hr)$^{-1}$	0.001-0.800	0.400	0.800 (2nd)	--
M_f	mm °C^{-1} (6 hr)$^{-1}$	0.001-2.400	0.800	--	0.469 (1st)
NMF_{max}	mm °C^{-1} (6 hr)$^{-1}$	0.001-2.400	1.200	1.794 (5th)	2.215 (3rd)
f_u	mm mb^{-1} (6 hr)$^{-1}$	0.001-1.000	0.500	0.500 (6th)	0.500 (5th)
TIPM	fraction	0.001-1.000	0.500	1.000 (3rd)	0.100 (2nd)
PLWHC	fraction	0.001-0.100	0.050	0.033 (4th)	0.050 (5th)
$K_{v,\ deciduous}$	fraction	0.001-1.000	0.400	--	0.400 (5th)
$K_{v,\ evergreen}$	fraction	0.001-1.000	0.400	--	1.000 (4th)

2.4 Results and Discussion

The results of the TI and RTI models were analyzed in three ways: (1) comparison to observations at SASP and SBSP, (2) comparison of SWE at four selected locations with similar elevations but differences in aspect and vegetation cover, and (3) comparison of SCA and SWE patterns over the entire basin.

2.4.1 SASP and SBSP

One way to partially test the RTI model is to compare its estimates of $SW_{\downarrow}$ and $LW_{\downarrow}$ to the observations at the SASP and SBSP sites. When calculating $SW_{\downarrow}$ at these sites, K_v was set to 1.0, which indicates no vegetation shading. K_s was calculated under the assumption that the pyranometers are level. No parameters were calibrated in the calculation of $SW_{\downarrow}$ or $LW_{\downarrow}$ at these sites, so the calibration and validation periods can be considered together. All comparisons of $SW_{\downarrow}$ and $LW_{\downarrow}$ are made using hourly observation and simulation data.

Figure 6 shows the simulated and observed $SW_\downarrow$ and $LW_\downarrow$ over a representative 7-day span in April 2011. The timing of the rise and fall of $SW_\downarrow$ over the day is mostly well captured for the days in this period. However, on cloud-free days (2nd and 3rd days), the model underestimates $SW_\downarrow$ by approximately 10%. On the other days when clouds are present, the model both underestimates and overestimates $SW_\downarrow$. The observed $LW_\downarrow$ values change little in comparison with $SW_\downarrow$, but higher values correspond to periods with clouds. The model tends to overestimate $LW_\downarrow$ during cloud-free days and underestimate when clouds are present.

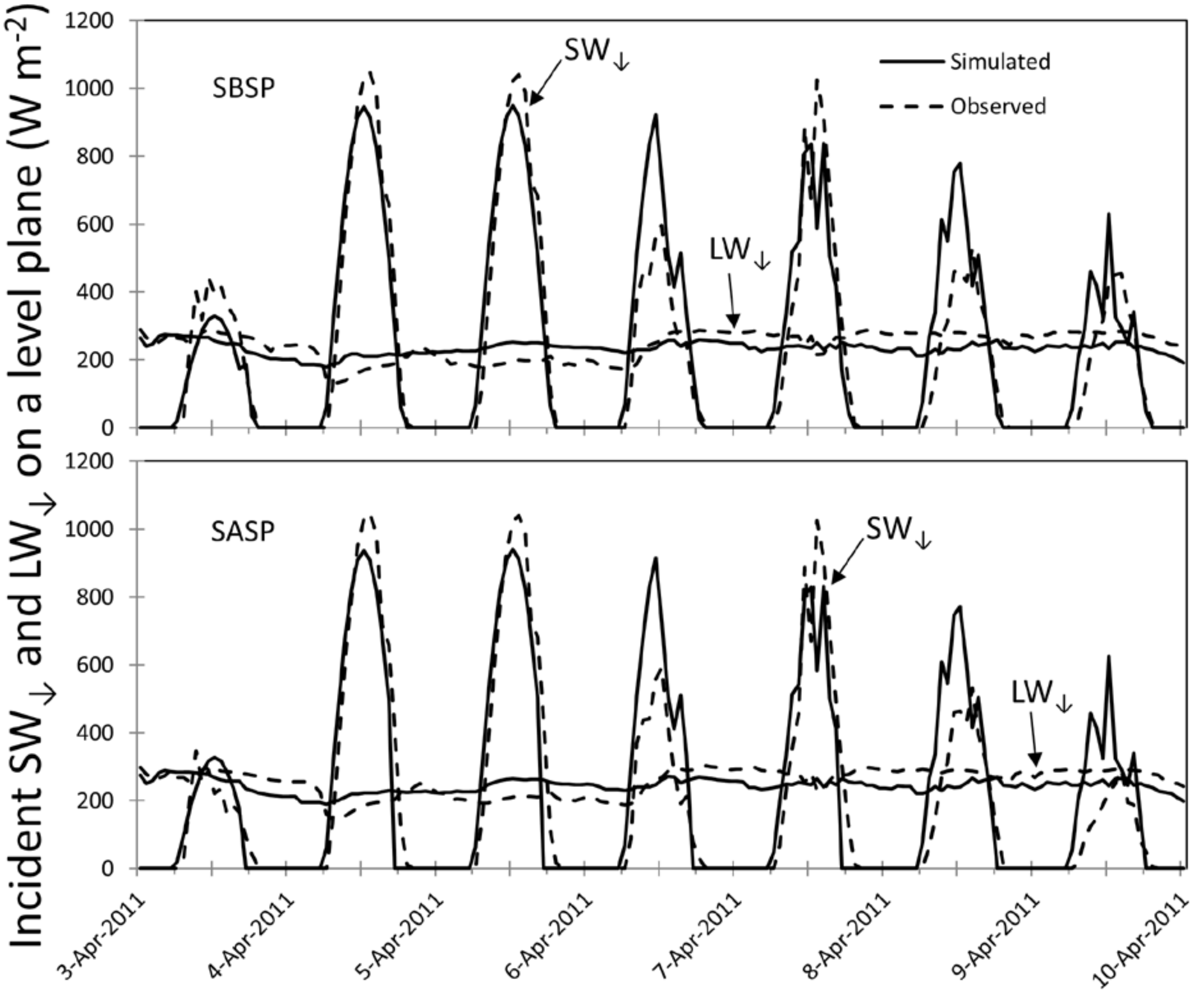

Figure 6. Comparison of observed (dashed) and RTI simulated (solid) $SW_\downarrow$ and $LW_\downarrow$ at SBSP (top) and SASP (bottom) over a typical 7 day period in April 2011.

Considering $SW_{\downarrow}$ for the entire simulation, the Nash-Sutcliffe Efficiency (Nash and Sutcliffe, 1970) is 0.80 for both SASP and SBSP, which suggests that the errors in the $SW_{\downarrow}$ estimates are rather small relative to the variability of the observed $SW_{\downarrow}$ values. These high efficiency values likely occur because the model continues to estimate the timing of the rise and fall in $SW_{\downarrow}$ quite well in each day. The root mean squared error (RMSE) is 133 W m^{-2} for SASP and 129 W m^{-2} for SBSP. At SASP, the RMSE is approximately 64% of the average observed $SW_{\downarrow}$ and 10% of the peak observed $SW_{\downarrow}$. At SBSP, the RMSE is approximately 61% of the average observed $SW_{\downarrow}$ and 10% of the peak observed $SW_{\downarrow}$. The RTI model tends to overestimate values of $SW_{\downarrow}$ at both test plots with a mean bias error (MBE) of 12.4 W m^{-2} and 14.8 W m^{-2} at SASP and SBSP, respectively. These results imply that one or more of the reduction factors in Eq. (13) are set too high (thus increasing $SW_{\downarrow}$). Among the reduction factors, K_{atm} is the most likely to be inaccurate because it was originally developed for agricultural purposes. A method described in Bras (1990) was also tested in which K_{atm} can be calculated based on a turbidity factor of the air and the solar elevation angle. This method produced similar accuracy but tended to underestimate $SW_{\downarrow}$ at both locations.

Comparisons between simulated and observed $LW_{\downarrow}$ are only made when snow is present. RMSE at SASP is 40.8 W m^{-2} (20% of the average observed $LW_{\downarrow}$) and 47.9 W m^{-2} at SBSP (22% of the average). MBE is 12.4 W m^{-2} at SASP and 21.2 W m^{-2} at SBSP, which are both approximately 10% of the average $LW_{\downarrow}$ at the respective gage. Cloud cover increases the simulated $LW_{\downarrow}$ up to 17% (Eq. (8)) with an average increase of 11%. Sicart et al. (2006) found in the Wolf Creek Research Basin in Canada that an increase of up to 50% in $LW_{\downarrow}$ could be attributed to clouds. However, those large increases were rare and average increases in $LW_{\downarrow}$ due to clouds was close to 16%, slightly higher than the 11% average increase found in this study. These results indicate that the approximate increase in $LW_{\downarrow}$ due to clouds may be accounted for in the TVA (1972) method, but the peak increases in $LW_{\downarrow}$ due to clouds may be absent and warrants further investigation. Bohn et al. (2013) indicated that other methods might estimate $LW_{\downarrow}$ better than the

TVA (1972) method. Thus, a more complicated method by Crawford and Duchon (1999) was tested. The Crawford and Duchon (1999) method determines a cloud fraction term by calculating the ratio of measured solar irradiance to the clear-sky irradiance. In the absence of such data, Bohn et al. (2013) used the ratio of calculated solar irradiance to the clear-sky irradiance, which is the same as K_c as defined earlier. Using the cloud fraction term, $LW_{\downarrow}$ was then calculated based on T_a and ε_a. When this method is implemented, the results at both SASP and SBSP have an increase in MBE of approximately 2.5 W m^{-2} and a decrease in RMSE of approximately 0.3 W m^{-2} when compared to the TVA (1972) method.

Figure 7 shows the SWE values from the TI and RTI models at SBSP and SASP, and it compares them to the SWE observations and simulated values from the SNTHERM model, which were produced by Landry et al. (2014). Neither the TI or RTI models were calibrated to these SWE observations (they were calibrated to SCA), and the SNTHERM parameters were set to values commonly found in literature (Landry et al., 2014). At SBSP, the TI and RTI results tend to be similar to the SNTHERM results. However, at SASP, both models are more accurate than SNTHERM. At SBSP, RTI slightly outperforms TI (i.e. its RMSE and MBE are the same or closer to zero, (Table 2) during both the calibration and validation periods. At SASP, the TI model has smaller RMSE values while the RTI model has smaller (magnitude) MBE values during the calibration and validation periods.

In general, the TI and RTI results track closely together at both locations. The TI model tends to slightly underestimate the SWE at SASP (negative MBE values in Table 2 and overestimate the SWE at SBSP (positive MBE values in Table 2, while the RTI model tends to overestimate the SWE at both SASP and SBSP (positive overall MBE values in Table 2). Wind scour is estimated to reduce the maximum SWE by up to 40% at SBSP (Landry et al., 2014). Because the models do not represent this process, it might explain why they tend to overestimate SWE at SBSP. The SASP site is more sheltered, and the modeled results are closer to the observed SWE.

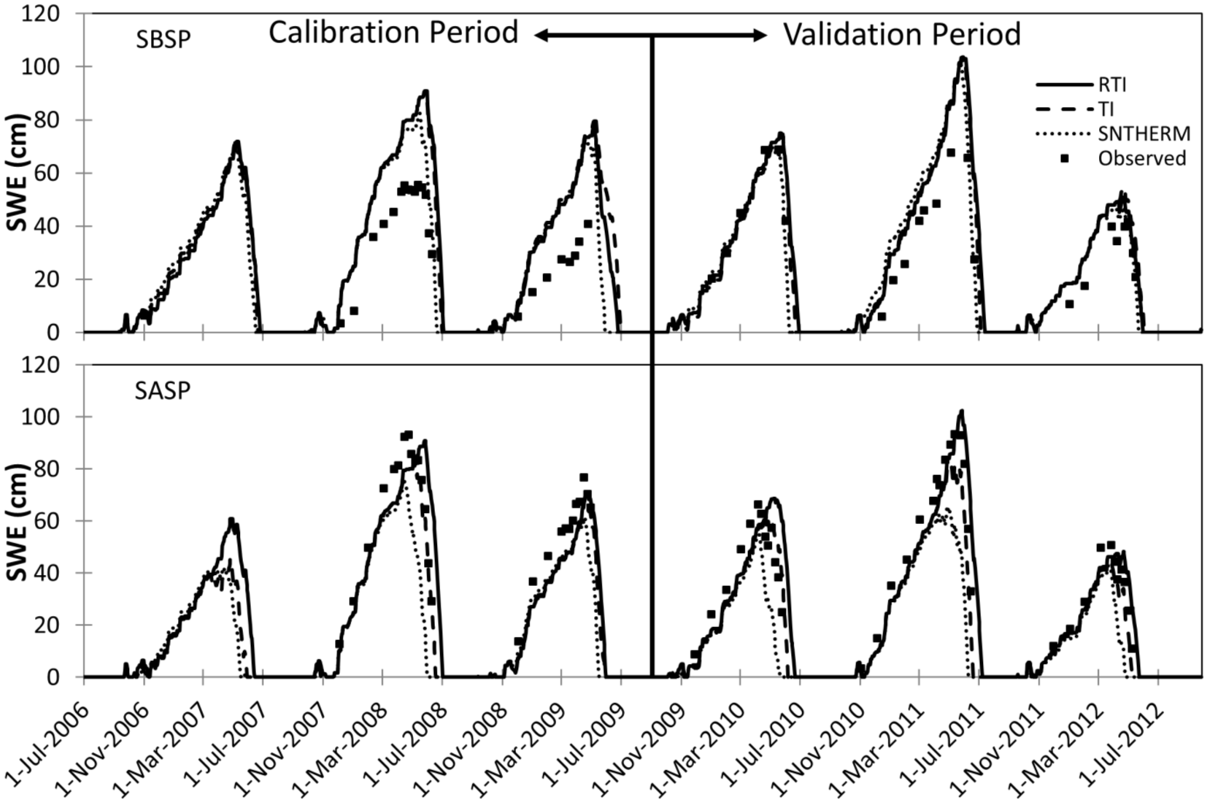

Figure 7. TI and RTI simulated SWE at SBSP (top) and SASP (bottom) compared to observation data and published SNTHERM simulation results (Landry et al., 2014).

Table 2. Statistics for TI and RTI SWE values at SASP and SBSP during the calibration period (1 July 2006 – 30 Sept 2009), validation period (1 Oct 2009 – 30 Sept 2012), and overall (1 July 2006 – 30 Sept 2012). Values closer to zero indicate better fit.

	Calibration		Validation		Overall	
	RMSE (cm)	MBE (cm)	RMSE (cm)	MBE (cm)	RMSE (cm)	MBE (cm)
TI SBSP	26.6	24.0	14.0	10.5	21.1	17.4
RTI SBSP	26.6	23.8	13.7	10.0	21.1	17.0
TI SASP	8.8	-7.7	9.4	-5.7	9.1	-6.5
RTI SASP	14.5	-2.4	13.0	3.1	13.6	0.9

The importance of cloud cover in the RTI model was evaluated by comparing the behavior of the TI and RTI models for the periods with and without cloud cover data. For the five water years with cloud cover data, the peak SWE for the RTI model is on average 17.8% higher at SASP and 1.8% lower at SBSP when compared to the TI model. For the period with no cloud data (08 Apr 2009 through 11 Nov 2009), the peak SWE from the RTI model is approximately 1.2% higher at SASP and 2.1% lower at SBSP than the TI model. The simulations were repeated using the assumption that the sky was clear during the period without data. In that case, the RTI model is approximately 1.2% higher at SASP and 6.3% lower at SBSP. These differences in peak SWE (especially at SBSP) indicate that the assumption made for missing cloud cover data has significant impacts on the simulation of SWE in the RTI model. Cloud cover also appears to impact the simulated snowpack duration in the RTI model. At SBSP, the TI and RTI models completely melt the snowpack within a week of each other in every WY, with WY 2009 and WY 2012 being the only two years where snow depletion occurred in the RTI model prior to the TI model. At SASP, the RTI model tends to completely melt the snowpack later than the TI model (between thirteen and sixteen days). The exception is WY 2009 when cloud data were not completely available and the RTI and TI model completely melt the snowpack on the same day at SASP. This result also suggests that cloud cover impacts the simulation of SWE in the RTI model.

The impact of dust on SWE is not accounted for in either the RTI or TI model. Skiles et al. (2015) showed an increasing trend in the number of dust events (occurring between March 1st and snow depletion for each calendar year) from 2006 through 2012 at SASP. However, the number of dust events is not a predictor of the amount of dust deposited within a basin (Skiles et al., 2015). Dust concentration (measured just prior to snow depletion) was relatively similar between the calibration and validation periods (ranging from 0.8 to 1.3 mg g^{-1}) for all years except 2009 and 2010, which both experienced greater than 4.0 mg g^{-1} of dust concentration. Of the years analyzed, the observed recession of the SWE for WY 2010 at SASP is quicker than that of the TI or RTI simulations (note that SWE measurements during snow recession are lacking in WY 2009). The rapid recession in observed SWE when compared to simulated SWE is likely caused by the high concentration of dust during WY 2010. Future work could include the impact of dust in the RTI model by modifying the snow albedo (α).

2.4.2 Locations Varying in Aspect and Vegetation Cover

Simulations of SWE at SBSP and SASP yielded very similar results between the TI and RTI models. However, these sites are flat with relatively low vegetation cover. Greater differences in SWE are expected when the topography and vegetation cover play larger roles. To evaluate the sensitivity of the models to these factors, the SWE values from the TI and RTI models were compared for four locations within the basin (locations shown in Figure 4). The four sites were chosen to have similar elevations (between 3493.1 and 3511.4 m), but they have strong differences in their topographic orientation (north-facing vs. south-facing) and their vegetation cover (evergreen forest vs. grassland or bare ground). No further calibration or additional simulations were performed for this analysis; it simply considers other locations in the watershed.

The SWE simulated by the TI model is nearly identical at the four locations (maximum difference of 1.8 cm) because this model does not account for topographic aspect and vegetation cover and the elevation differences between the sites are small. For clarity, a single representative result from the TI model is shown in Figure 8. In contrast, the SWE simulated by the RTI model varies for the four locations. Both north-facing locations typically exhibit higher values of SWE than the TI model throughout the entire simulation due to a reduction in $SW_{\downarrow}$ caused by K_s. The same factor causes the south-facing locations to exhibit lower values of SWE than the TI model. These results demonstrate that the topographic orientation plays a strong role in determining the SWE pattern for mountainous terrain in the RTI model, while this factor is neglected in the TI model.

For both the north-facing and south-facing slopes the forested locations consistently have lower SWE values than the non-forested locations. Differences in SWE due to the forest canopy were caused solely by an increase in $LW_{\downarrow}$ due to the canopy (recall that T_{canopy}=T_a and the emissivity between the canopy and the snow surface, ε_c, is equal to unity for forested areas). The values of K_v were set or calibrated to

1.0 (except for a small portion of deciduous forest), causing no decrease in $SW_{\downarrow}$ due to the canopy cover. No data are available in SBB to determine if snow persists longer in the open or forested areas, but Lundquist et al. (2013) found that snow typically persists longer under the canopy than in the open areas for areas with colder winters. If the K_v values were set lower than unity, $SW_{\downarrow}$ would be reduced under the canopy and snow would persist longer at such locations.

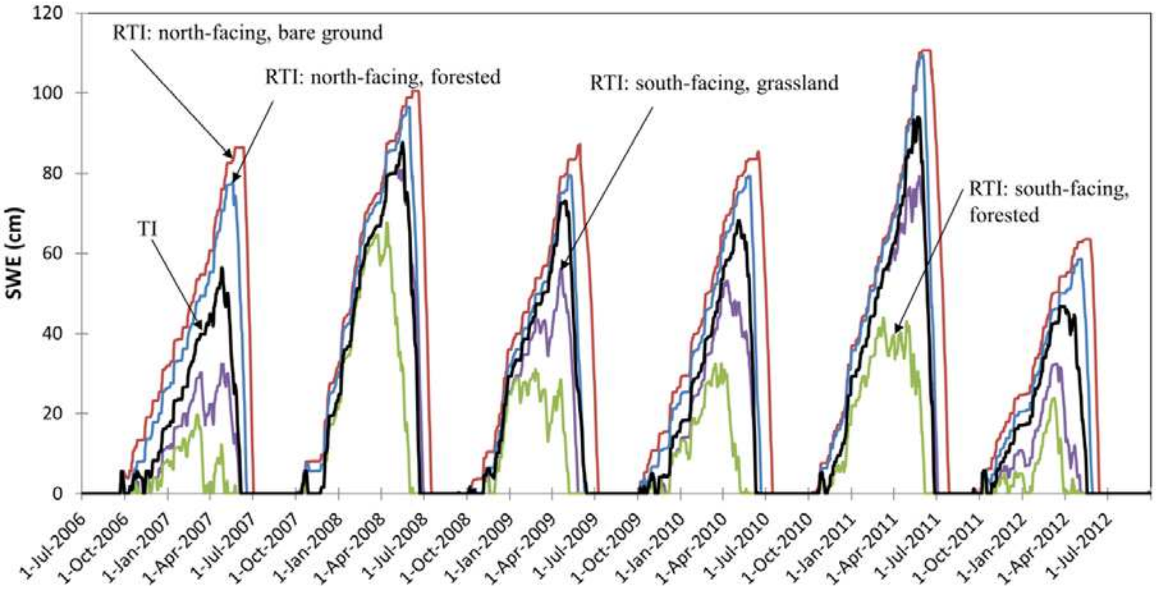

Figure 8. SWE simulation at four locations within SBB that have similar elevations (between 3493.1 and 3511.4 m), but vary in aspect and vegetation cover. The TI model (black) simulates all four sites nearly identically, but the RTI model (colored) simulates each site differently.

2.4.3 Snow Covered Area

Figure 9 and Figure 10 show the LandSat-derived SCA maps along with the SWE maps produced by the TI and RTI models. The 6 images in Figure 9 show the maps from the calibration period, and the remaining 6 images in Figure 10 show the maps from the validation period. The spatial variation in the TI SWE map is only due to variations in elevation, which is used to derive the local T_a. In contrast, the spatial variation in the RTI SWE map depends on elevation, topographic-orientation, and (to a small extent) vegetation cover because they affect T_{rad}. All of the images in Figure 9 and Figure 10 show that there is a clear distinction in how the TI and RTI models simulate spatial patterns of SWE. Qualitatively, the RTI model typically outperforms the TI model in reproducing SCA (e.g., 20 June 2007 and 21 Oct 2011). Skiles et al. (2015) found that dust deposition at SASP advanced melt by 24-49 days. Including dust in the calculation of α in the RTI model could potentially improve SCA simulations at SBB during the ablation period (note overestimation of SCA for 08 May 2009 and 27 May 2010 and recall that both years had high dust concentration (Skiles et al., 2015)).

For the TI simulation, the average error (Eq. (9)) is 0.44 during the calibration period, 0.40 during the validation period, and 0.42 overall. For the RTI simulation, the average error is 0.29 during the calibration period, 0.36 during the validation period, and 0.33 overall. Of the 12 observation dates, the TI and RTI models produced the same error for 2 images (23 Oct 2006 and 24 Sept 2007, both in calibration period), the RTI model had higher error for 1 image (01 July 2011, in validation period), and the RTI model had a lower error for 9 images (4 in calibration period, 5 in validation period). The simulations of SCA were also evaluated using the F score as described in Rittger et al. (2013). The F scores tend to be better for the RTI patterns (average of 0.86) than the TI patterns (average of 0.80), and the F scores also suggest that the RTI SCA is superior for 9 of the 12 observation dates.

Figure 11 analyzes the composition of the error in SCA for each image. Specifically, it shows the percent of the basin where: (1) snow was observed and simulated (accurately simulated snow), (2) snow was not observed and not simulated (accurately simulated no snow), (3) snow was observed but was not simulated (under-simulated snow), and (4) snow was not observed but was simulated (over-simulated snow). During the calibration period, the model was calibrated to minimize the contributions of (3) and (4); cases (1) and (2) represent the accuracy of the models. The average SCA accuracy modestly improves from 75.5% for the TI model to 79.9% for the RTI model with a maximum improvement of 19.7% on 28 Oct 2008 followed by a 14.0% improvement on 8 Nov 2006. Both the TI and RTI models have higher average accuracies for the calibration period (76.6% and 82.9%, respectively) than the validation period

(74.4% and 76.9%, respectively). The improved performance suggests that the RTI model captures some elements of the snowpack evolution that are not included in the TI model. The improvement may be small in part because the RTI introduces much more local variation in the SWE pattern than the TI model.

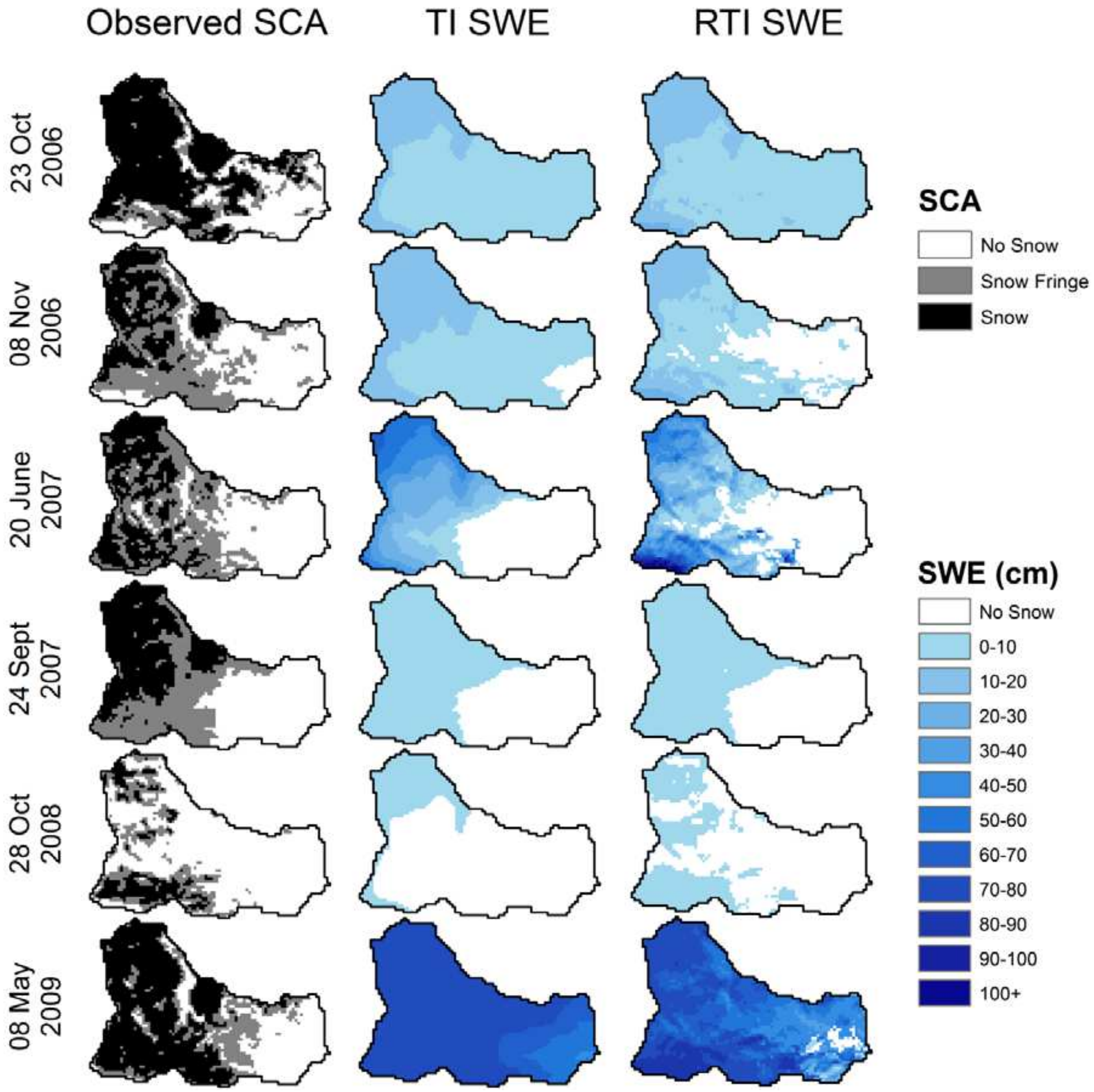

Figure 9. Basin-wide observed SCA (left, from LandSat 5 imagery), and TI (center) and RTI (right) simulated SWE from the calibration period (1 July 2006 – 30 Sept 2009).

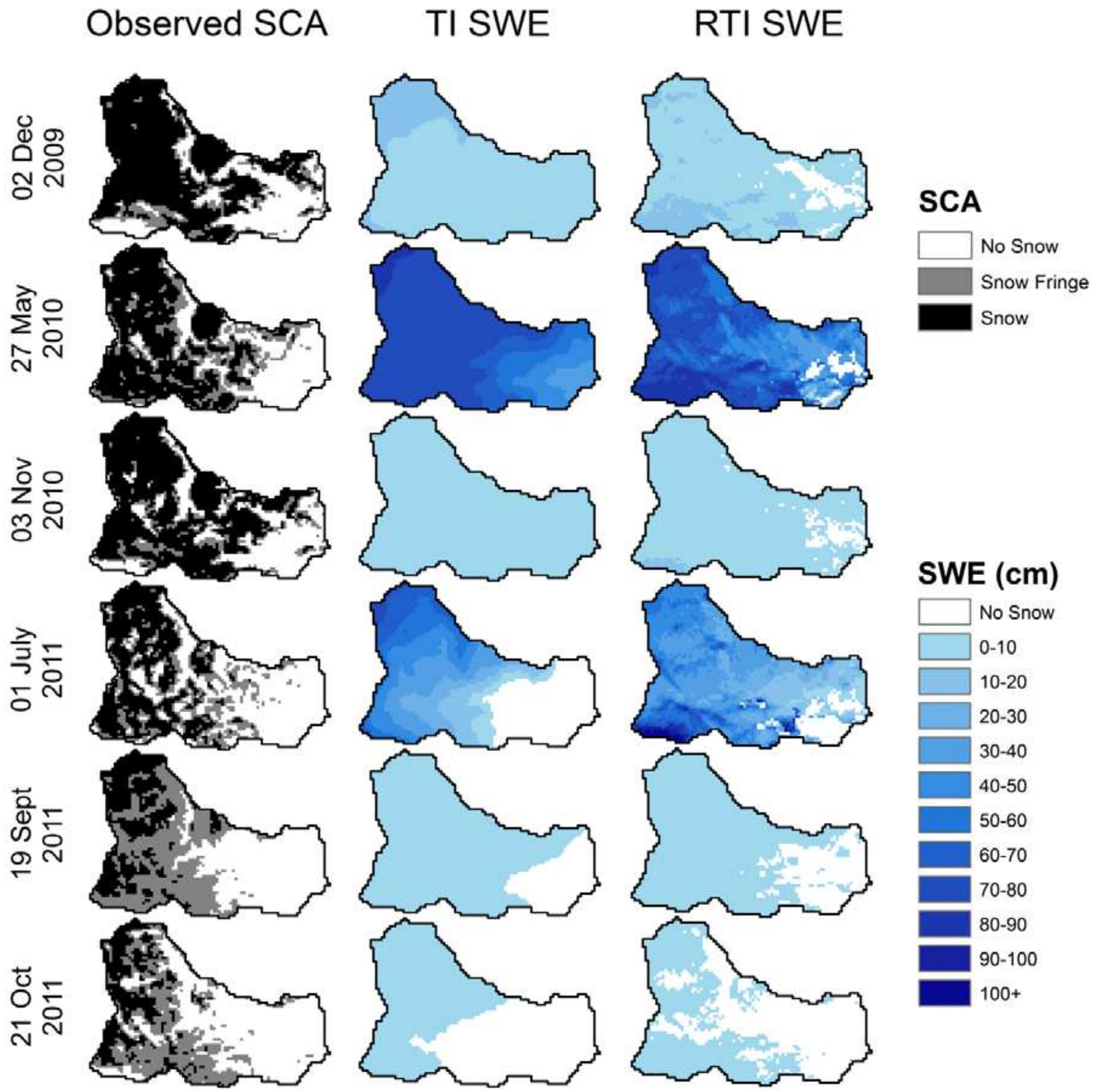

Figure 10. Basin-wide observed SCA (left, from LandSat 5 imagery), and TI (center) and RTI (right) simulated SWE from the validation period (1 Oct 2009 – 30 Sept 2012).

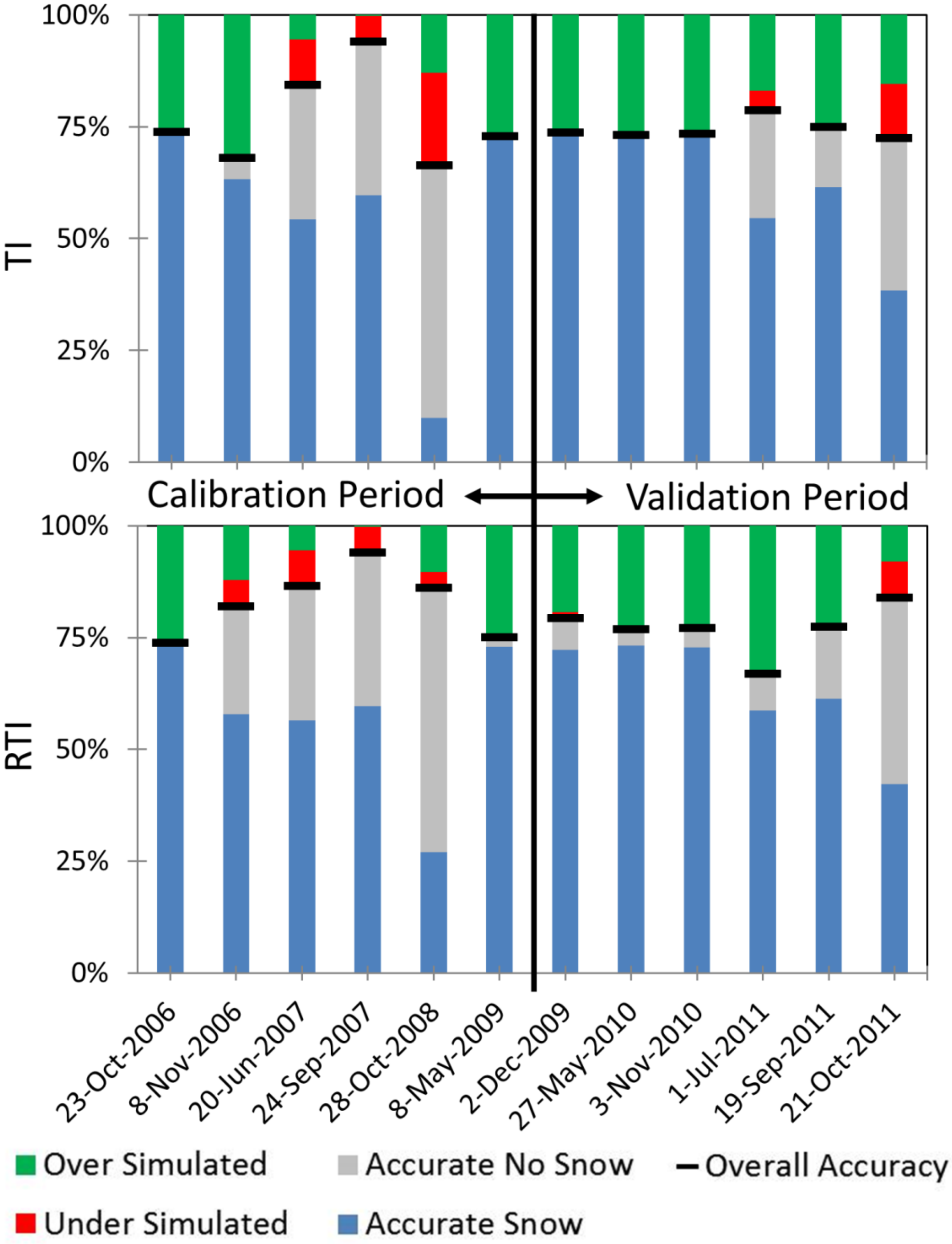

Figure 11. Composition of the SCA from the TI model (top) and RTI model (bottom) as percentages of total basin area. The heights of the black lines indicate the accuracy of the SCA on each date.

2.4.4 Basin-Wide SWE Volume

Basin-wide SWE is often calculated to help plan water allocations and reservoir management. Although no basin-wide SWE observations are available, it is useful to see whether the TI and RTI model produce substantial differences in this quantity. The total volume of SWE (m^3) as a function of time during the simulations is shown in Figure 12 for both the TI and RTI models. During the accumulation periods, both models estimate very similar volumes of SWE. This similarity continues until just prior to the peak in each WY. As melting begins, the TI estimates are typically higher than the RTI estimates. The differences are especially large during the melting period of WY 2009 when the cloud cover was estimated. The difference in the annual peak SWE varied from 53,831 m^3 (2.1% difference) in WY 2008 to a 260,168 m^3 (12.9%) difference in WY 2007. The largest percentage difference occurred in WY 2012 with the RTI model simulating 13.9% (209,268 m^3) less SWE than TI. On average, the annual peak SWE was 187,579 m^3 greater for the TI model than the RTI model (an 8.5% difference). The snowpack completely disappeared in every WY for both the TI and RTI models. Snow in the RTI model disappeared between 8 days (WY 2012) and 37 days (WY 2010) after snow had disappeared in the TI model. This delay (an average of 21.5 days) was caused in part by snow remaining in a few high-elevation topographically-shaded areas within the RTI model.

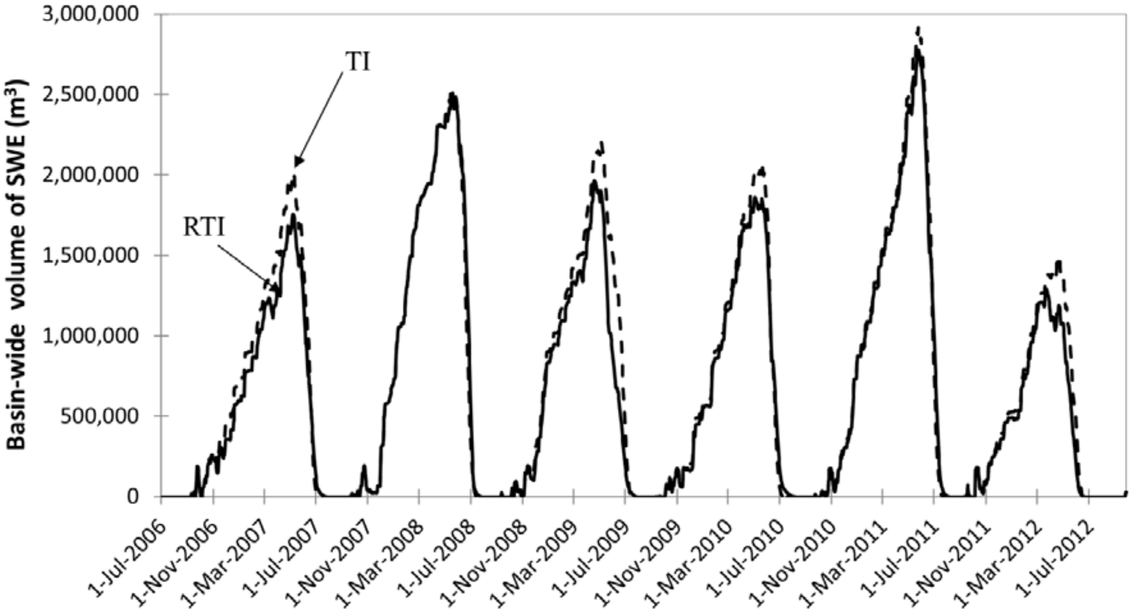

Figure 12. Basin-wide volume of SWE (m^3) simulated by the TI model (dashed) and the RTI model (solid) during the entire study period. Cloud cover was estimated in the RTI model from 08 April 2009 through 11 Nov 2009 due to the lack of cloud cover data.

2.5 Conclusions

This study aimed to better account for the energy that is available to heat or melt snowpack in the GSSHA snowpack routine. The existing TI model uses air temperature as a proxy for the available energy because measurements for this variable are widely available. However, air temperature is most directly related to the longwave radiation from the air (Ohmura, 2001), which is only one contributor in the energy balance. We proposed to replace the air temperature with an alternative proxy, which is calculated from a simple radiation balance. This new RTI model retains the general structure of the TI approach and requires only one additional type of data (cloud cover). The RTI model also includes an estimate of the absorbed shortwave radiation, which is often the dominant source of energy for snow melt (Sicart et al., 2006; DeWalle and Rango, 2008), and it includes the effects of topographic orientation and vegetation cover. Because shortwave radiation is directly considered in the RTI model, two calibrated melt factor terms in the TI model can be replaced with a single melt factor term. To account for vegetation effects, the RTI model does require two inputs related to vegetation: the vegetation transmission coefficient and the leaf area index. However, both of these inputs are currently used in the evapotranspiration routine of GSSHA. Because the RTI model retains the general structure of the TI model, it can easily be implemented into existing distributed models that use the TI model.

In this study, the RTI model was applied to the SBB and compared to local observations of SWE and LandSat-derived maps of SCA. Its results were also compared to the TI model and, at the local scale, to those of the SNTHERM model. The primary conclusions of the paper are as follows:

(1) When the TI and RTI models are calibrated to basin-wide SCA and then applied to the SBSP and SASP sites, they produce similar performance. For example, when compared to observed SWE data, the RTI model has a lower MBE at both sites than the TI model, but a larger RMSE at SASP. Both models perform better at SASP than SBSP, which has known effects from wind scour that are not accounted for in the models. These sites both have little slope and low vegetation cover, so the elements that distinguish the TI and RTI models have little effect. Both methods outperform published results from an uncalibrated SNTHERM model for these sites and produce reasonable estimates of the observed SWE. Thus, at least for this basin, the RTI model appears to have similar performance as the TI model for flat and thinly vegetated locations.

(2) The RTI model produces substantial variations in SWE depending on the topographic orientation and vegetation cover whereas the TI model does not. The RTI model includes the effect of the topographic orientation in its calculation of the absorbed shortwave radiation and thus its proxy temperature. North-facing slopes tend to have more SWE than south-facing slopes. Similarly, when forested and non-forested locations are compared, the non-forested locations have more SWE than the forested locations due to enhanced longwave radiation from the forest cover. The differences between the forested and non-forested locations are expected to be specific to this watershed, and the RTI model likely requires additional data to

ensure accurate representation of these differences. In contrast, the TI model infers its proxy temperature using only elevation and thus exhibits no variations based on topographic orientation or vegetation cover.

(3) The basin-wide SCA area maps from the RTI model are typically more accurate than those from the TI model at SBB, showing improved accuracy in 9 of the 12 images analyzed, similar accuracy in 2 images, and reducing the error from 0.42 to 0.33. The F score (Rittger et al., 2013) modestly improved from 0.8 to 0.86 when using the RTI model. The RTI model's dependence on topographic orientation and vegetation cover produce more local variability in SWE than the TI model. These local variations resemble the variability in SCA maps that are derived from LandSat images. In contrast, the TI model produces very smooth SWE maps that depend only on elevation and often do not resemble the SCA maps from LandSat.

(4) The differences between the TI and RTI models produce substantial differences in the overall volume of SWE in the study basin. The peak basin-wide SWE value in a given water year is 2.1% to 13.9% smaller for the RTI model than the TI model, which could impact water allocation and reservoir operation plans. Although observations are not available to determine which estimate is more accurate, this result suggests that the differences in the TI and RTI models are significant and deserve further testing.

(5) Cloud cover can have a significant effect on the estimation of both shortwave radiation and SWE within the RTI model. During the WY 2009 melting period, cloud cover data were unavailable and therefore estimated hourly by randomly sampling the values from the same day and hour of the other years. This assumption resulted in expedited melting of the snowpack in the RTI model compared to the TI model. It is unclear whether the RTI model can be effectively deployed in basins without observed cloud cover data (perhaps by manipulating calibration parameters such as the melt factor, by calibrating the cloud cover fraction, or using remotely-sensed cloud cover products). Without cloud cover data, the RTI

model still accounts for the effects of topography and vegetation on shortwave radiation and SWE, but its performance is likely diminished.

Additional testing is needed to better characterize the differences between the TI and RTI models. The present study revealed that the most considerable differences occur in locations with substantial topographic and vegetation effects. Future research should focus on comparing to observations in such locations to determine the relative reliability of the two methods. In addition, future testing could determine the magnitude to topographic and vegetation variations that are needed to produce substantial differences between the two methods. Additional testing should also consider the role of cloud cover in more detail. Performance of the RTI model might differ for areas with cloudier climates, such as the Pacific Northwest. Similarly, the performance of the RTI model in basins dominated by turbulent fluxes (e.g., warm temperate mountain climates (Sade et al., 2014)) may be diminished and should be studied. The RTI model also neglects the effects of dust, wind scour, and emission of longwave radiation from local topography; all of which may cause errors in the simulation of SWE and SCA. Dust could be included through a more detailed calculation of snow albedo. Future testing should also examine the performance of the RTI model at predicting the overall volume of SWE in the watershed as well as the timing and magnitude of snowmelt discharges in the spring.

CHAPTER 3. COMPARISON OF RUNOFF SIMULATION USING A MODIFIED-TEMPERATURE-INDEX SNOW METHOD

3.1 Introduction

Volume and timing estimates of snowmelt runoff are vital for water supply and flood forecasting in snow-dominated regions of the world including the western United States (Barros and Lettenmaier, 1993; Wahl, 1992). The shape, peak, and duration of snowmelt runoff are often controlled by the spatial pattern of the snowpack (Luce et al., 1998; Pomeroy et al., 2009), and the large-scale distribution of snowpack is often controlled by elevation, land cover, and slope/aspect (Fassnacht et al., 2017; Jost et al., 2007). Topography (Bloschl et al., 1991; Kirnbauer et al., 1994) and vegetation influence the spatial heterogeneity of the snowpack because they affect the net radiation balance, which is usually the primary energy source for snowmelt (Aguado, 1985). Air temperature and cloud cover (Aguado, 1985; Sicart et al., 2006) also contribute to the net radiation balance, thus affecting the spatial distribution of the snowpack.

Numerical hydrologic models are often employed by water managers and federal agencies (e.g., U.S. Army Corps of Engineers, U.S. Bureau of Reclamation, National Weather Service) to understand and forecast snowmelt runoff within basins. The snowpack within a hydrologic model is simulated using one of two methods: energy balance (EB) or temperature-index (TI). EB approaches solve energy and mass balances within the snowpack as well as the energy transfer across the snow-atmosphere and snow-ground interfaces. These balance equations characterize many of the energy- and mass-fluxes in an attempt to provide accurate spatial representation of the snowpack (Kumar et al., 2013). However, EB approaches require highly-accurate spatiotemporal forcing data (Lei et al., 2007; Franz et al., 2008), which are either unavailable or available at an inadequate spatial resolution for many sites. Because many snow-dominated watersheds have limited forcing data available, TI approaches, such as the

SNOW-17 model (Anderson, 1973; 2006), are often utilized. TI methods utilize air temperature as a proxy for available energy (Anderson, 2006), and melt rates are calculated using the air temperature and an empirical melt factor. Spatial variation of the snowpack in TI methods is often dictated by changes in elevation through a temperature-elevation relationship. Modified-TI snow methods have been proposed in recent years to better account for spatial variations in snowpack due to topography and vegetation while remaining applicable to data-sparse environments (Bookhagen and Burbank, 2010; Cazorzi and Fontana, 1996; Dunn and Colohan, 1999; Hock, 1999; Hock, 2003; Kang, 2005; Kustas et al., 1994; Molotch and Bales, 2006; Shamir and Georgakakos, 2006).

A recent modified-TI method, the Radiation-derived Temperature Index (RTI) method (Follum et al., 2015), uses the framework of an older TI method *SNOW-17* (Anderson, 1973; 2006), but it replaces the air temperature with a calculated proxy temperature. The proxy temperature is derived from a simple radiation balance that is calculated using readily-available elevation, land cover, temperature, and cloud cover data. Use of the RTI method resulted in improved representation of snowpack variability within Senator Beck Basin (SBB) in Colorado (Follum et al., 2015) and Sleepers River experimental watershed in Vermont (Follum et al., 2018). However, neither study considered whether the snowmelt hydrograph differed between using the TI or RTI approaches. Although several examples of modified-TI snow approaches exist, only a few studies (Brubaker et al., 1996; Kustas et al., 1994) compare streamflow production from a modified-TI method and a standard TI method. Kustas et al. (1994) modified a degree-day snow method (a form of TI method) within the snowmelt runoff model (SRM) by including a simple radiation component and found improved melt rates when compared to lysimeter measurements. When combined with a synthetic hydrograph, their results also suggested that the modified-TI snow method would improve hydrograph prediction. When a modified-TI method was used within a semi-distributed version of the SRM model at a watershed in Vermont, the streamflow results (as evaluated with R^2) improved in two of the six years tested and improvements in total flow volume were noted in all six study years (Brubaker et al., 1996). No literature is currently available that has compared streamflow from TI and modified-TI methods using a process-based hydrologic model that is fully-distributed and physics-based. Process-based models are able to isolate variability within a system. For example, the affect that different snowpack simulations have on streamflow could be assessed by keeping all physically-based hydrologic and runoff parameters constant (and set to published values), isolating only the changes in snow simulations. Processed-based models are well-suited for these types of applications because they simulate the physical interaction of hydrologic processes and are less subject to biased parameters arising from intensive calibration (Fatichi et al., 2016). Assessing the differences in runoff production between the TI and modified-TI snow methods is important since the use of more complex methods, such as the modified-TI snow method, could be utilized by water managers if shown to improve the timing and volume of the hydrograph, which would affect planning and reservoir operation.

The purpose of this paper is to test and compare snowmelt hydrographs simulated using a TI and a modified-TI snow method in a processed-based hydrologic model to determine if use of the modified-TI snow method leads to improved simulation of streamflow. Further, to determine how the TI and modified-TI snow methods perform using different calibration data, snowpack (SWE and SCA) and the resultant streamflow simulations are compared when the TI and modified-TI methods are calibrated using only SWE measurements or SCA images. This test is completed to determine how the type of calibration data (SWE or SCA) affects the snow and streamflow accuracy when using each snow method. The TI and RTI approaches for snow simulation are tested within the Gridded Surface Subsurface Hydrologic Analysis (GSSHA) (Downer and Ogden, 2004) model. GSSHA is a fully-distributed, process-based hydrologic model that includes both overland- and channel-routing processes as well as movement of meltwater vertically and laterally through the snowpack. SBB is used as the test location because it has available forcing, SWE, SCA, and streamflow data. SBB is also well-suited for our purposes because the basin is predominantly rock with limited infiltration of runoff as it travels to the outlet, allowing several elements of the basin response aside from snowmelt to be constrained or omitted. Four scenarios are explored using the GSSHA model with results compared to observed snow and streamflow data. The first two scenarios utilize the TI snow method alone. In scenario 1, the snow parameters are calibrated using point snow data from two sites, while in scenario 2, the snow parameters are calibrated using basin-wide SCA maps. Scenarios 3 and 4 are identical to scenarios 1 and 2, respectively, but use the RTI snow method instead of the TI snow method. The performance of each scenario is compared to SWE observations at the two point locations, 12 images of SCA derived from LandSat 5 imagery, and streamflow measurements at the outlet of SBB for water year (WY) 2007-2012.

3.2 Study Area

SBB is a 2.9 km^2 research watershed in the San Juan Mountains in southwestern Colorado with elevations ranging from 3362 m to 4118 m (Gesch et al., 2002). The SBB land surface is predominantly rock, specifically rock outcrops, rubble, and some well-draining rock formations (Soil Survey Staff, Natural Resources Conservation Service, United States Department of Agriculture, Soil Survey Geographic (SSURGO) Database, available online at https://sdmdataaccess.sc.egov.usda.gov. Accessed 28 May 2014). Land cover classifications at SBB are mostly barren land (27% of basin), grassland (62% of basin), and some deciduous and evergreen forest below 3600 m (Fry et al., 2011) (Figure 13).

SBB is monitored by the Center for Snow and Avalanche Studies (CSAS) (more information provided by Landry et al. (2014)). Precipitation data are measured hourly at the Swamp Angel Study Plot (SASP), which is located at an elevation of 3371 m in a nearly level forest clearing that provides some shelter from wind. Temperature data are measured hourly at both SASP and the Senator Beck Study Plot (SBSP), which is located at an elevation of 3714 m in a nearly level section of alpine tundra that is exposed to the effects of wind. SWE, snow depth, and snow density are measured regularly (monthly in early winter and weekly in late winter and spring) using formal snow cover profiles at SASP and SBSP (see Landry et al. 2014). Streamflow data are collected every 5 seconds at the SBB outlet by CSAS from late winter through late fall using a broad-crested notched weir. The streamflow data were post-processed to hourly and daily timesteps and are available on the CSAS website (https://snowstudies.org/archived-data/. Accessed 18 June 2018).

Thirty-two SCA maps of SBB are also available from LandSat 5 imagery (Follum et al., 2015) during the study period of 1 July 2006 through 30 Sept 2012. Each SCA image has a 30 m resolution with each pixel classified as snow, no-snow, or snow fringe (transition between snow and no-snow). SCA images that show periods of accumulation or ablation have higher value in testing the models. Of the 32 available SCA images, 12 images have snow coverage between 25% and 75% and are used in this study.

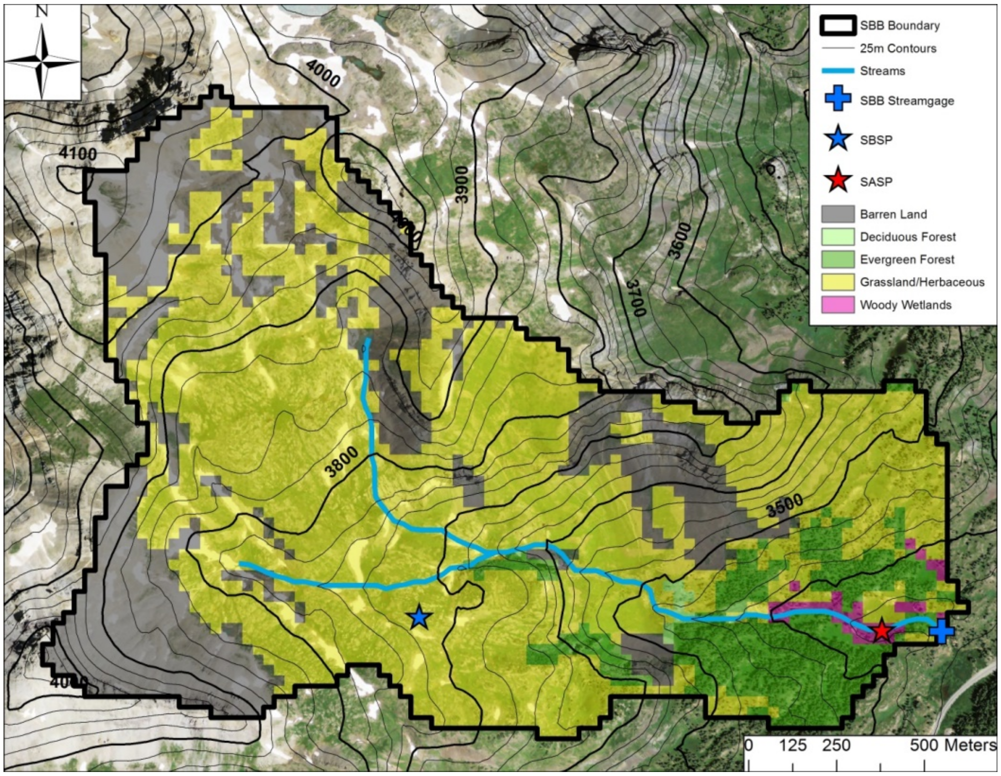

Figure 13. Elevation contours (black lines) and land cover classifications (shading) overlaid on orthoimagery of the Senator Beck Basin in Colorado, USA. The two snow measurement sites (stars), stream channels (blue lines), and outlet (plus symbol) are marked. Elevation contours are from the 1/3-arc-second (~9 m) National Elevation Dataset (Gesch et al., 2002), and land cover classifications are based on the 2006 National Land Cover Database (Fry et al., 2011). Stream locations were determined using the National Elevation Dataset and the Watershed Modeling System (Aquaveo, 2013). The background image was obtained from United States Geological Survey 1-m orthoimagery data and was used to help define starting locations of streams.

3.3 Modeling Methodology

3.3.1 TI Method

Follum and Downer (2013) implemented the TI method (based on SNOW-17 (Anderson, 1973; 2006)) in GSSHA. SNOW-17 was originally formulated using a 6 hour time step, but model parameters can be adjusted to utilize other time steps (Anderson, 2006). GSSHA uses an hourly time step (Δt) for snow simulation where hourly hydrometeorological forcing data are applied on a structured, square grid. A central variable in most snow methods is air temperature T_a (°C), which can vary for each cell based on the elevation of the cell (E_c, m) using a lapse rate ϑ (°C m^{-1}):

$$T_a = T_g + \vartheta\,(E_g - E_c), \qquad (21)$$

where E_g (m) and T_g (°C) are the gage's elevation and temperature reading, respectively.

Precipitation P (m hr^{-1}) accumulates as snow water equivalent (SWE, m) within each cell when T_a falls below a threshold temperature T_h (°C). Although values for T_h can vary in time and space (Fassnacht and Soulis, 2002; Fassnacht et al. 2013), T_h is often set between -2°C and 2°C (Anderson, 1973; He et al., 2011) and is therefore set to 0°C in this study. Not all precipitation reaches the ground surface. An effective precipitation P_{eff} (m hr^{-1}) indirectly accounts for interception, sublimation, and redistribution of snow and is determined by multiplying P by a calibrated factor (S_{cf}) (Anderson 2006). Melting of the snowpack occurs once the heat deficit (cold content) of the snowpack is overcome. As described in Anderson (2006), changes in heat deficit are calculated hourly using T_a, P_{eff}, the daily melt factor M_f (mm °C^{-1} (Δt)$^{-1}$), and three calibration parameters: the antecedent snow temperature index A_{TIPM} (fraction), the maximum melt factor $M_{f,max}$(mm °C^{-1} (6 h)$^{-1}$), and maximum negative melt factor $N_{Mf,max}$ (mm °C^{-1} (6 h)$^{-1}$). The daily melt factor M_f is calculated as:

$$M_f = (\Delta t/6)\left[S_v A_v\left(M_{f,max} - M_{f,min}\right) + M_{f,min}\right], \qquad (22)$$

where S_v accounts for seasonal melt variation based on Julian day, A_v is a seasonal melt variation adjustment based on latitude and Julian day, and $M_{f,min}$ is the calibrated minimum melt factor (mm °C^{-1} (6 h)$^{-1}$).

Under normal conditions, the amount of melt M (mm of SWE) is calculated as:

$$M = \left[M_f(T_a - T_{mbase}) + 0.0125P_{eff}f_rT_r\right]\Delta t, \tag{23}$$

where f_r is the fraction of precipitation falling as rain (set equal to 0 when $T_a \leq T_h$, otherwise set to 1), T_r (°C) is the precipitation temperature (set equal to the greater of T_a and 0°C), and T_{mbase} (°C) is the temperature at which melt begins (set to 0°C) (default f_r, T_r, T_{mbase} values are set based on Anderson (1973)). During rain-on-snow events (greater than 1.5 mm of rainfall in a 6 h period) a simple energy balance is used to calculate M as:

$$M = \sigma\left[(T_a + 273)^4 - 273^4\right]\Delta t + 0.0125P_{eff}f_rT_r + 8.5f_u(\Delta t/6)[(r_he_{sat} - 6.11) + 0.00057P_aT_a], \tag{24}$$

where σ is the Stefan-Boltzmann constant and f_u is the average wind function (a parameter, mm mb^{-1} (6 h)$^{-1}$). Atmospheric pressure P_a (mb) is estimated from elevation (Anderson, 2006), relative humidity r_h (fraction) is set to 0.9 during rain events (Anderson 2006), and saturation vapor pressure e_{sat} (mb) is calculated based on T_a (Smith 1993).

Water can begin to leave the snowpack once the snowpack becomes ripe. In the TI method the snowpack is considered ripe when the ratio of meltwater held by the snowpack (W_q, mm) to the ice in the snowpack (W_i, mm) exceeds the liquid water holding capacity L_h (calibrated fraction not to exceed 0.4 (Anderson, 2006)). Once L_h is surpassed, excess water (E, mm) within the snowpack moves vertically through the ripe snowpack using an empirical lag and attenuation method described in Anderson (2006). The lag time for excess water to begin leaving the snowpack (L, h) is calculated:

$$L = 5.33\left[1.0 - e^{(-0.03(\Delta t/6)W_i)/E}\right]. \tag{25}$$

The hourly withdrawal rate R (hr^{-1}) for meltwater to leave the snowpack and go to the land surface is calculated as:

$$R = \left[1 + 5\, e^{-500\, \left(E_l/(25.4\, A_s)\right)/\left(W_i/(25.4\, A_s)\right)^{1.3}}\right]^{-1}, \tag{26}$$

where E_l (mm) is the hourly lagged excess liquid water available during the current time step (based on Equation 25). A_s is the fractional area of the cell covered by snow, set to 1 because GSSHA does not account for partial snow covered area within a cell (if snow is within a cell it is assumed to cover the entire cell). E_l and the previously stored excess liquid water held within the snowpack, S_l (mm), are multiplied by R (hr^{-1}) to determine the volume of meltwater released to the land surface.

3.3.2 RTI Method

The RTI method follows the same structure as the TI method but replaces T_a in Eq. (23) and (24) with a radiation-derived proxy temperature T_{rad} (°C). In those equations, T_a is used to represent the energy available to melt the snowpack. While T_a is most closely related to incoming longwave radiation from the air (Ohmura, 2001), T_{rad} considers both longwave and shortwave radiation. If radiation terms are assumed to dominate the energy balance at the snow surface, the energy balance can be approximated as:

$$R_a = R_{SW,net} + R_{LW\downarrow}, \tag{27}$$

where R_a (W m^{-2}) is available energy at the snow surface, $R_{LW\downarrow}$ (W m^{-2}) is incoming longwave radiation, and $R_{SW,net}$ (W m^{-2}) is net shortwave radiation. Equation 27 neglects turbulent heat fluxes as well as outgoing longwave radiation from the snowpack.

R_a can be represented as a temperature (i.e. T_{rad}) by use of the Stefan-Boltzmann Law:

$$T_{rad} = \left(\frac{R_a}{\varepsilon_{snow}\, \sigma}\right)^{1/4} - 273.15, \tag{28}$$

where σ is the Stefan-Boltzmann constant and ε_{snow} is the emissivity of snow (commonly set to 0.97 (Jin et al., 2006; Walter et al., 2005)).

Both $R_{SW,net}$ and $R_{LW\downarrow}$ are rarely measured operationally in snow-dominated watersheds, and are therefore estimated. $R_{SW,net}$ can be calculated as:

$$R_{\mathrm{SW,net}} = (1 - \alpha_s)R_{\mathrm{SW}\downarrow}, \tag{29}$$

where $R_{\mathrm{SW}\downarrow}$ is the incoming shortwave radiation (W m^{-2}) and α_s is the albedo of the snowpack, which is calculated daily based on the time since most recent snowfall and whether the snow is melting (description of method in Henneman and Stefan (1999)). $R_{\mathrm{SW}\downarrow}$ can be calculated using an assumed solar constant $R_{SW,0}$ (set to 1366 W m^{-2} from Liou (2002)) as described in Follum et al. (2015):

$$R_{\mathrm{SW}\downarrow} = R_{\mathrm{SW,0}}\, \varphi_r\, \varphi_{atm}\, \varphi_c\, \varphi_v\, \varphi_s\, \varphi_t, \tag{30}$$

where the φ variables are reductions due to the distance from the Earth to the sun (φ_r), atmospheric scattering (φ_{atm}), absorption by the clouds (φ_c), shading from vegetation (φ_v), slope and aspect of the terrain (φ_s), and shading from topographic features (φ_t). φ_r, φ_{atm}, φ_s, and φ_t are estimated based on time of year and elevation data (TVA, 1972; Allen et al., 2005; Duffie and Beckman, 1980; Follum et al., 2015). Following Follum et al. (2015), φ_v is set equal to the vegetation transmission coefficient K_v (Bras (1990) provides a table of K_v values for various vegetation types). φ_c is estimated using fractional cloud cover measurements N as described in TVA (1972). $R_{LW\downarrow}$ is estimated as (TVA, 1972; Liston and Elder, 2006):

$$R_{LW\downarrow} = \sigma\varepsilon_a(T_a + 273.15)^4(1.0 + 0.17\, N^2)(1 - F_c) + F_c\sigma\varepsilon_c\left(T_{canopy} + 273.15\right)^4, \tag{31}$$

where ε_a is the air emissivity (assumed 0.757 when snow is present (Bras, 1990)), ε_c is the canopy emissivity (assumed 1.0 based on Sicart et al. (2004)), F_c is the fractional canopy cover (calculated using leaf area index L_{AI} based on Liston and Elder (2006) and Pomeroy et al. (2002)), and T_{canopy} (°C) is the canopy temperature (assumed equal to T_a based on DeWalle and Rango (2008)).

Another difference between the TI and RTI methods is how M_f is determined. The TI method accounts for seasonal changes by adjusting S_v and A_v in the calculation of M_f in Equation 22. M_f in Equation 22 can range between $M_{f,min}$ and $M_{f,max}$, corresponding to the times of year with minimum and maximum melt. As shown in Follum et al. (2015), these times of minimum and maximum melt correlate to minimum and maximum exposure to $R_{\mathrm{SW}\downarrow}$. Because T_{rad} includes $R_{\mathrm{SW}\downarrow}$, M_f is a static calibration parameter in the RTI method (for more details see Follum et al. (2015)).

3.3.3 Surface Hydrology

Meltwater at the ground surface can be infiltrated, evaporated, ponded, or routed to the outlet of the basin. Routing of meltwater laterally through the snowpack and over the land surface are expected to be important processes in simulating basin outflow at SBB and are discussed in detail below. Three simplifications are made regarding surface hydrology at SBB. First, evaporation from the runoff in SBB is assumed to be minimal because snowmelt runoff moves quickly through the relatively small and steep basin that has no detention basins (e.g., lakes), limiting the exposure for the runoff to evaporate. Second, infiltration is assumed to play a minor role in snowmelt runoff estimation at the outlet of SBB and is not simulated. Soil is typically thin in the bare rock and tundra above 3700 m, with thicker soil layers in the subalpine forest areas at the lower elevations (< 3600 m) of the basin (Landry et al., 2014) (Figure 13). The soil quickly saturates in the late spring and summer when the snowpack begins to melt (Landry et al., 2014), resulting in direct runoff as overland flow. Third, base flow is not simulated because at SBB it is minimal (Landry et al., 2014) compared to the runoff generated by the spring and summer snowmelt.

If snow is present within a cell, GSSHA simulates lateral flow along the bottom of the snowpack using Darcy's law, as described in Colbeck (1974):

$$q_{snow} = \propto k_s \Phi g_c \mathrm{H}, \tag{32}$$

where q_{snow} ($\mathrm{m}^3\ \mathrm{s}^{-1}$) is the lateral flow of meltwater through the snowpack, $\propto$ is a hydraulic constant for water ($\propto = 5.47 \times 10^6\ \mathrm{m}^{-1}\ \mathrm{s}^{-1}$ based on Colbeck (1974)), k_s is the saturated permeability of the snowpack (estimated as $25 \times 10^{-10}\ \mathrm{m}^2$ based on Colbeck and Anderson (1982)), Φ is the downward slope between cells, g_c (m) is the grid cell resolution (the width over which flow occurs), and H (m) is the thickness of the saturated layer, calculated as the depth of surface water divided by the porosity of the snowpack θ (m^3 m^{-3}). θ varies based on the condition (fresh snow, ripe snowpack, etc.) of the snowpack and can be calculated using a snow density model, but in this study is set to 0.67 (the default value for fresh or refrozen snow in the SNTHERM model (Jordan, 1991)). Equation 32 assumes the bottom of the snowpack is saturated and homogeneous and that the elevation gradient dictates the hydraulic gradient. If snow is not present within a cell, GSSHA employs a two-dimensional overland flow routing method to convey excess-runoff (i.e. meltwater) over the land surface and to the outlet of the basin. Overland flow fluxes $q_{x,y}$ (m^3 s^{-1}) between cells are calculated using a diffusive wave approach, where Manning's equation is solved for the head-gradient discharge relationship in the x and y directions following Julien and Saghafian (1991). Once water reaches a stream channel (channel locations are identified in the model set-up) water can flow from the overland into the channel network, where it is routed to the outlet using a one-dimensional diffusive-wave equation. More information is available from Downer and Ogden (2004; 2006).

3.4 Model Application

The GSSHA model for SBB was developed using the Watershed Modeling System software (Aquaveo, 2013). A 30-m structured grid (g_c=30 m) was defined for the basin (3207 cells), which captures much of the spatial heterogeneity of the basin while remaining computationally efficient. The elevation for each grid cell was sampled from the 1/3-arc-second (~9 m) National Elevation Dataset (Gesch et al., 2002), and land cover classifications were obtained from the 2006 National Land Cover Database (Fry et al., 2011). The stream network was developed within the Watershed Modeling System using the elevation dataset. Orthoimagery was also used to identify the threshold for stream initiation. The streams were assumed to be trapezoidal with a bottom width of 4 m, a bank full depth of 2 m, and a side slope of 1.

Tests showed for this small basin that as long as water remained in the channel the dimensions of the trapezoidal channel (bottom width and bank full depth) had minor effect on the outflow of the stream.

An hourly lapse rate was calculated and air temperature values were applied to each grid cell using Equation 21. Although cold-air pooling can occur in the valleys in SBB causing a local temperature inversion, it is expected that these inversions are localized and therefore lapse rate values (ϑ) were limited to between 0.0 and 0.00981 °C m^{-1}. Cloud cover classifications (clear, scattered, overcast, etc.) are available at most airports in the United States from the National Centers for Environmental Information (NCEI, https://www.ncdc.noaa.gov/). Cloud cover classifications from Telluride Regional Airport were collected and converted to percentages (from 0% for clear to 100% for overcast), as described in Follum et al. (2015). From 08 April 2009 through 11 November 2009 cloud cover classifications were unavailable and were therefore estimated by randomly sampling the observations from the same day and hour during the other years.

All parameters related to hydraulic routing of runoff were set to published values. GSSHA requires Manning's roughness coefficients for overland flow (n_{ov}, s $m^{-1/3}$) and channel flow (n_{ch}, s $m^{-1/3}$). The n_{ov} value of each cell was set to the roughness coefficient in Downer and Ogden (2006) that corresponds to the land cover classifications of the cell. n_{ch} was set to 0.040 s $m^{-1/3}$, the recommended value for mountain streams in Chow (1959).

Snow parameters within the TI and RTI snow methods were calibrated using two different approaches: 1) to match point SWE measurements in the watershed (TI Point and RTI Point), and 2) to match SCA maps for the entire watershed (TI Spatial and RTI Spatial). In both cases, the snow parameters within the TI and RTI methods were calibrated using the Model-Independent Parameter Estimation and Uncertainty (PEST) method (Doherty et al., 1994). PEST calibrates numerous parameters simultaneously to minimize the sum of the squared residuals between simulated and observed values. When calibrating to SWE measurements (called the TI Point and RTI Point scenarios), the residuals (ϵ) were set to the difference between each observed and simulated SWE value. When calibrating to SCA observations (called the TI Spatial and RTI Spatial scenarios), ϵ was calculated for each observed SCA image as follows (Follum et al., 2015):

$$\epsilon = \frac{A_{over} + A_{under}}{A_{obs}}, \quad (33)$$

where A_{over} is the area where the model simulates snow but no snow is observed, A_{under} is the area where snow is observed but not simulated in the model, and A_{obs} is the total area with observed snow. An ϵ value of 0 indicates a perfect fit between simulated and observed SCA. The calibration period is water year (WY) 2007 - 2009. The validation period is WY 2010 - 2012.

Table 3 shows the allowable range, calibrated value, and sensitivity ranking for each snow parameter for the TI and RTI methods under the two calibration scenarios. Except for S_{cf}, the lower limit of the parameter values is set to 0.001 (as close to the physical limit of 0 as allowed by the software). The upper limits of parameter values are based on physical limits (Anderson, 2006) and typical values from the field (Gerdel, 1954; Singh et al., 1997). The value for K_v differs for each land cover type and has a physical range between 0 (fully canopy coverage) and 1 (no canopy coverage). K_v for evergreen forest $K_{v,evergreen}$ is set to 1 in this study following Follum et al. (2015). At Sleepers River Experimental Watershed in Vermont (a predominantly deciduous forest) Follum et al. (2018) set K_v for deciduous forest $K_{v,deciduous}$ equal to 0.969 (most sensitive parameter when using the RTI method). The deciduous forest is sparse at SBB and has limited canopy in the winter, therefore $K_{v,deciduous}$ is set to 1 in this study. L_{AI} values for evergreen and deciduous forests were set to 2.5 and 0.5, respectively, following recommendations by Liston and Elder (2006).

Table 3. Allowable range and calibrated values from PEST for the TI Point, TI Spatial, RTI Point, and RTI Spatial model parameters. Dashes indicate parameters that are not required and values in parentheses after the calibrated values indicate sensitivity ranking of the parameter.

Parameter	Units	Allowable Range	Calibrated Values TI Point	TI Spatial	RTI Point	RTI Spatial
$M_{f,\ max}$	mm °C^{-1} (6 hr)$^{-1}$	0.001-2.400	0.744 (2)	0.843 (1)	--	--
$M_{f,\ min}$	mm °C^{-1} (6 hr)$^{-1}$	0.001-1.600	0.491 (6)	0.405 (2)	--	--
M_f	mm °C^{-1} (6 hr)$^{-1}$	0.001-2.400	--	--	0.405 (3)	0.175 (1)
NMF	mm °C^{-1} (6 hr)$^{-1}$	0.001-2.400	1.252 (3)	1.947 (4)	2.400 (2)	0.499 (3)
f_u	mm mb^{-1} (6 hr)$^{-1}$	0.001-1.000	0.500 (7)	0.500 (6)	0.500 (6)	0.500 (5)
$TIPM$	fraction	0.001-1.000	0.724 (4)	0.217 (5)	0.774 (4)	0.699 (4)
L_h	fraction	0.001-0.100	0.059 (5)	0.046 (6)	0.039 (5)	0.037 (5)
S_{cf}	fraction	0.800-1.000	0.913 (1)	0.803 (3)	0.981 (1)	0.800 (2)

Table 3 shows that S_{cf} is one of the most sensitive parameters in both the TI and RTI methods. The models that were calibrated to SCA (TI Spatial and RTI Spatial) have S_{cf} values at or near the minimum, while the models calibrated to SWE (TI Point and RTI Point) have S_{cf} values closer to the initial value of 1. f_u is the least sensitive of the parameters in all of the models. f_u is only important when the basin experiences frequent rain-on-snow events with relatively warm temperatures (Anderson, 2006), which are infrequent in the high-elevation SBB.

3.5 Results and Discussion

The results from the four models are analyzed in three ways: 1) comparison to observed SWE measurements at SASP and SBSP; 2) comparison of 12 satellite-derived SCA images to SWE patterns for the entire basin; and 3) comparison between simulated and observed flowrates at the outlet of SBB. All three analyses allow a comparison of the two calibration approaches, while the third analysis allows a comparison of the TI and RTI methods in terms of the streamflow produced.

3.5.1 SWE Simulation at SASP and SBSP

Figure 14 shows the SWE values from the two TI models (TI Point and TI Spatial) and the two RTI models (RTI Point and RTI Spatial) compared to observed SWE at SASP and SBSP. TI Point and RTI Point perform similarly, and the TI Spatial and RTI Spatial perform similarly. Both SASP and SBSP are located in areas with little slope and minimal vegetation cover, which are two characteristics that can cause T_{rad} to deviate from T_a in the RTI method. Therefore, differences between the TI and RTI models are small at SASP and SBSP. The TI and RTI models calibrated to SWE and SCA perform similarly, with the main difference being the models calibrated to SCA often simulate lower SWE estimates at both SASP and SBSP.

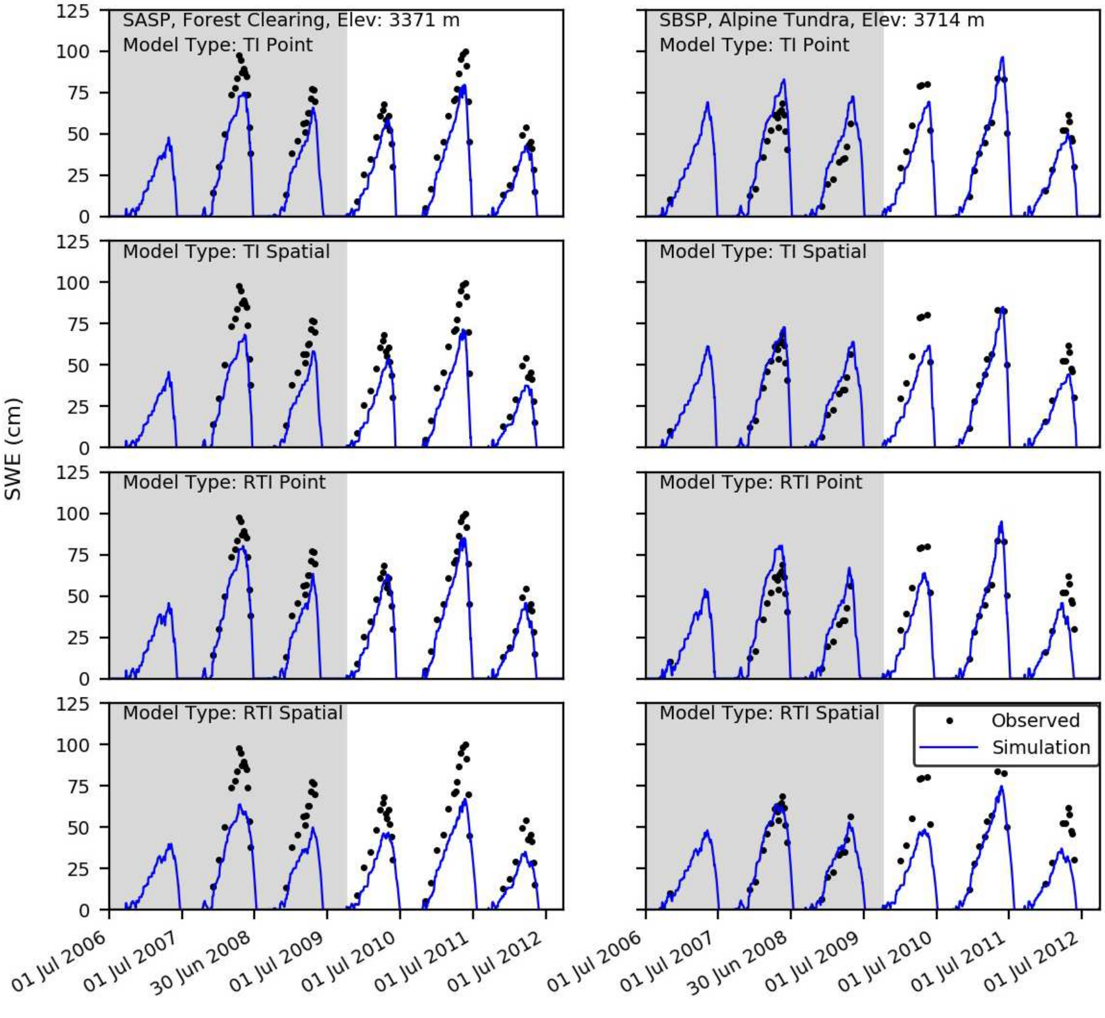

Figure 14. Simulated (TI Point, TI Spatial, RTI Point, and RTI Spatial) and observed SWE at SASP (left) and SBSP (right). Gray shading indicates calibration period.

Table 4 shows the root mean squared error (RMSE) and mean bias error (MBE) of the simulated SWE. All four models underestimate SWE at SASP (indicated by negative MBE values), while they simulate SBSP more accurately (overall RMSE and MBE values are closer to zero). Statistically, the TI Point and RTI Point perform similarly, and the TI Spatial and RTI Spatial perform similarly. At SASP, the models calibrated to SWE produce more accurate SWE values than the models calibrated to SCA. However, at SBSP, the models calibrated to SCA outperform the models calibrated to SWE during the calibration period. The lower estimates (lower or negative MBE values) of SWE using TI Spatial and RTI spatial improve accuracy at SBSP during the calibration period, but then cause more severe underestimation of SWE during the validation period.

Table 4. Root mean squared error (RMSE) and mean bias error (MBE) for the TI Point, TI Spatial, RTI Point, and RTI Spatial SWE values at SASP and SBSP during the calibration period (1 July 2006-30 September 2009), validation period (1 October 2009-30 September 2012), and both periods combined.

			TI Point	TI Spatial	RTI Point	RTI Spatial
SASP	Calibration	RMSE (cm)	13.4	19.6	12.6	23.1
		MBE (cm)	-12.1	-18.4	-11.2	-20.8
	Validation	RMSE (cm)	11.7	16.8	8.9	17.6
		MBE (cm)	-8.5	-13.6	-6.0	-14.4
	Overall	RMSE (cm)	12.4	18.0	10.6	20.0
		MBE (cm)	-10.0	-15.6	-8.1	-17.0
SBSP	Calibration	RMSE (cm)	13.8	7.6	12.7	4.8
		MBE (cm)	12.0	5.5	11.1	1.4
	Validation	RMSE (cm)	9.9	13.0	16.9	19.3
		MBE (cm)	-4.5	-9.9	-11.7	-15.7
	Overall	RMSE (cm)	12.0	10.7	15.0	14.2
		MBE (cm)	3.6	-2.4	-0.5	-7.3

3.5.2 Snow Cover Area

Figure 15 shows the satellite-derived SCA and the simulated (TI Point, TI Spatial, RTI Point, and RTI Spatial) SWE maps for both the calibration and validation periods. The TI Point and TI Spatial SWE maps vary spatially with elevation because T_a varies only with elevation (Equation 21). The RTI Point and RTI Spatial SWE maps vary spatially due to elevation, topographic orientation, and (to a small extent) vegetation cover because these properties are included in the calculation of T_{rad}. The TI Point and TI Spatial models show a similar snow pattern in most of the images, while the RTI Point tends to have less extensive snowpack than the RTI Spatial.

Each SCA image was used to quantify the percentages of the basin where snow was accurately simulated (Accurate Snow), snow was accurately not simulated (Accurate No Snow), snow was observed but not simulated (Omission Error), and snow was simulated but not observed (Commission Error). SCA Accuracy was calculated as the sum of the Accurate Snow and Accurate No Snow percentages (Table 5). The RTI model performs best in Overall SCA Accuracy. The RTI Point model is more accurate in 7 of the 12 SCA images when compared to the TI Point model. The RTI Spatial is more accurate than the TI Spatial model in 8 of the 12 SCA images and has the same accuracy in 1 of the 12 images. The largest difference in accuracy between the RTI Spatial and TI Spatial models is 21% on 28 Oct 2008. Using SCA to calibrate the TI and RTI models results in only minor improvement using the RTI model when compared to calibrating using SWE measurements. The RTI Spatial model has an Overall SCA Accuracy of 77% compared to 76% using the RTI Point model. The TI Point and TI Spatial models perform the same in SCA Accuracy for each image with the exception of 1 July 2011 and 21 Oct 2011, resulting in the same Overall SCA Accuracy of 74%.

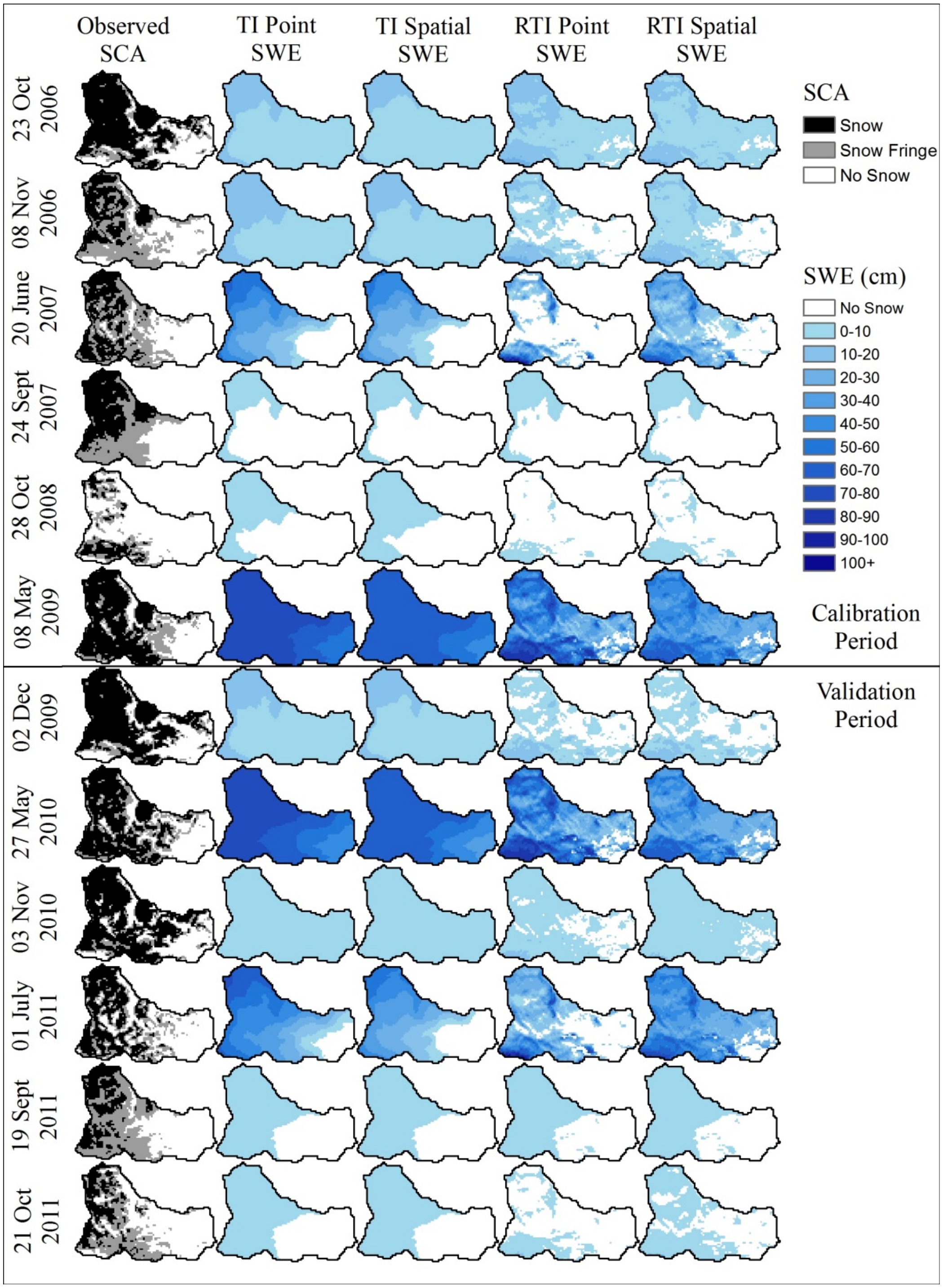

Figure 15. Satellite-derived SCA images (left) and corresponding maps of simulated SWE (TI Point, TI Spatial, RTI Point, and RTI Spatial) from the calibration period (1 July 2006-30 September 2009) and the validation period (1 October 2009-30 September 2012).

Table 5. SCA Accuracy of the TI Point, TI Spatial, RTI Point, and RTI Spatial SCA maps during each WY, the calibration period (1 July 2006-30 September 2009), validation period (1 October 2009-30 September 2012), and overall. WY 2008 had no SCA observations.

	TI Point	TI Spatial	RTI Point	RTI Spatial
WY 2007	80%	80%	77%	83%
WY 2008	--	--	--	--
WY 2009	67%	67%	77%	79%
WY 2010	73%	73%	71%	73%
WY 2011	71%	71%	80%	70%
WY 2012	72%	74%	68%	76%
Calibration	76%	76%	77%	82%
Validation	72%	72%	75%	72%
Overall	74%	74%	76%	77%

3.5.3 Flow Simulations

Analysis of flow simulations for each WY start when streamflow measurements at the outlet of SBB begin in early spring (typically March or April). The analysis stops a day prior to any rainfall event that is expected to dominate the streamflow response. Such rainfall events are defined as occurring after 15 July and exceeding 14 mm d^{-1}. The only WY that does not have such a rainfall event is WY 2011, and therefore the analysis period for WY 2011 stops on 30 Sept 2011 (the end of WY 2011).

The streamflow results for WY 2009 are examined first because this year is typical in terms of snow and flow accuracy for both the TI and RTI models. Figure 16 shows the observed and simulated hydrographs, rainfall hyetograph, and the basin average SWE. Overall, the RTI models (RTI Point and RTI Spatial) better capture the timing and magnitude of the observed hydrograph. The TI models underestimate flow in the early spring, possibly because the TI models do not account for $R_{SW,net}$ which can cause snow to melt even when T_a<0°C (T_{rad} can be greater than T_a due to higher values of $R_{SW,net}$). The streamflow in March and April are overestimated by both RTI models, which could occur due to excessive melt on the south-facing slopes of the basin. The overestimation of flow could also result from neglecting infiltration in the basin during snowmelt runoff. The ground at the lower elevations may not be fully saturated in the early spring months. During the main runoff period (May through August) the RTI models perform better than the TI models. The TI models follow the observed hydrograph through June and then overestimate the streamflow in the latter part of the summer. The overestimation of flow is caused by a large and sudden reduction in the basin average SWE during July and August. These are some of the warmest months at SBB, and the reliance on T_a within the TI method may result in excessive melt. The RTI model produces a more gradual reduction in basin average SWE, which results in a more accurate hydrograph. Also, a substantial amount of cloud cover data were missing for WY 2009 (and estimated as described earlier), yet both RTI models still outperform the TI models. Using SCA to calibrate the TI or RTI snow models result in minor differences in streamflow simulation when compared to models calibrated to SWE data. The TI Spatial and TI Point streamflow simulations have similar hydrographs (peak flows and timing). The RTI Spatial and RTI Point streamflow simulations have similar timing, but the RTI Spatial model most accurately represents the hydrograph.

Figure 17 shows scatterplots of the observed and simulated flow as well as graphs of cumulative flow for WY 2009. The scatterplots (left side of Figure 17) show that the RTI Spatial model is the most accurate with most points occurring near the 1-to-1 line. The large overestimation of flow rates in the TI models result in more scatter away from the 1-to-1 line. The cumulative flow graphs (right side of Figure 17) are normalized to the total cumulative observed flow. The RTI Spatial cumulative flow again follows the 1-to-1 line after an initial overestimation of flow in the early spring. Both the TI Point and TI Spatial underestimate the flow in the early spring and greatly overestimate the flow in the late spring and summer.

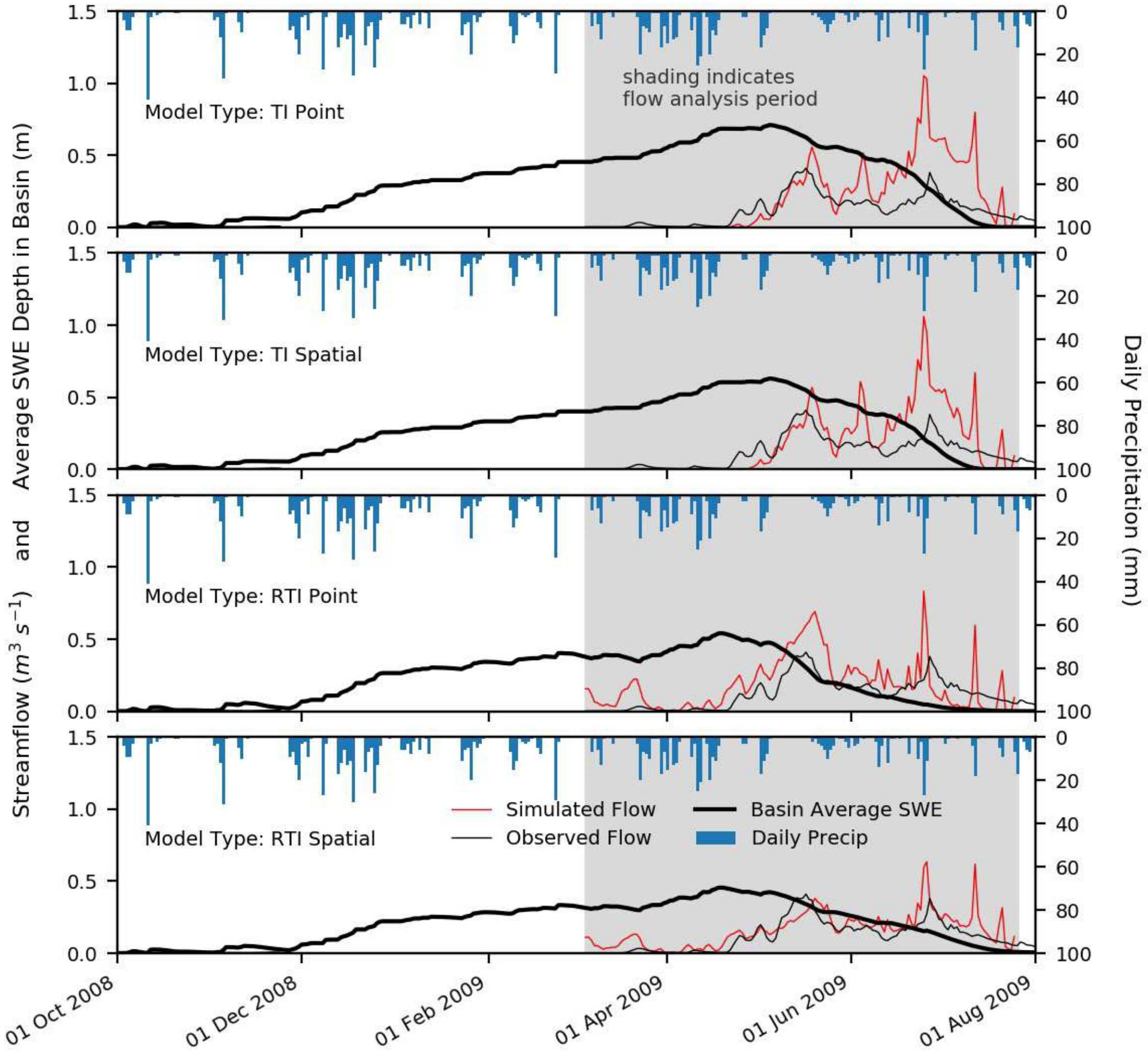

Figure 16. Observed and simulated (TI Point, TI Spatial, RTI Point, and RTI Spatial) hydrographs, rainfall hyetograph, and the basin average SWE for WY 2009.

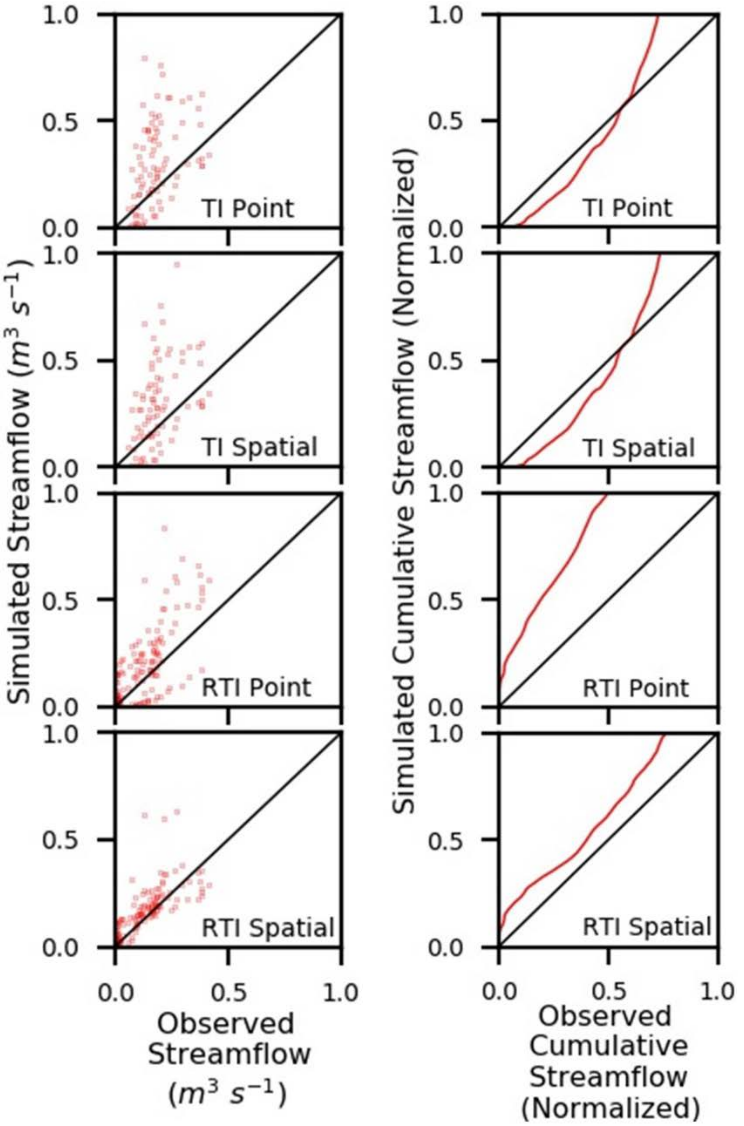

Figure 17. Scatterplot (left) and cumulative 1-to-1 plot (right, normalized to maximum cumulative observed flow) of the observed and simulated flow (TI Point, TI Spatial, RTI Point, and RTI Spatial) hydrographs during the analysis period for WY 2009. In both plots, results closer to the 1-to-1 axis and a slope closer to 1:1 are more accurate.

Figure 18 displays the observed and simulated flow at the outlet of SBB for the entire model period. Overall, the shape, timing, and magnitudes of the RTI Point and RTI Spatial hydrographs match the observed hydrograph better than the hydrographs from the TI Point and TI Spatial hydrographs. The TI Point and TI Spatial hydrographs are similar, with some differences in the magnitude of peak flow each

WY. The RTI Spatial and RTI Point hydrographs have similar timing, but the RTI Spatial most accurately represents the observations in both timing and magnitude of streamflow.

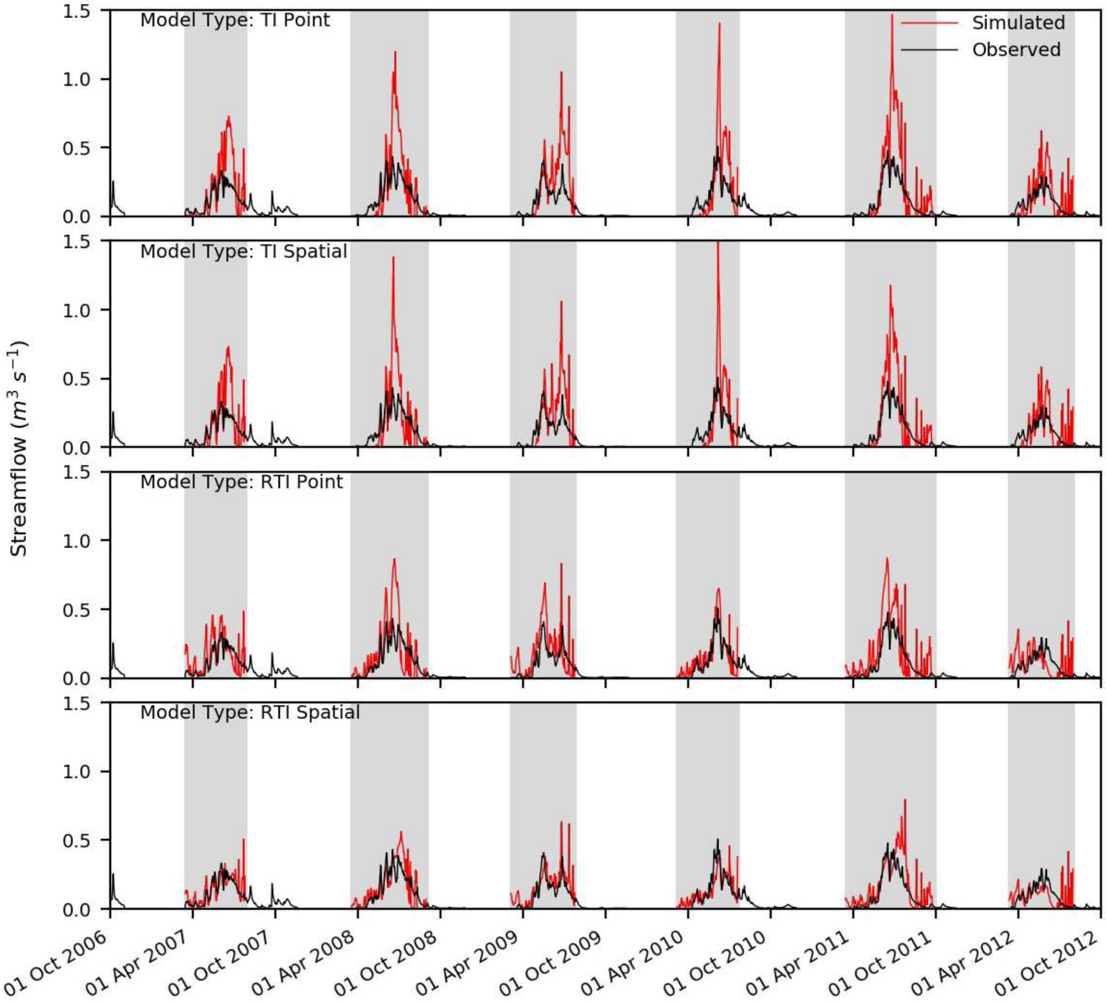

Figure 18. Observed and simulated (TI Point, TI Spatial, RTI Point, and RTI Spatial) streamflow at the SBB outlet for entire model period. Gray shading indicates flow analysis period.

Table 6 shows the observed and simulated flow volume and peak flow rate during the analysis period for each WY. The RTI models (RTI Point and RTI Spatial) better capture the peak flow rate in each WY. The TI models (TI Point and TI Spatial) estimate peak discharges that are more than double the observed peak discharge in each WY. Runoff volume is also better captured when using the RTI models. RTI

Spatial captures the runoff volume the best in every WY, and nearly matches the volume in WY 2010 and WY 2012.

Table 6. Observed and simulated (TI Point, TI Spatial, RTI Point, and RTI Spatial) flow volume and peak flow rate for each WY during the analysis period.

WY		Observed	TI Point	TI Spatial	RTI Point	RTI Spatial
2007	Volume (ha m)	148	224	200	190	163
	Peak Flow (m^3 s^{-1})	0.33	0.73	0.73	0.49	0.51
2008	Volume (ha m)	200	270	240	270	227
	Peak Flow (m^3 s^{-1})	0.43	1.20	1.38	0.87	0.56
2009	Volume (ha m)	147	248	220	230	196
	Peak Flow (m^3 s^{-1})	0.41	1.05	1.06	0.83	0.64
2010	Volume (ha m)	154	211	189	189	154
	Peak Flow (m^3 s^{-1})	0.51	1.40	1.69	0.65	0.46
2011	Volume (ha m)	199	335	297	322	274
	Peak Flow (m^3 s^{-1})	0.48	1.47	1.18	0.87	0.80
2012	Volume (ha m)	121	167	148	142	119
	Peak Flow (m^3 s^{-1})	0.29	0.62	0.58	0.42	0.42
	Overall Volume(ha m)	969	1456	1294	1342	1133

Table 7 shows the RMSE and Nash Sutcliffe Efficiency (NSE) for the observed and simulated flow rates during the analysis period for each WY during the calibration period, validation period, and overall. Based on these statistics, the RTI model more accurately simulates daily streamflow (volume, peak flow, RMSE, and NSE) than the TI model. The TI Spatial and RTI Spatial models have the same SCA Accuracy in WY 2010 and TI Spatial has a higher accuracy in WY 2011, yet the RTI Spatial performs better in flow simulation (volume, peak flow, RMSE, and NSE) in both WY 2010 and WY 2011. These results indicate that even when the RTI and TI models perform similarly in snow simulation (point SWE measurements and/or SCA), the RTI model still performs better in flow simulation. Improved streamflow simulations when using the RTI model may be attributed to better spatial representation of SWE within the basin and better spatial estimates of melting. The models calibrated to SCA more accurately simulate daily streamflow (volume, peak flow, RMSE, and NSE) than models calibrated to SWE. The models calibrated to point SWE sites overestimate the volume of runoff considerably more than the counterparts calibrated to SCA images, likely due to higher calibrated S_{cf} values in both TI Point and RTI Point. Although the analysis periods were chosen to focus on snowmelt-derived runoff, rainfall-derived runoff does affect the watershed throughout the summer months and likely increases the errors.

Table 7. Statistics for simulated (TI Point, TI Spatial, RTI Point, and RTI Spatial) flow rates for each WY, the calibration period (1 July 2006-30 September 2009), the validation period (1 October 2009-30 September 2012), and the entire modeling period. Root mean squared error (RMSE) values closer to zero and Nash-Sutcliffe (NSE) values closer to one indicate better fit.

	WY		TI Point	TI Spatial	RTI Point	RTI Spatial
Calibration Period	2007	RMSE (m^3 s^{-1})	0.17	0.16	0.11	0.07
		NSE	-2.44	-2.02	-0.36	0.42
	2008	RMSE(m^3 s^{-1})	0.21	0.21	0.17	0.09
		NSE	-1.96	-1.91	-1.05	0.41
	2009	RMSE (m^3 s^{-1})	0.19	0.17	0.14	0.09
		NSE	-2.36	-1.67	-0.78	0.29
Validation Period	2010	RMSE (m^3 s^{-1})	0.20	0.20	0.09	0.07
		NSE	-1.56	-1.56	0.54	0.65
	2011	RMSE (m^3 s^{-1})	0.21	0.19	0.15	0.11
		NSE	-1.52	-0.94	-0.31	0.32
	2012	RMSE (m^3 s^{-1})	0.12	0.11	0.11	0.09
		NSE	-1.32	-1.08	-1.21	-0.36
		Calibration Period RMSE (m^3 s^{-1})	0.19	0.18	0.15	0.09
		Calibration Period NSE	-2.17	-1.85	-0.80	0.38
		Validation Period RMSE (m^3 s^{-1})	0.19	0.17	0.13	0.10
		Validation Period NSE	-1.48	-1.14	-0.13	0.35
		Overall RMSE (m^3 s^{-1})	0.19	0.18	0.14	0.09
		Overall NSE	-1.77	-1.44	-0.42	0.37

3.6 Conclusions

The main purpose of this paper was to compare streamflow estimates using a standard temperature-index (TI) and a modified-TI (RTI) snow method within a processed-based hydrologic model to determine if use of the RTI snow method leads to improved streamflow simulation. The secondary purpose was to determine how the TI and RTI methods perform (SWE, SCA, and streamflow) when they are calibrated to either point SWE measurements (the TI Point and RTI Point cases) or basin-wide SCA maps (the TI Spatial and RTI Spatial cases). The primary conclusions of the paper are as follows:

1.) The TI and RTI methods perform similarly in reproducing observed snowpack at Senator Beck Basin (SBB) in Colorado. SWE simulation differences between the TI and RTI models at the two observation locations (SBSP and SASP) are small because both sites are located in areas with little slope and minimal vegetation cover (two characteristics that cause the proxy temperature within the RTI method to deviate from the air temperature, thus causing different snow estimates). Although limited, the RTI model more accurately captures the presence of snow (i.e. SCA) when compared to the TI model.
2.) Calibrating the snow models to SWE sites or SCA images produces minor differences in snowpack simulation, with the main difference being the models calibrated to SCA often simulate lower SWE estimates. The RTI model does show minor improvement in SCA estimation when calibrated to SCA images, while the TI model produces similar SCA estimates regardless of whether calibrated to SWE or SCA.
3.) Use of the RTI method results in more accurate streamflow simulations at the basin outlet (volume, peak flow, RMSE, and NSE) in every water year under all criteria considered. This indicates that the RTI model is likely representing the distribution of SWE and the spatial melt patterns within the watershed better than the TI method.
4.) The models calibrated to SCA maps (RTI Spatial and TI Spatial) are overall more accurate in streamflow simulation (volume, peak flow, RMSE, and NSE) than the corresponding models calibrated to SWE point sites (TI Point and RTI Point). Amounts of SWE within a basin can vary considerably, even over the distance of a few meters (Webb, 2017). Therefore, calibrating to a few point measurements may not result in the watershed model accurately capturing the amount of SWE within a basin.

The scope of this research was limited to a small mountain watershed with high relief, opening several pathways for future research. Differences in streamflow estimation between the TI and RTI models may not be as evident in larger basins where the attenuation of runoff and streamflow along longer drainage pathways can smooth the deviations (Rango and Martinec, 1995). Future research should assess the differences in outflow estimation between the TI and RTI models for larger snow-dominated basins. Within larger basins a calibration routine utilizing both SCA images and SWE measurements may be a preferred method for simulating both the snowpack and streamflow. Many mountain watersheds, including SBB, are known to be impacted by dust events that alter the surface albedo of the snow and may have a primary role in snowmelt and the subsequent snowmelt runoff (Skiles et al., 2015; Painter et al., 2018). Adjustment of the albedo calculation within the RTI model could be a simple approach to simulate the affects of dust on the snowpack and runoff without requiring an energy balance snow model.

CHAPTER 4. A SIMPLE TEMPERATURE-BASED METHOD TO ESTIMATE HETEROGENEOUS FROZEN GROUND WITHIN A DISTRIBUTED WATERSHED MODEL

4.1 Introduction

Frozen ground (also known as frozen soil or soil frost) is important to predicting stormflows produced by certain watersheds (Shanley and Chalmers, 1999; McNamara et al., 1997; Prèvost et al., 1990; Woo, 1986). Several plot-scale studies have shown that frozen ground can impede infiltration and thus enhance runoff (Bayard et al., 2005; Dunne and Black, 1971; Stähli et al., 1999). Several of these studies have also shown that frozen ground is highly-variable temporally and spatially (Campbell et al., 2010; Shanley and Chalmers, 1999; Stähli, 2017), which affects the amount and type of runoff (Wilcox et al., 1997). The presence, spatial pattern, and depth of frozen ground are driven by mass (water) and energy balances. The energy available from the atmosphere to thaw the soil is subject to the insulation of the snowpack (Pearson, 1920; Willis et al., 1961) and ground cover including any vegetation, woody debris, and leaf litter (Brown, 1966; Diebold, 1938; Fahey and Lang, 1975; Sartz, 1973; Stähli, 2017). MacKinney (1929) found that ground cover reduced the depth of frost penetration by 40% at a test site in Connecticut. Additionally, the presence and depth of frozen ground is affected by soil moisture (Fox, 1992; Willis et al., 1961) and the thermal conductivity of the soil (Farouki, 1981; Johansen, 1977).

Frozen ground has proven difficult to simulate within hydrologic models due to complex interactions of energy and water between the atmosphere, snowpack, and soil (Dun et al., 2010; Kennedy and Sharratt, 1998; Lin and McCool, 2006). Physically-based models of frozen ground, such as the Simultaneous Heat and Water (SHAW) model (Flerchinger and Saxton, 1989), the coupled heat and mass transfer model for soil-plant-atmosphere systems (COUP) (Jansson 2001; Jansson and Karlburg, 2010), and the Distributed Water-Heat Coupled (DWHC) model (Chen et al., 2007) have large parameter and forcing data requirements – such as wind speed, relative humidity, and short- and long-wave radiation – which restricts their applicability in many watershed. Additionally, these types of models either include, or are tightly coupled to soil moisture models, which can limit their applicability in models that do not explicitly simulate soil moisture content. To reduce data and parameter requirements and increase applicability, simple temperature-index or degree-day methods (Molnau and Bissell, 1983; Rekolainen and Posch, 1993) remain widely used within watershed models, including LISFLOOD (De Roo et al., 2001; Van Der Knijff et al., 2010), CREAMS (Rekolainen and Posch, 1993), and the Gridded Surface Subsurface Hydrologic Analysis (GSSHA) model (Downer and Ogden, 2004). Degree-day approaches typically accumulate the daily average temperature as a frost index (°C-days). When the frost index exceeds a threshold, the soil is considered frozen and impermeable to infiltration. The sudden restriction on infiltration can be an incorrect assumption, especially in forested environments where frozen soils often still experience infiltration (Lindstrom et al. 2002; Nyberg et al., 2001; Shanley and Chalmers, 1999). A limitation of degree-day approaches is that they are often untested against observed frost data because the frost index is not a physical property that can be compared to measurements. However, degree-day methods have been successful in capturing increased runoff from frozen ground events (Molnau and Bissell, 1983), and higher frost index values have been shown to correlate to deeper frost depths (Vermette and Christopher, 2008; Vermette and Kanack, 2012). Spatial variations of frozen ground within degree-day methods are typically based on variations in temperature (which are estimated from an elevation-temperature relationship) and variations in snowpack insulation (which are also typically inferred from an elevation-temperature relationship). Such reliance on elevation may lead to errors because Stähli (2017) found no clear connection between elevation and presence of frozen ground at test sites in the Swiss pre-alpine zone.

The objective of this paper is to develop a model for frozen ground that (1) captures the spatial variations of frozen ground within a watershed, (2) allows the frozen ground model to be incorporated into a variety of watershed models, and (3) allows application in data sparse environments where limited forcing data may prohibit use of energy balance methods. In this paper, we use the GSSHA watershed model and develop the frozen ground model by modifying the commonly used Conceptual Frozen Ground Index (CFGI) (Molnau and Bissell, 1983) method in four ways. First, the CFGI method is coupled to an improved snowpack model that more accurately captures the spatial heterogeneity of the snowpack. In past applications of GSSHA, the CFGI method has been coupled with a temperature-index (TI) snowpack model based on SNOW-17 (Anderson, 1973; Anderson, 2006). However, Follum et al. (2015) proposed a Radiation-derived Temperature Index (RTI) snow model that uses a proxy temperature instead of air temperature to represent the energy available to the snowpack. Compared to the TI model, the RTI model more directly includes the effects of shortwave radiation and canopy cover and was shown to better represent the spatial variations of snow cover and snow water equivalent (SWE) in the Senator Beck Basin in Colorado. The RTI model is adopted to simulate the snowpack in the present study. Second, the effects of shortwave radiation and canopy cover are included in the CFGI model when calculating the energy available at the snow or ground surface. These effects are included by using a similar radiation-derived proxy temperature when calculating the frost index. Third, the insulation effects of ground cover are included by modifying the frost index equation. Fourth, an option is included to compute frost depth as a function of the frost index value. The modified Berggren Equation and similar Stefan Equation have been previously used to estimate frost depth from degree-days (Carey and Woo, 2005; DeWalle and Rango, 2008; Fox, 1992; Woo et al., 2004); a similar approach is used here to convert the frost index to frost depth.

The following sections first describe the existing TI and CFGI models within GSSHA. The combination of these two models serves as the baseline or control case for the experiments. Then, the RTI snow model and the modified CFGI frozen ground model (referred to as modCFGI) are described. Finally, the results of the TI/CFGI model and RTI/modCFGI models are compared to each other and to observations of snow depth, SWE, and frost depth at the Sleepers River Experimental Watershed (SREW) in Vermont.

4.2 Methodology

4.2.1 TI Snowpack Model

The TI snow model was implemented into GSSHA by Follum et al. (2014), who provides additional information about the model. Although GSSHA allows a variable time step for multiple processes, it always uses an hourly time step (Δt) for snow calculations. GSSHA utilizes a structured grid in which each cell can have a different air temperature T_a ($°C$) and precipitation P (m h^{-1}). Air temperature is the primary driver of snowpack dynamics in the TI model and is estimated as:

$$T_a = T_g + \emptyset\left(E_g - E_c\right), \tag{34}$$

where T_g (°C) is the air temperature at a gage, $\emptyset$ is a linear lapse rate (°C km^{-1}), and E_g and E_c (m) are the elevations of the temperature gage and the grid cell where T_a is being calculated, respectively. Precipitation accumulates as SWE (m) when $T_a \leq T_{px}$, where T_{px} is the freezing point (0°C by default). The precipitation P is multiplied by a uniform multiplication factor (S_{cf}), which crudely represents snowpack sublimation and redistribution of snow due to wind (Anderson, 2006). The resultant effective precipitation (P_{eff}) is added to the SWE.

Before the snowpack begins to melt, its heat deficit (or cold content) must be overcome. The change in heat deficit ΔD_t (mm of SWE), due to a temperature difference between the snow surface and air, is calculated as:

$$\Delta D_t = N_{mf,\max}(\Delta t/6)\left(M_f/M_{f,\max}\right)(A_{TI} - T_{sur}), \tag{35}$$

where T_{sur} is the snow surface temperature, and A_{TI} is the antecedent temperature index (°C), which is calculated using T_a and the antecedent snow temperature index parameter A_{TIPM} (see Anderson (2006) for details regarding T_{sur} and A_{TI}). $N_{mf,\max}$ is the maximum negative melt factor (mm °C^{-1} (6 h)$^{-1}$), which is a parameter. M_f is the melt factor (mm °C^{-1} Δt^{-1}), which is calculated as:

$$M_f = (\Delta t/6)\left[S_v A_v\left(M_{f,\max} - M_{f,\min}\right) + M_{f,\min}\right], \tag{36}$$

where S_v and A_v are seasonal melt adjustments that change by Julian day, and $M_{f,\max}$ and $M_{f,\min}$ are the maximum and minimum melt factors (mm °C^{-1} (6 h)$^{-1}$), which are parameters.

Once the heat deficit is overcome, SWE decreases as melt occurs. During normal conditions, the melt M (mm of SWE) is:

$$M = \left[M_f(T_a - T_{mbase}) + 0.0125P_{eff}f_rT_r\right]\Delta t, \tag{37}$$

where T_{mbase} is the temperature at which melt begins (0°C by default), f_r is the fraction of any precipitation that is rain (assumed equal to 1 when $T_a > 0°C$, otherwise set to 0), and T_r is the precipitation temperature (assumed equal to T_a or 0°C, whichever is greater). During rain-on-snow events (more than 1.5 mm of rainfall in the previous 6 h), M is calculated from a simple energy balance:

$$M = \sigma\left[(T_a + 273)^4 - 273^4\right]\Delta t + 0.0125P_{eff}f_rT_r + 8.5f_u(\Delta t/6)[(r_he_{sat} - 6.11) + 0.00057P_aT_a], \tag{38}$$

where σ is the Stefan-Boltzmann constant, f_u is the average wind function (mm mb^{-1} (6 h)$^{-1}$) (see Anderson (2006) for details), r_h is the relative humidity (assumed to be 0.9 during rain-on-snow events) (Anderson, 1973, 2006), P_a is atmospheric pressure (mb) (either measured or calculated from elevation) (Anderson, 2006), and e_{sat} is the saturation vapor pressure (mb) (calculated based on Smith (1993)). The ripeness of the snowpack affects the amount of melt that is released and is controlled by the liquid holding capacity L_{hc}, which is a specified percentage of the ice in the snowpack (Anderson, 2006).

For frozen ground calculations, the snow depth is needed from the snow model. The snow depth D_s (cm) is found from the SWE and the snowpack density. GSSHA uses the single-layer snow density functions from SNOW-17 (Anderson, 1976; Anderson, 2006). The density of newly fallen snow ρ_n (gm cm^{-3}) varies between 0.05 ($T_a \leq -15°C$) and 0.15 ($T_a = 0°C$) according to:

$$\rho_n = 0.05 + 0.0017\,(T_a + 15)^{1.5}. \tag{39}$$

Increases in snowpack density ρ_x from compaction, destructive metamorphism, and melt metamorphism due to the presence of liquid water are calculated as (Koren et al., 1999):

$$\rho_{x,t} = \rho_{x,t-1} \left(\frac{e^{B_2}}{B_2}\right) e^{B_1}, \tag{40}$$

where:

$$B_1 = c_3\, c_5\, dt\, e^{c_4\, T_s - c_x\, \beta\, (\rho_{x,t-1} - \rho_d)}, \text{ and} \tag{41}$$

$$B_2 = W_{i,t-1}\, c_1\, dt\, e^{0.08\, T_s - c_2 \rho_{x,t-1}}. \tag{42}$$

The variable t is an index for time, W_i is the ice portion of the snow pack (cm, $W_i = 100\, S_{swe,t-1}$) where S_{swe} is the snow water equivalent on the ground in m, T_s is the average snow pack temperature (°C, calculated based on Anderson (2006)), and ρ_d is the threshold density above which destructive metamorphism decreases (ρ_d is set to 0.15 gm cm^{-3} based on Anderson (2006)). Finally, $\beta = 0$ if $\rho_{x,t-1} \leq \rho_d$, and $\beta = 1$ if $\rho_{x,t-1} > \rho_d$, $c_1 = 0.026$ cm^{-1} hr^{-1}, $c_2 = 21$ cm^{3} gm^{-1}, $c_3 = 0.005$ hr^{-1}, $c_4 = 0.10$ °C^{-1}, and $c_5 = 2.0$ if there is liquid water in the snowpack and $c_5 = 1.0$ if there is not (see Anderson (1976) and Anderson (2006) for details).

4.2.2 CFGI Frozen Ground Model

The CFGI model was originally developed as a lumped model for flood forecasting in the Pacific Northwest, but it has been used in distributed models as well (De Roo et al., 2001; Van Der Knijff et al., 2010). The rationale of the CFGI method is that air temperature ultimately controls the ground temperature, but its impact is moderated by the insulating effects of any snowpack. The presence of frozen ground is determined by the frozen ground index F (°C-days), which is calculated as:

$$F_t = F_{t-1} A - T_{a,d}\, e^{-0.4 K_s D_s}, \tag{43}$$

where $T_{a,d}$ is the average daily air temperature (°C), A is a daily decay coefficient, and K_s is the snow reduction coefficient (cm^{-1}). A controls the persistence of the F values, and K_s controls the insulation from the snowpack. Molnau and Bissell (1983) recommended changing K_s depending on whether $T_{a,d}$ is above or below freezing (denoted as $K_{s,T_a>0°C}$ and $K_{s,T_a<0°C}$, respectively).

Higher values of F indicate a higher likelihood that the ground is frozen. Once F exceeds a specified threshold ($F_{threshold}$), the ground is considered frozen and infiltration is restricted. Molnau and Bissell (1983) found the ground to be frozen when $F > 83$ °C-days and thawed when $F < 56$ °C-days. When F is between these values, the ground could be either frozen or thawed. It is worth noting that F does not depend on soil moisture, which is known to affect the initialization and depth of frozen ground (Kurganova et al., 2007; Willis et al., 1961).

4.2.3 RTI Snowpack Model

The RTI model makes two modifications to the TI model: (1) it uses a radiation-derived temperature T_{rad} $(°C)$ to better describe the available energy, and (2) it estimates spatially-varying snowpack sublimation based on solar radiation approximations.

The RTI model replaces T_a in Eq. (37) and (38) with a radiation-derived proxy temperature T_{rad} (°C). In those equations, T_a is used to conceptually represent the energy available to the snowpack. T_{rad} has a similar purpose but is intended to improve the estimation of available energy. T_{rad} is calculated by assuming that the radiation terms dominate the energy balance at the snow surface so that outgoing longwave radiation balances the net incoming shortwave and longwave radiation (Follum et al., 2015). Thus:

$$R_{LW\uparrow} = R_{SW,net} + R_{LW\downarrow}, \tag{44}$$

where $R_{LW\uparrow}$ is outgoing longwave radiation, $R_{SW,net}$ is the net incoming shortwave radiation, and $R_{LW\downarrow}$ is the downwelling longwave radiation. The right side of Eq. (44) represents the energy that is supplied to the snowpack via the atmosphere. $R_{LW\uparrow}$ (W m^{-2}) is the radiative response of the snowpack to that energy. Using the Stefan-Boltzmann Law, $R_{LW\uparrow}$ can be written in terms of a temperature T_{rad}:

$$T_{rad} = \left(\frac{R_{SW,net}+R_{LW\downarrow}}{\varepsilon_{snow}\,\sigma}\right)^{1/4} - 273.15, \tag{45}$$

where ε_{snow} is the emissivity of snow (assumed to be 0.97) and σ is the Stefan-Boltzmann constant. $R_{SW,net}$ is calculated:

$$R_{\mathrm{SW,net}} = (1 - \alpha_s) R_{\mathrm{SW}\downarrow}, \tag{46}$$

where α_s is the albedo of the snowpack, which is calculated based on the time elapsed since the most recent snowfall and whether melt is occurring (Henneman and Stefan, 1999). $R_{\mathrm{SW}\downarrow}$ is the incident shortwave radiation, which is calculated:

$$R_{\mathrm{SW}\downarrow} = R_{\mathrm{SW,0}}\, \varphi_r\, \varphi_{atm}\, \varphi_c\, \varphi_v\, \varphi_s\, \varphi_t, \tag{47}$$

where $R_{SW,0}$ is the solar constant (Liou, 2002), φ_r accounts for distance from the Earth to the sun (based on Julian day (TVA, 1972)), φ_{atm} accounts for atmospheric scattering (based on elevation (Allen et al., 2005)), φ_c accounts for absorption by clouds (based on fractional cloud cover (TVA, 1972)), φ_v accounts for vegetation (set equal to the vegetation transmission coefficient K_v (Bras, 1990), a vegetation-specific parameter ranging from 1.0 for no canopy coverage to 0.0 for complete canopy coverage), φ_s accounts for the slope/aspect of the terrain (based on latitude, slope, and azimuth angle (Duffie and Beckman, 1980)), and φ_t accounts for topographic shading (based on elevation, azimuth angle, and solar elevation angle).

$R_{LW\downarrow}$ is calculated from the contributions of the atmosphere (including clouds) and the canopy:

$$R_{LW\downarrow} = \sigma \varepsilon_a (T_a + 273.15)^4 (1.0 + 0.17\, N^2)(1 - F_c) + F_c \sigma \varepsilon_c \left(T_{canopy} + 273.15\right)^4, \tag{48}$$

where ε_a is the air emissivity (0.757 when snow is present based on Bras (1990)), N is the fractional cloud cover, F_c is the fractional canopy cover (estimated from leaf area index L_{AI} following (Liston and Elder, 2006; Pomeroy et al., 2002)), ε_c is the canopy emissivity (assumed equal to 1 following Sicart et al. (2004)), and T_{canopy} is the canopy temperature (°C) which is assumed equal to T_a following DeWalle and Rango (2008).

Because the TI model uses T_a to drive snowpack dynamics, those dynamics are only directly associated with the downwelling longwave radiation from the air, which is a component of $R_{LW\downarrow}$. Furthermore, the spatial variations in the available energy depend only on the variations of T_a, which are inferred from elevation. T_{rad} in the RTI model considers both $R_{SW,net}$ and $R_{LW\downarrow}$ and thus accounts for heterogeneity in topographic orientation and shading as well as canopy cover. The TI model partially accounts for seasonal variation in solar radiation and snow albedo by empirically adjusting M_f as shown in Eq. (36). In the RTI model, seasonal variations in solar radiation and snow albedo are included in T_{rad}, so a constant melt factor M_f is used (Follum et al., 2015).

The TI model uses a uniform multiplication factor (S_{cf}) that is applied to the precipitation to account for sublimation, but sublimation is known to vary spatially (Musselman, 2008; Rinehart, 2008; Veatch, 2009). Most sublimation methods depend on relative humidity and wind speed (e.g. Pomeroy, 1988; Liston and Elder, 2006), which are often unavailable in data sparse environments. However, Gustafson et al. (2010) linked differences in sublimation rates to the amount of solar radiation a location receives. In the RTI model a simple approach is used to estimate hourly sublimation rates S_{sub}(cm hr^{-1}) as:

$$S_{sub} = S_{sub,d}\left(\frac{R_{SW\downarrow}}{R_{SW\downarrow,flat}}\right), \tag{49}$$

where $S_{sub,d}$ (cm d^{-1}) is the watershed-average daily maximum sublimation amount (a parameter), and $R_{SW\downarrow,flat}$ is the daily shortwave radiation for a flat cell within the watershed on a cloud-free day. Thus, locations with higher $R_{SW\downarrow}$ (e.g., open areas and south-facing slopes in the northern hemisphere) will have higher values of S_{sub}. The method neglects wind speed and relative humidity, but does vary sublimation rates based on spatial patterns of solar radiation.

4.2.4 modCFGI Frozen Ground Model

The CFGI model is modified in three ways to create the modCFGI model. First, the average daily proxy temperature $T_{rad,d}$ is used in place of $T_{a,d}$ to represent available energy. Second, ground cover (leaf litter, woody debris, etc.) is included as an insulator in the frozen ground index. And third, an option is included to estimate frost depth based on the frozen ground index. The frost depth calculation is optional because it requires soil moisture estimates and may not be needed in many hydrologic models that only require the occurrence (not depth) of frozen ground.

The CFGI uses $T_{a,d}$ in Eq. (43) to represent the energy that is available to heat the ground surface. In the modCFGI model, $T_{a,d}$ is replaced with $T_{rad,d}$. $T_{rad,d}$ is calculated using α_s (see Eq. (45) and (46)) when snow is present, and the albedo of the land cover when snow is not present. By using $T_{rad,d}$, the modCFGI model is expected to better represent the spatial heterogeneity of energy supply due to variations in the topography and canopy cover within a watershed.

The insulation by the ground cover is included by modifying Eq. (43) to become:

$$F_t = F_{t-1}A - T_{rad}\, e^{-0.4\left(K_s D_s + K_{gc} D_{gc}\right)}, \qquad (50)$$

where K_{gc} is the ground cover reduction coefficient (cm^{-1}) and D_{gc} is the depth of ground cover (cm). This formulation retains the original form of the CFGI model but includes insulation from both snowpack and ground cover. F can still be used to identify the occurrence of frozen ground, which may be sufficient for many hydrologic models. However, because F is not a measurable quantity, an option to extend modCFGI to calculate frost depth is also needed.

Frost depth is calculated using F and the modified Berggren Equation. As originally proposed (and described by DeWalle and Rango (2008)), the Berggren equation relates the number of degree days in the freezing/thawing period U (ºC-days) to the maximum frost depth $Z_{\max}$ (m) as follows:

$$Z_{\max} = \lambda(48\, U\, \delta^{-1} \Omega_m)^{1/2}, \qquad (51)$$

where λ is a dimensionless coefficient that accounts for changes in sensible heat of the soil, δ (J m^{-3}) is the latent heat of fusion of the soil, and Ω_m (J m^{-1} h^{-1} °C^{-1}) is the mean thermal conductivity of the frozen and unfrozen soil layers. The derivation and corresponding assumptions (i.e. linear soil temperature gradients (Aldrich, 1956)) do not reveal any major impediments to adapting this equation for a shorter time step. In addition, Fox (1992), Woo et al. (2004), and Carey and Woo (2005) have used a layered version of the Stefan Equation, which is similar to Eq. (51) to simulate daily frost depths with daily input data. Thus, the modified Berggren Equation is applied at a daily time scale and revised to become:

$$Z_d = \lambda[48\,(F - F_{threshold})\,\delta^{-1}\Omega_m]^{1/2}, \tag{52}$$

where Z_d is the depth of frozen ground (m). By using the difference between F and $F_{threshold}$, the degree-days of the current freezing/thawing period is utilized, which is similar to the use of U in the original equation. Z_d is only calculated once the ground begins to freeze (when $F > F_{threshold}$). Z_d deepens as F becomes increasingly larger than $F_{threshold}$. When F decreases (due to increasing T_{rad}), so does the thickness of frost depth. No frost remains when F falls below $F_{threshold}$.

For the original modified Berggren Equation, λ can be estimated annually from Aldrich (1956) using U, the mean annual air temperature, and the soil water content ω (% of dry weight). Here, λ is calculated using daily differences between F and $F_{threshold}$, the mean annual air temperature, and daily ω values. Thus, soil moisture is included in the calculation of Z_d even though it is not included in the calculation of F. Furthermore, δ is estimated daily as:

$$\delta = \delta_f \rho\, \omega/100, \tag{53}$$

where δ_f is the latent heat of fusion of water (0.334 MJ kg^{-1} at 0°C) and ρ is the dry soil density. Ω_m is estimated as (Farouki, 1981; Johansen, 1977):

$$\Omega_m = \left(\Omega_{sat} - \Omega_{dry}\right)\omega + \Omega_{dry}, \tag{54}$$

where Ω_{dry} and Ω_{sat} are the thermal conductivity of dry and saturated soil, respectively. Ω_{sat} is calculated as the geometric mean of the conductivities of the materials within the soil profile (Farouki, 1981; Johansen, 1977):

$$\Omega_{sat} = {\Omega_s}^{(1-n_{total})} {\Omega_{ice}}^{(n_{ice})} {\Omega_{water}}^{(n_{total}-n_{ice})}, \tag{55}$$

where Ω_s, Ω_{ice}, and Ω_{water} are the thermal conductivity of solids, ice, and water, respectively (Farouki, 1981). n_{total} is the porosity, and n_{ice} is:

$$n_{ice} = n_{total}\, Z_d / H, \tag{56}$$

where H (m) is the soil thickness.

4.3 Model Application

4.3.1 Study Area

The TI/CFGI and RTI/modCFGI models are tested at the W-3 sub-basin (Figure 19) of the SREW. The study period is 1 Oct 2005 through 30 Sept 2010, which is water year (WY) 2006 through 2010. The SREW was founded in 1958 primarily for studies of snow accumulation, melt, and runoff (Anderson, 1973; Anderson, 1976; Dunne and Black, 1970a; Dunne and Black, 1970b; Dunne and Black, 1971; Shanley, 2000; Shanley and Chalmers, 1999). The W-3 sub-basin is located at 44° 29' N and 72° 09' W. Elevations range between 348 m and 697 m, and the area is approximately 8.5 km^2 (based on the National Elevation Dataset (Gesch et al., 2002)). The basin is primarily forested with deciduous (57.7%), evergreen (7.8%), and mixed (15.3%) trees (based on the 2006 National Land Cover Database (NLCD) (Fry et al., 2011)). Approximately 14.6% of the land cover is pasture/hay and cultivated crops. These open areas are typically below an elevation of 525 m, which is the approximate limit for viable agriculture (Shanley and Chalmers, 1999). The W-3 sub-basin is extensively gaged for both hydrometeorology and hydrology by the U.S. Geological Survey (USGS) and collaborators from federal agencies and universities. Additional basin information and data are provided by Shanley et al. (1995), Shanley and

Chalmers (1999) and the USGS website (https://nh.water.usgs.gov/project/sleepers/index.htm, accessed 7 November 2016).

Two snow sites and 35 frost sites within W-3 were monitored by the Vermont Field Office of the USGS. At the snow sites, SWE and snow depth were measured approximately weekly, and both sites are used in the present study. At the frost sites, snow depth and frost depth were measured periodically (between 0 and 14 measurements in a given winter). Frost depth was measured using CRREL-Gandahl frost tubes (Ricard et al., 1976), which are filled with a methylene blue solution. The frost depth is identified by a change in colour within the tube (blue indicates thawed, clear indicates frozen). Vermette and Kanack (2012) provide images and descriptions of similar frost tubes, and Shanley and Chalmers (1999) provides detailed descriptions of the frost tubes at SREW. The frost sites (labelled FS in Figure 19) are clustered in six parts of the watershed. For this paper, one site from each cluster (FS4, FS11, FS21, FS24, FS30, and FS40) was selected for analysis. The selected sites are far enough apart to be relatively independent but still capture the variations in elevation and land cover classification within the watershed.

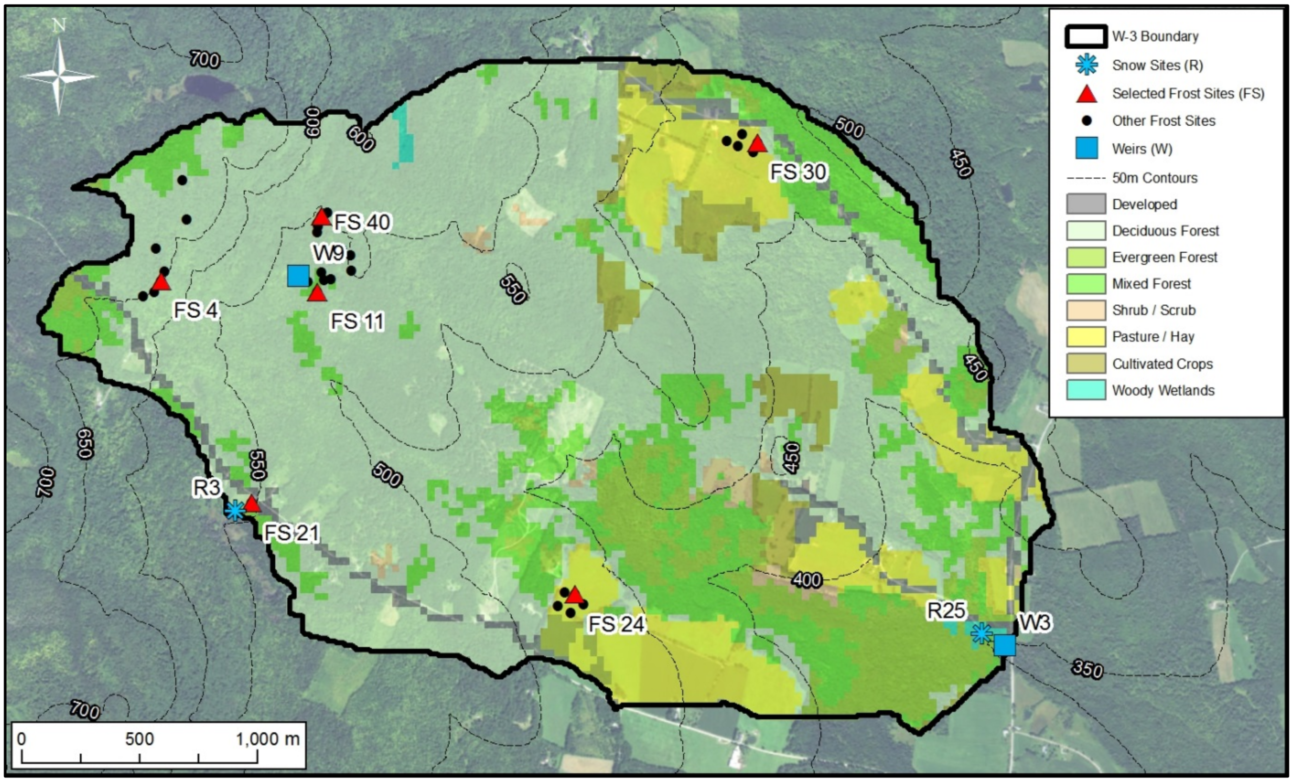

Figure 19. W-3 sub-basin in the Sleepers River Experimental Watershed. Sites used in this study are identified with red triangles and blue snowflakes. Basin delineation and elevation contours (m) are based on the 1/3-arc-second National Elevation Dataset, land cover classification based on the 2006 National Land Cover Database, and sources of the background imagery include ESRI, DigitalGlobe, Earthstar Geographics, CNES/Airbus DS, GeoEye, USDA FSA, USGS, Getmapping, Aerogrid, IGN, IGP, and the GIS User Community.

4.3.2 Model Inputs

The TI and CFGI models require hourly precipitation and temperature data, which were obtained from the USGS. Precipitation was measured at the W9 weir and R3 snow site (Figure 19). The USGS then creates a single spatially-averaged precipitation time series by weighting the measurements using the distribution of elevation (based on personal communication with Dr. James Shanley of the Vermont Field Office of the USGS on 14 November 2016). The W9 gage receives more weight because the watershed includes elevations both above and below this site. Hourly temperature was measured at the W9 site, which has an elevation of 520 m.

The RTI and modCFGI models also require cloud cover data, which were obtained from the National Centers for Environmental Information (NCEI, https://www.ncdc.noaa.gov/, accessed 7 November 2016). The hourly cloud-cover classification data (clear, few clouds, broken sky, etc.) were collected at the Edward F. Knapp State Airport (44 km southwest of the basin) and the Morrisville-Stowe State Airport (36 km west of the basin). The classification data were converted to cloud cover percentages using the method from Follum et al. (2015). Cloud cover data are routinely measured at most airports in the U.S. (data archived at NCEI) as well as many meteorological stations. For simulation of frost depth (and comparison to frost depth observations), soil moisture and evapotranspiration were also simulated. These two components additionally require hourly relative humidity, wind speed, and atmospheric pressure data, all of which were obtained from a meteorological station at the Fairbanks Museum in Saint Johnsbury, VT (11 km southeast of the basin) with missing values filled-in using hourly data from the two airports. All the models require elevation data to determine the spatial patterns of snow and frozen ground. W-3 was delineated using the 1/3-arc-second (~9 m) National Elevation Dataset (Gesch et al., 2002). The RTI and CFGI models additionally require land cover classifications, which were obtained from the 2006 National Land Cover Database (Fry et al., 2011) and have a 30-m resolution. The classifications of some grid cells were changed to match the land covers observed in the field. In particular, the grid cell containing R3 was changed from deciduous forest to pasture/hay, FS11 was changed from mixed forest to evergreen forest, and FS21 was changed from developed to mixed forest. Both FS24 and FS30 are classified as pasture/hay, where FS24 is a managed pasture and FS30 is an unmanaged pasture (personal communication with Ann Chalmers of the Vermont Field Office of the USGS on 15 November 2016). For example, during field observations in November 2016, FS24 had manure spread throughout the field, while FS30 was not fertilized.

Soil classification data are also required if calculating frost depth, which were obtained from the Digital General Soil Map of the Unites States (Soil Survey Staff, Natural Resources Conservation Service, United States Department of Agriculture, Web Soil Survey, available online at http://websoilsurvey.nrcs.usda.gov/. Accessed 10 August 2016). Almost the entire W-3 basin is classified as fine sandy loam. The Watershed Modeling System (Aquaveo, 2013) was used to develop the GSSHA model with a 30-m structured grid. This resolution is adequate to capture the spatial heterogeneity of the basin while remaining computationally efficient.

4.3.3 Parameter Estimation and Calibration

The Model-Independent Parameter Estimation and Uncertainly Analysis (PEST) method (Doherty et al., 1994) was used to calibrate 7 parameters in the TI model and 8 parameters in the RTI model. PEST is a nonlinear local search parameter estimator that calibrates numerous parameters simultaneously to produce the best fit between simulated results and observations. WY 2006 and 2007 were used as the calibration period. The TI and RTI snow models were calibrated first to minimize the sum of the squared residuals between simulated and observed snow depths at the 8 sites (6 frost sites and 2 snow sites).

Table 8 displays the allowable range, calibrated value, and sensitivity ranking for the calibrated snow parameters. Goodness of fit statistics as well as description of affects each parameter has on the snow simulations are described in the Results and Discussion section. The allowable ranges for A_{TIPM}, f_u, L_{hc}, $N_{mf,\max}$, M_f , $M_{f,\max}$, and $M_{f,\min}$ are based on physical limitations and typical ranges in the literature (Follum et al., 2015). L_{AI} can be estimated from seasonal and annual relationships to remotely-sensed normalized difference vegetation index (NDVI) values (Wang et al., 2005). However, snowpack affects the measurement of greenness in high latitude regions (Beck et al., 2006). Thus, L_{AI} and K_v values were calibrated based on land cover classifications with forested land covers being categorized as deciduous forest (including deciduous forest, woody wetlands, and mixed forest) or evergreen forest. L_{AI} and K_v values for non-forested land cover classifications were set to 0.0 and 1.0, respectively. T_{px} and T_{mbase} were not calibrated (both are 0°C) because the temperature data were post-processed by the Vermont USGS and are expected to be accurate. By comparing the temperature measurements at W9 and the

Fairbanks Museum (elevation of ~212.4 m), $\emptyset$ was estimated at 6.6 °C km^{-1}. All snow density parameters are set based on Anderson (1973) and Anderson (2006).

The PEST results indicate that the TI model's snow depths are most sensitive to S_{cf}, $M_{f,\max}$, A_{TIPM}, and $M_{f,\min}$. For the RTI model, snow depths are most sensitive to K_v (deciduous), A_{TIPM}, L_{AI}(evergreen), and M_f (Table 8). The calibrated deciduous K_v is near the top of the allowable range (1.0) and L_{AI} is near the bottom (0.103), indicating that the snow in the deciduous forest behaves similarly to the open pasture areas where K_v=1 and L_{AI}=0.

Table 8. Allowable ranges and calibrated values for the TI and RTI model parameters using PEST. Dashes indicate parameters that are not required in the associated model. The sensitivity ranking for each parameter is shown in parentheses.

		Allowable	Calibrated Values	
Parameter	Units	Range	TI	RTI
$M_{f,\ max}$	mm °C^{-1} (6 h)$^{-1}$	0.001-2.400	1.017 (2)	--
$M_{f,\ min}$	mm °C^{-1} (6 h)$^{-1}$	0.001-1.600	0.001 (4)	--
M_f	mm °C^{-1} (6 h)$^{-1}$	0.001-2.400	--	0.391 (4)
S_{cf}	fraction	0.800-1.000	0.869 (1)	--
$S_{sub,\ d}$	cm d^{-1}	0.001-0.100	--	0.068 (6)
$N_{mf,\ max}$	mm °C^{-1} (6 h)$^{-1}$	0.001-2.400	0.002 (6)	0.256 (8)
f_u	mm mb^{-1} (6 h)$^{-1}$	0.001-1.000	0.500 (7)	0.500 (10)
A_{TIPM}	fraction	0.001-1.000	1.000 (3)	0.992 (2)
L_{hc}	fraction	0.001-0.100	0.001 (5)	0.001 (9)
$K_{v,\ deciduous}$	fraction	0.200-1.000	--	0.969 (1)
$K_{v,\ evergreen}$	fraction	0.200-0.800	--	0.308 (7)
$L_{AI,\ deciduous}$	m^2 m^{-2}	0.100-1.000	--	0.103 (5)
$L_{AI,\ evergreen}$	m^2 m^{-2}	1.000-4.000	--	1.000 (3)

The CFGI and modCFGI frozen ground models were calibrated to minimize the sum of squared residuals between the simulated and observed frost depths at the 6 frost sites. For purposes of comparison the modified Berggren equation was also added to the CFGI model to calculate frost depth. Table 9 displays the allowable range, calibrated value, and sensitivity ranking of each calibrated frozen ground parameter. Goodness of fit statistics as well as description of affects each parameter has on the frost depth simulations are described in the Results and Discussion section. $F_{threshold}$ was calibrated for both the CFGI and modCFGI models with the upper range based on Molnau and Bissell (1983). Three K_{gc} values were calibrated for the modCFGI frozen ground model: one for the managed pasture site FS24 ($K_{gc,FS24}$), one for the unmanaged pasture site FS30 ($K_{gc,FS30}$), and one for all other frozen ground sites (K_{gc}). Following Molnau and Bissell (1983), multiple combinations of A (0.8 and 0.97), and $K_{s,T_a<0°C}$ and $K_{s,T_a>0°C}$ (0.08, 0.2, and 0.5) values were tested with A = 0.97, $K_{s,T_a<0°C}$ = 0.08, and $K_{s,T_a>0°C}$ = 0.5 producing frost indices that best replicate the rise and fall of the frost depth as well as the timing of the peak frost depth. Depth of ground cover for each land cover type was obtained from field observations in November 2016. Specifically, $D_{gc} = 6$ cm for deciduous forest (fallen leaves), $D_{gc} = 2$ cm for evergreen forest (fallen leaves), $D_{gc} = 4$ cm for pasture (grass), and $D_{gc} = 0$ cm for all other land cover types. The modified Berggren Equation requires soil moisture, which can be simulated using several methods in GSSHA (Downer and Ogden, 2006). To facilitate extension of these results to other hydrologic models, the commonly-used single-layer Green and Ampt infiltration model (Green and Ampt, 1911) with soil moisture redistribution between rainfall events (Ogden and Saghafian, 1997) is utilized to calculate infiltration. Soil moisture is tracked using a simple bucket approach, accounting for infiltration, evapotranspiration, and groundwater recharge as described in Downer (2007). The soil layer thickness (H) is set to 0.5 m for both the soil moisture calculations and frost depth equations. Soil infiltration parameters are set based on published values for the W-3 soil type (Downer and Ogden, 2006; Rawls et al., 1982; Rawls and Brakensiek, 1985; Rawls et al., 1983) and are shown in Table 10 Evapotranspiration, which can reduce the soil moisture, is simulated using a Penman Monteith approach (Monteith, 1965; Monteith, 1981) with parameters estimated based on land cover (Downer and Ogden, 2006). The dry soil density (ρ = 1137 kg m^{-3}) and dry soil thermal conductivity (Ω_{dry} = 792 J m^{-1} h^{-1} °C^{-1}) are set based on measurements of fine sandy loam by Nikolaev et al. (2013).

For the CFGI model, the calibrated $F_{threshold}$ value (Table 9) is relatively close to the lower bound value of 56°C-days found in Molnau and Bissell (1983). For the modCFGI model, the calibrated $F_{threshold}$ value is at the lower bound. The $F_{threshold}$ value is expected to be lower for the modCFGI model than the CFGI model. The modCFGI model incorporates the insulation by ground cover directly using K_{gc} and D_{gc}, whereas the CFGI model can only account for those effects by adjusting the $F_{threshold}$ value. It is also worth noting that $K_{gc,FS30}$ has a very low value (minimum of allowable range), which suggests that insulation from grass in an unmanaged pasture is very small. This could be the result of snow falling within the grass of the unmanaged pasture, thus making any insulating contribution from the grass very small.

Table 9. Allowable ranges and calibrated values for the CFGI and modCFGI model parameters using PEST. Dashes indicate parameters that are not required in the associated model. The sensitivity ranking for the modCFGI parameters are shown in parentheses.

Parameter	Units	Allowable Range	Calibrated Values CFGI	Calibrated Values modCFGI
$F_{threshold}$	°C - days	5.00-83.00	52.55	5.00 (3)
K_{gc}	cm	0.001-1.000	--	1.033 (1)
$K_{gc,FS24}$	cm	0.001-1.000	--	1.887 (2)
$K_{gc,FS30}$	cm	0.001-1.000	--	0.001 (4)

Table 10. Values of soil parameters used to calculate soil moisture in the single-layer Green and Ampt infiltration model.

Parameter	Units	Value
saturated hydraulic conductivity	cm h^{-1}	2.040
effective porosity	cm^3 cm^{-3}	0.407
residual water content	cm^3 cm^{-3}	0.038
field capacity	cm^3 cm^{-3}	0.166
wilting point	cm^3 cm^{-3}	0.075
capillary head	cm	8.570
pore distribution arithmetic mean	cm cm^{-1}	0.466

4.4 Results and Discussion

4.4.1 Snow Depth and SWE (TI vs RTI)

Figure 20 shows maps of simulated snow depth on 23 February 2007 from the TI and RTI snow models. The spatial variability in the TI snowpack is entirely based on elevation (due to the inference of local air temperature from elevation). Higher elevations have deeper snowpack due to lower air temperatures. The RTI snowpack also varies with elevation but shows variation due to land cover as well. In particular, pasture areas have slightly shallower snowpack than surrounding areas due to higher sublimation rates and higher absorbed shortwave radiation. North-facing slopes also have more snow than south-facing slopes due to lower absorbed shortwave radiation. Although no maps of observed snow depth are available for comparison, large-scale distributions of snowpack are known to be controlled by elevation, land cover, and slope/aspect (Fassnacht et al., 2017; Jost et al., 2007), which is more consistent with the RTI model.

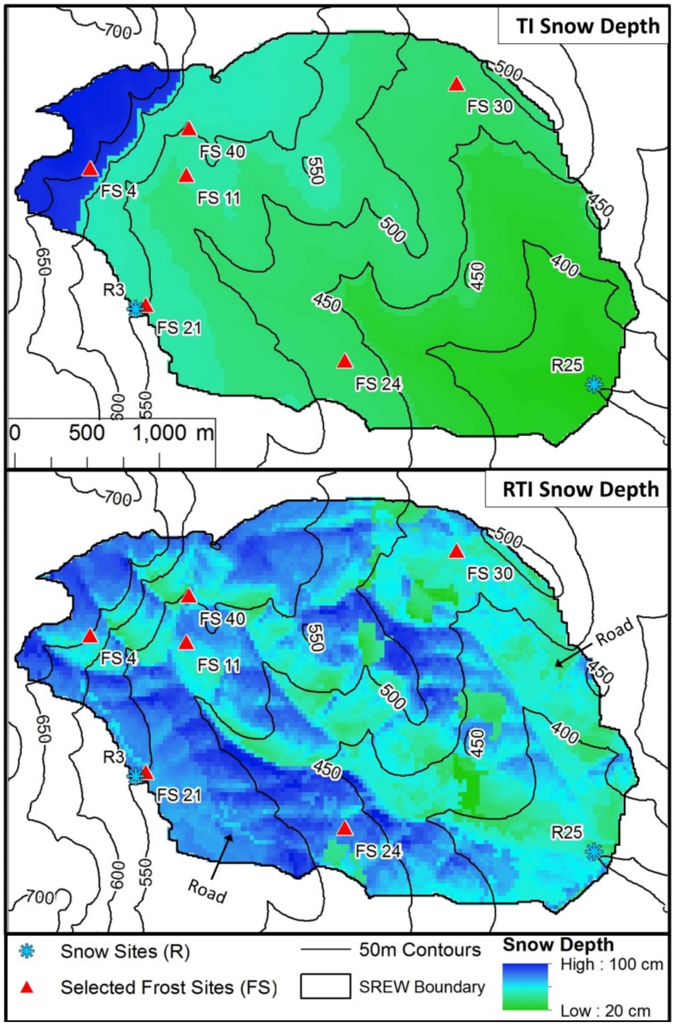

Figure 20. Simulated maps of snow depth (TI and RTI models) within the W-3 watershed for 23 February 2007. No observed maps of snow depth are available, but the map shows the differences between the temperature-based (TI) model and the modified (RTI) model.

Figure 21 shows the snow depths from the TI and RTI models at all 8 test locations and compares them to the observations. Root mean squared error (RMSE) and Nash-Sutcliffe Efficiency (NSE) are shown in Table 11 for the calibration period (WY 2006-2007), validation period (WY 2008-2010), and complete period (WY 2006-2010). The TI and RTI models track closely together at the 8 test locations despite differences in the snow depth shown in Figure 20. Differences between the TI and RTI snowpack at the test sites are small (Figure 21 and Table 11). The RTI model performs slightly better than the TI model in overall average RMSE (15.69 vs. 15.71 cm), while the TI model performs slightly better in overall average NSE (0.58 vs. 0.53). The observed snow depth is relatively low in WY2008 and 2009 at two of the pasture sites (FS24 and FS30) compared to the other sites. Specifically in WY2008 the small snow depth observations are not captured within either model. The R3 site is also classified as pasture yet has a higher snowpack in WY2008 and 2009. The higher snowpack at this pasture site may be explained by the proximity of R3 to forested areas, which may reduce the wind and help preserve the snowpack. Neither model considers wind effects.

The snow depths from the two models are similar at each location (Figure 21) because on average the available energy to melt snow (T_a in the TI model and T_{rad} in the RTI model) is similar (Figure 22). However, the diurnal variation of T_{rad} is typically greater than that of T_a. T_{rad} is derived from a simple radiation balance (i.e. neglecting other terms in the thermal energy balance). Thus, T_{rad} is higher than T_a during the day due to high $R_{\mathrm{SW}\downarrow}$ values, and it is typically lower than T_a at night because $R_{\mathrm{SW}\downarrow}$ reduces to 0 and ε_a (set to 0.757) in Eq. (48) limits the affect T_a has on $R_{\mathrm{LW}\downarrow}$ and therefore T_{rad}. As shown in Figure 22 the available energy is also similar between these locations. The elevation difference between the highest and lowest elevation site is approximately 300 m, corresponding to a maximum temperature difference of approximately 2°C between the sites. Also, the test sites are typically located on shallow slopes so topographic aspect has little influence on the energy available to melt the snowpack (i.e. T_{rad}). All land cover classifications except evergreen forest (FS11) have K_v values at or near 1 and L_{AI} values at or near 0, which reduces any variations due to land cover. T_{rad} at FS11 (evergreen forest) is different from the other 7 sites because its low K_v value (0.308) reduces $R_{SW,net}$ during the day, and a high L_{AI} value (1.0) increases $R_{LW\downarrow}$ during day and night.

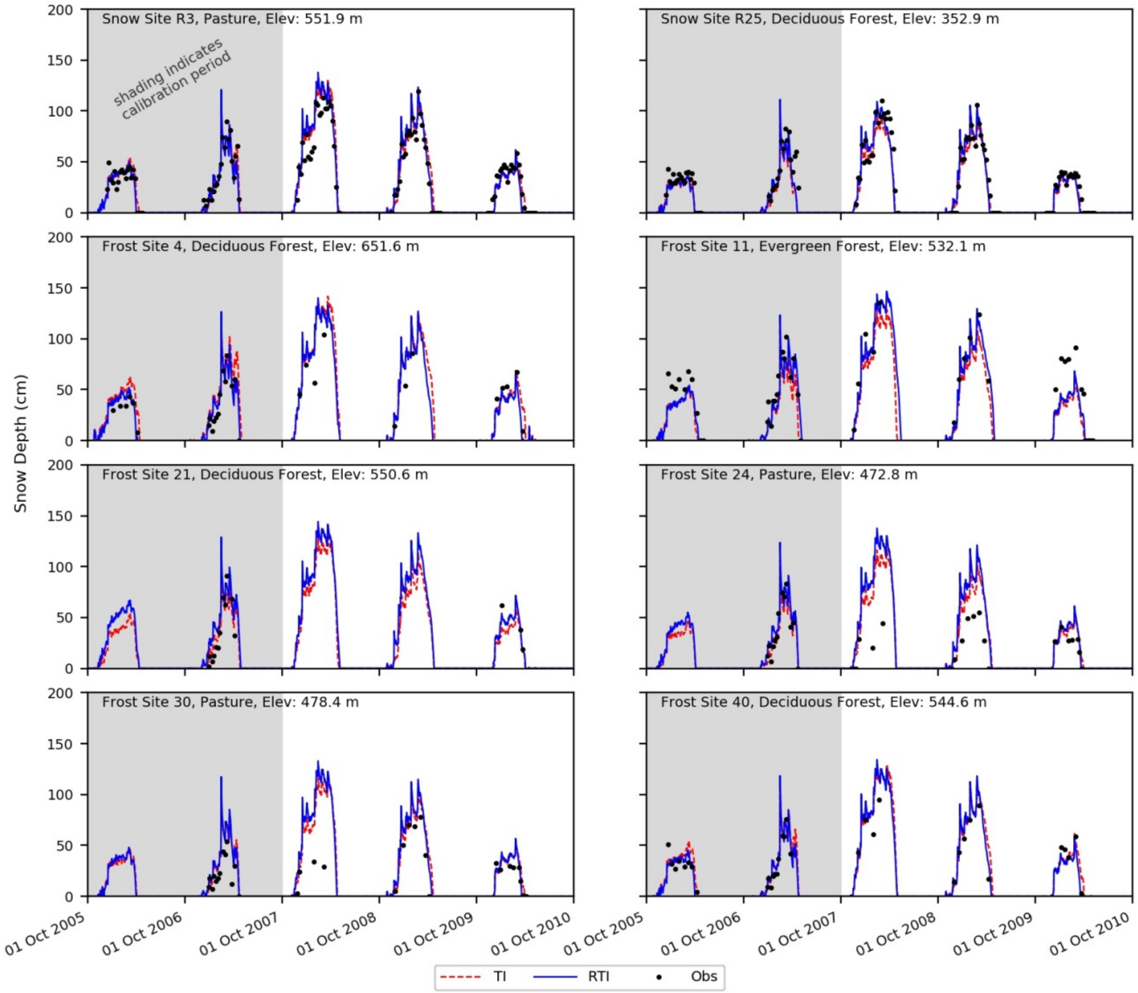

Figure 21. TI and RTI simulated snow depth at all eight test sites within the W-3 watershed.

Table 11. Statistics for TI and RTI snow depth values at all 8 test sites, and statistics for TI and RTI SWE values at the R3 and R25 snow test sites. Values are shown for calibration period (WY 2006-2007), validation period (WY 2008-2010), and overall (WY 2006-2010). RMSE values closer to zero and NSE values closer to one indicate better fit.

			Snow	Calibration		Validation		Overall	
	Site	Land Cover	Model	RMSE (cm)	NSE	RMSE (cm)	NSE	RMSE (cm)	NSE
Snow Depth	R3	Pasture	TI	6.6	0.91	12.1	0.89	10.6	0.89
			RTI	8.4	0.86	11.9	0.89	10.9	0.89
	R25	Deciduous Forest	TI	13	0.61	9.4	0.93	10.7	0.88
			RTI	12.2	0.65	9.2	0.93	10.3	0.89
	FS4	Deciduous Forest	TI	18.1	0.3	17	0.57	17.7	0.51
			RTI	9.4	0.81	15.4	0.64	12.1	0.77
	FS11	Evergreen Forest	TI	18.4	0.54	24.5	0.65	21.6	0.62
			RTI	15.8	0.66	19.3	0.78	17.6	0.75
	FS21	Deciduous Forest	TI	12.1	0.82	13	0.45	12.3	0.79
			RTI	18.1	0.59	6.1	0.88	16.4	0.62
	FS24	Pasture	TI	10.1	0.85	26.2	-1.18	21.3	0.08
			RTI	10.7	0.83	33.2	-2.51	26.7	-0.44
	FS30	Pasture	TI	16.1	-0.12	22.6	0.09	20.3	0.06
			RTI	17	-0.26	24.9	-0.1	22.2	-0.12
	FS40	Deciduous Forest	TI	9.3	0.74	13.1	0.74	11.2	0.78
			RTI	7.6	0.83	11.1	0.81	9.3	0.85
SWE	R3	Pasture	TI	2.1	0.9	3.3	0.91	3	0.91
			RTI	3.6	0.71	3.1	0.92	3.3	0.89
	R25	Deciduous Forest	TI	5.2	0.29	2.7	0.92	3.7	0.83
			RTI	5	0.35	3.1	0.91	3.8	0.82

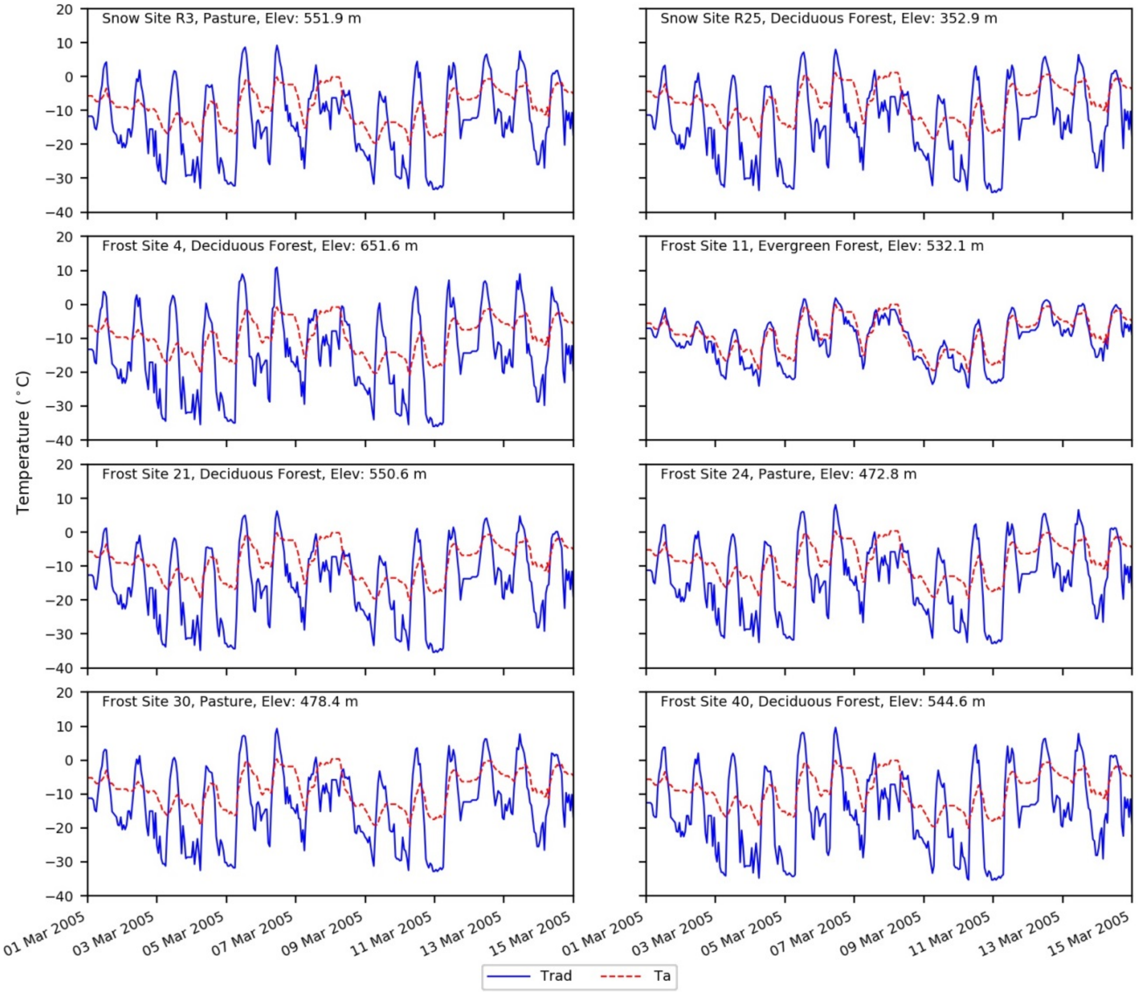

Figure 22. T_a and T_{rad} values at all eight test sites within the W-3 watershed between 01 March 2005 and 15 March 2005.

Figure 23 shows the simulated (both TI and RTI models) and observed SWE values, Table 11 shows the associated performance metrics at the R3 and R25 snow sites. The TI and RTI models are only calibrated to snow depth, but SWE is calculated first and then combined with snow density to determine snow depth. Both models use the same method to calculate snow density. Both models exhibit similar behaviour and performance at the two sites, which is consistent with their similar snow depths discussed earlier (Figure 21 and Table 11). Overall, these suggest that the snow density equations used within

GSSHA are relatively accurate at the W-3 watershed. Thus, accurate estimates of snow depth typically correspond to accurate estimates of SWE as well.

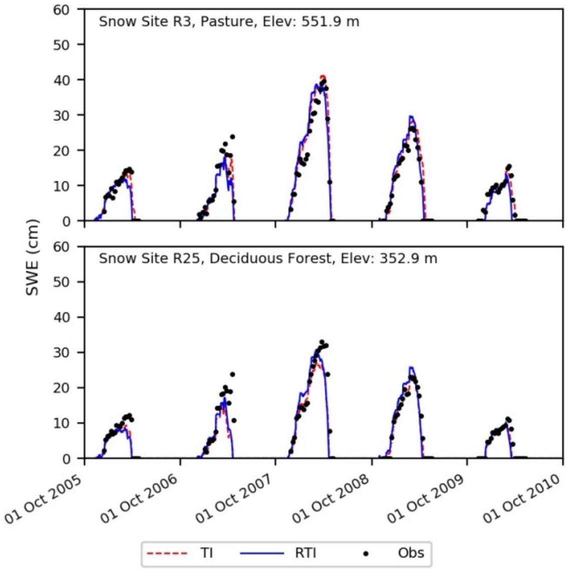

Figure 23. TI and RTI simulated SWE at R3 and R25 snow sites within the W-3 watershed.

4.4.2 Frost Depth (CFGI vs modCFGI)

Figure 24 shows simulated frost depth maps for 23 February 2007 using the CFGI and modCFGI models (no maps of observed frost depths are available for comparison). In the CFGI model, the frost depths mainly depend on elevation. Colder temperatures at higher elevations generally result in greater snowpack, which insulates the ground and produces smaller frost depths. However, at the beginning of the snow season when the snowpack is shallow, low temperatures at high elevations create deep frost in the higher elevations of the watershed. Later, deeper snowpack at high elevations insulate the ground, while the frost depth increases at lower elevations. This reversal in the elevation dependence can produce an inversion (localized minima in frost depth), as seen between the 500 and 650 m contour lines in Figure 24. The modCFGI frost depth also has some elevation dependence, but the spatial variation mainly follows land cover classification, which is similar to observations of frozen ground in the Swiss pre-alpine zone (Stähli, 2017). This variation is partly due to the use of T_{rad} and the increased heterogeneity in the snow depth. The effect of snowpack can be seen by comparing hillslopes with the same land cover but different orientations, such as along the 500 m contour south of FS11. Lower T_{rad} values on northeast-facing slopes result in deeper snowpack than the southwest-facing slopes (Figure 20). This deeper snowpack produces shallower frost depths on the northeast-facing slopes due to insulation by the snow. However, the spatial pattern of frost depth is more heavily affected by the land cover. Land cover's impact largely occurs through the associated ground cover. This effect can be seen by comparing the deep frost at the unmanaged pasture (near FS30) with the shallower frost depth at the deciduous forest areas near FS4, FS21, and FS40. The low ground cover reduction coefficient at the unmanaged pasture ($K_{gc,FS30}$) reduces the insulation from the ground cover, creating deeper frost compared to the deciduous forest areas. The larger than expected role of ground cover in the modCFGI model may occur because ground cover is present during the initiation, deepening, and decrease of frost depth, while the snowpack is much more variable throughout the season.

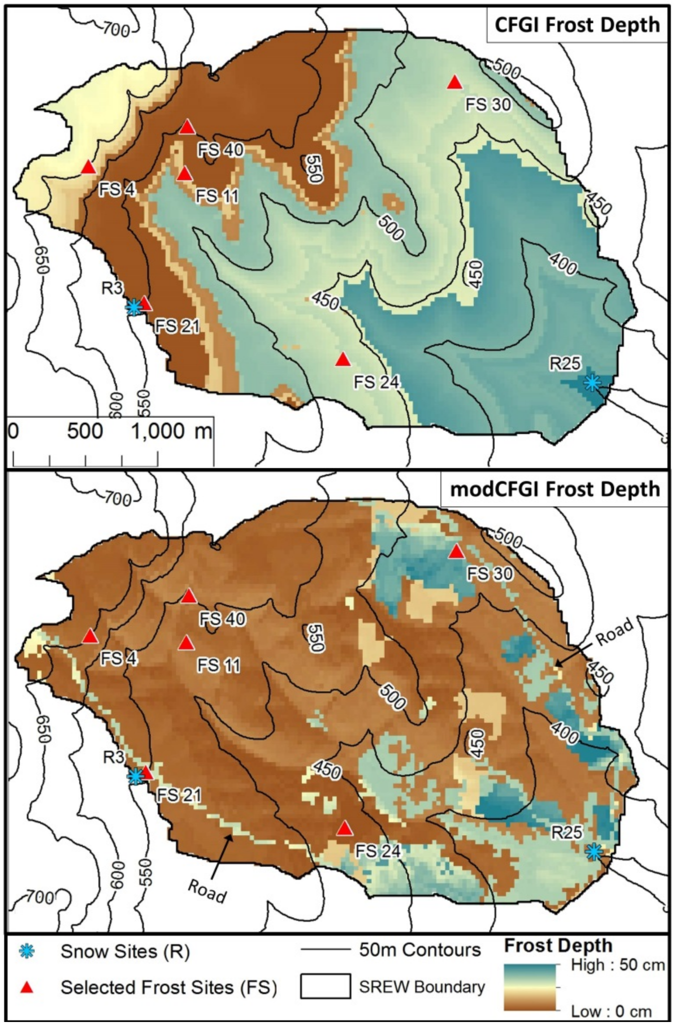

Figure 24. Simulated maps of frost depth (CFGI and modCFGI models) within the W-3 watershed for 23 February 2007. No observed maps of frost depth are available, but the map shows the differences between the temperature-based (CFGI) model and the modified (modCFGI) model.

Figure 25 shows the frost depths from the CFGI and modCFGI models along with the frost depth observations. The RMSE and NSE values during the calibration, validation, and overall periods are shown in Table 12. The simulated frost depth remains more constant amongst the sites when using the CFGI model, which produces similar maximum frost depths for a given year independent of the land cover. The modCFGI results deviate considerably from the CFGI results, producing greater frost depths at the unmanaged pasture (FS30) and evergreen (FS11) sites and smaller frost depths at the deciduous (FS4, FS21, and FS40) and managed pasture (FS24) sites. These simulated differences between the sites are consistent with the observations. The decreased frost depth in the deciduous forest and managed pasture result from their high measured litter depth ($D_{gc} = 6$ cm) and high reduction coefficient ($K_{gc,FS24} = 1.887$ cm^{-1}), respectively. The two pasture sites (FS24 and FS30) differ considerably in the observed frost depth with FS30 consistently having deeper frost. This difference likely occurs because FS24 is managed and FS30 is not. With the exception of the validation period at FS30, the modCFGI model performs better (lower RMSE and higher NSE values) than the CFGI model. The difference in performance is most pronounced at the deciduous sites (FS4, FS21, and FS40) where the average overall NSE value is -11.9 for the CFGI model and 0.20 for the modCFGI model.

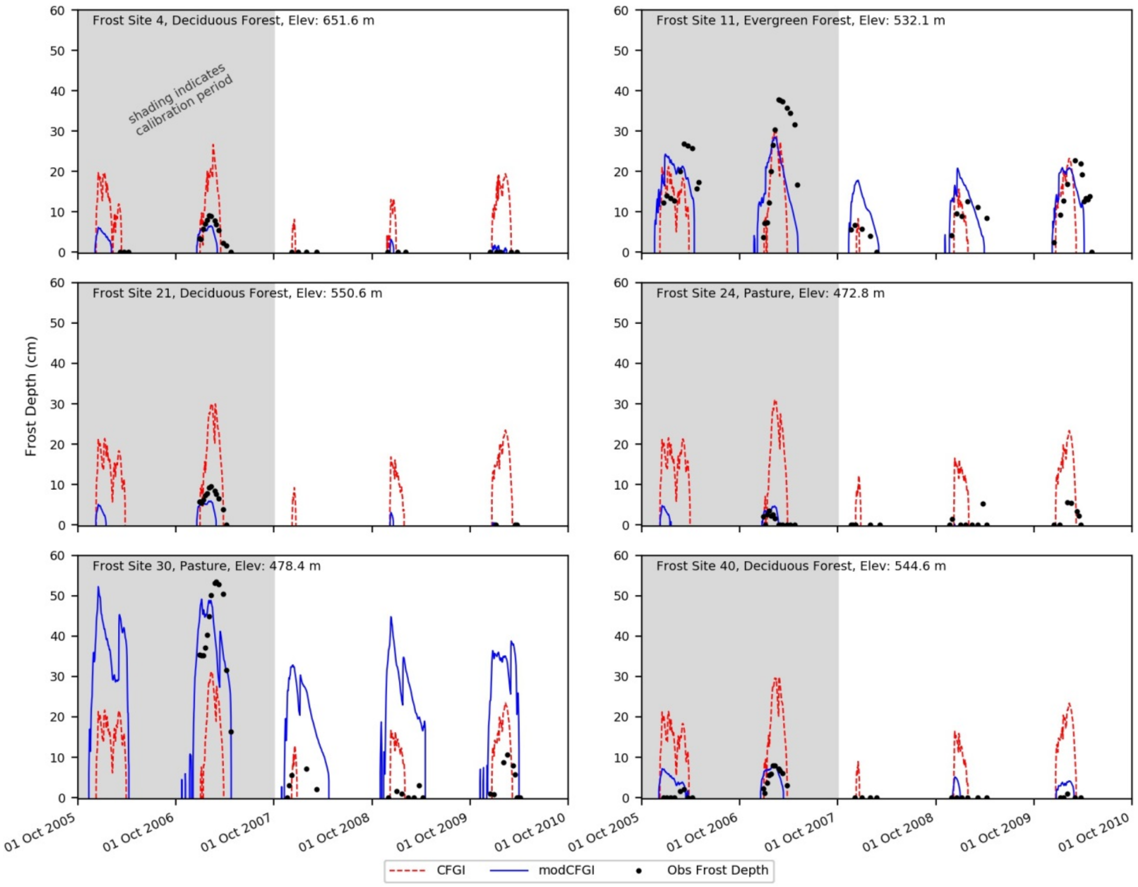

Figure 25. Observed frost depth compared against simulated (CFGI and modCFGI) frost depth at all 6 selected frozen ground test sites within the W-3 watershed.

Table 12. Statistics for CFGI and modCFGI frost depth at all 6 frost sites. Values are shown for calibration period (WY 2006-2007), validation period (WY 2008-2010), and overall (WY 2006-2010). RMSE values closer to zero and NSE values closer to one indicate better fit. No frost was present at FS4 and FS21 during the validation period, resulting in an inability to calculate NSE. Statistics for a recalibrated modCFGI model without ground cover (labelled as "modCFGI no gc") are also shown.

		Frost Depth	Calibration		Validation		Overall	
Site	Land Cover	Model	RMSE (cm)	NSE	RMSE (cm)	NSE	RMSE (cm)	NSE
FS4	Deciduous Forest	CFGI	8.2	-5.0	5.7	NA	7.2	-3.8
		modCFGI	2.5	0.4	0.2	NA	1.9	0.7
		modCFGI no gc	26.5	-62.9	16.0	NA	22.6	-45.9
FS11	Evergreen Forest	CFGI	15.5	-1.2	9.9	-1.6	13.1	-0.6
		modCFGI	12.6	-0.5	8.2	-0.8	10.7	-0.1
		modCFGI no gc	17.5	-1.8	10.9	-2.1	14.6	-1.0
FS21	Deciduous Forest	CFGI	12.5	-24.2	8.4	NA	11.8	-10.9
		modCFGI	3.9	-1.5	0.0	NA	3.5	-0.1
		modCFGI no gc	26.2	-109.8	14.3	NA	24.3	-49.4
FS24	Pasture	CFGI	17.5	-188.5	7.3	-12.3	12.4	-49.1
		modCFGI	1.4	-0.3	2.3	-0.3	2.0	-0.3
		modCFGI no gc	28.2	-490.0	13.5	-44.3	20.6	-137.4
FS30	Pasture	CFGI	27.5	-5.8	6.2	-2.4	17.7	0.2
		modCFGI	11.7	-0.2	24.9	-55.0	20.9	-0.1
		modCFGI no gc	18.1	-2.0	11.4	-10.8	14.4	0.5
FS40	Deciduous Forest	CFGI	14.2	-22.6	10.1	-1642	12.6	-20.9
		modCFGI	3.4	-0.3	1.8	-52.1	2.8	-0.1
		modCFGI no gc	36.9	-157.9	21.8	-7631	31.2	-133.1

In hydrologic models, capturing the presence of frozen ground is important because even shallow frost with high moisture content (concrete frost) has the potential to impede infiltration (Dunne and Black, 1971). Therefore, the ability of the CFGI and modCFGI models to accurately capture the presence of frozen ground is evaluated. Whenever frost observations are available, the simulated frost depths are categorized as: True Positive (both simulated and observed data show frost), True Negative (both simulated and observed data show no frost), False Positive (simulated data shows frost but observed data shows no frost), or False Negative (simulated data shows no frost but observed data shows frost). Table 13 shows the number of observations in each category for each test site. The table also shows the model accuracy, which is calculated as the percent of the observations that are correctly classified (True Positive or True Negative). The CFGI and modCFGI models perform similarly in capturing True Positives at FS4, FS21, FS24, and FS40, while modCFGI has more True Positives at FS11 and FS30. The lower True Positives and higher False Negatives indicate that the CFGI model tends to underestimate the presence of frozen ground at FS11 and FS30. Overall, both the CFGI and modCFGI models capture most of the frozen ground events, with the modCFGI model performing better than the CFGI model at 5 sites and worse at 1 site (FS21). The average accuracy of the modCFGI model is 15.2% higher than the CFGI model, with the largest increase in accuracy at FS11 (29.8%).

Table 13. Number of True Positive (both simulated and observed data show frost depth) True Negative (both simulated and observed data show no frost depth), False Positive (simulated data shows frost depth but observed data does not), and False Negative (simulated data shows no frost depth but observed data shows frost depth) occurrences during the entire test period. The Accuracy is the sum of the True Postive and True Negative divided by the total number of observations.

Site	Land Cover	Elev (m)	Model	True Positive	True Negative	False Positive	False Negative	Accuracy (%)
FS4	Deciduous Forest	651.6	CFGI	9	12	4	3	75.0%
			modCFGI	9	15	1	3	85.7%
FS11	Evergreen Forest	532.1	CFGI	24	2	0	21	55.3%
			modCFGI	39	1	1	6	85.1%
FS21	Deciduous Forest	550.6	CFGI	10	3	1	1	86.7%
			modCFGI	8	4	0	3	80.0%
FS24	Pasture	472.8	CFGI	7	12	9	5	57.6%
			modCFGI	6	20	1	6	78.8%
FS30	Pasture	478.4	CFGI	16	8	0	10	70.6%
			modCFGI	26	1	7	0	79.4%
FS40	Deciduous Forest	544.6	CFGI	13	9	11	1	64.7%
			modCFGI	13	12	8	1	73.5%
Total			CFGI	79	46	25	41	65.4%
			modCFGI	101	53	18	19	80.6%

A simple test is employed to explore the modification that contributes most to the increased accuracy of the modCFGI model. This test removes ground cover from the modCFGI model, recalibrates, and then compares the results to observations. When ground cover is removed, the calibrated $F_{threshold}$ value is 83 °C-days, which is at the top of the calibration range. This change indicates that ground cover has a large impact on the appropriate value of this threshold. Figure 26 shows the simulated frost depths using the modCFGI model with and without ground cover for each test site. Performance metrics for the modCFGI model with and without ground cover are shown in Table 12. Variability in frost depth between the sites is diminished when ground cover is removed, leading to large errors between simulated and observed frost depth. When ground cover is removed, the frost depth results decrease in accuracy (higher RMSE values and lower NSE values) compared to the complete modCFGI model. The only exception is the overall period at FS30, which is also the only site where the CFGI model outperforms the full modCFGI model. These results suggest that inclusion of ground cover is an important reason why the modCFGI model outperforms the CFGI model.

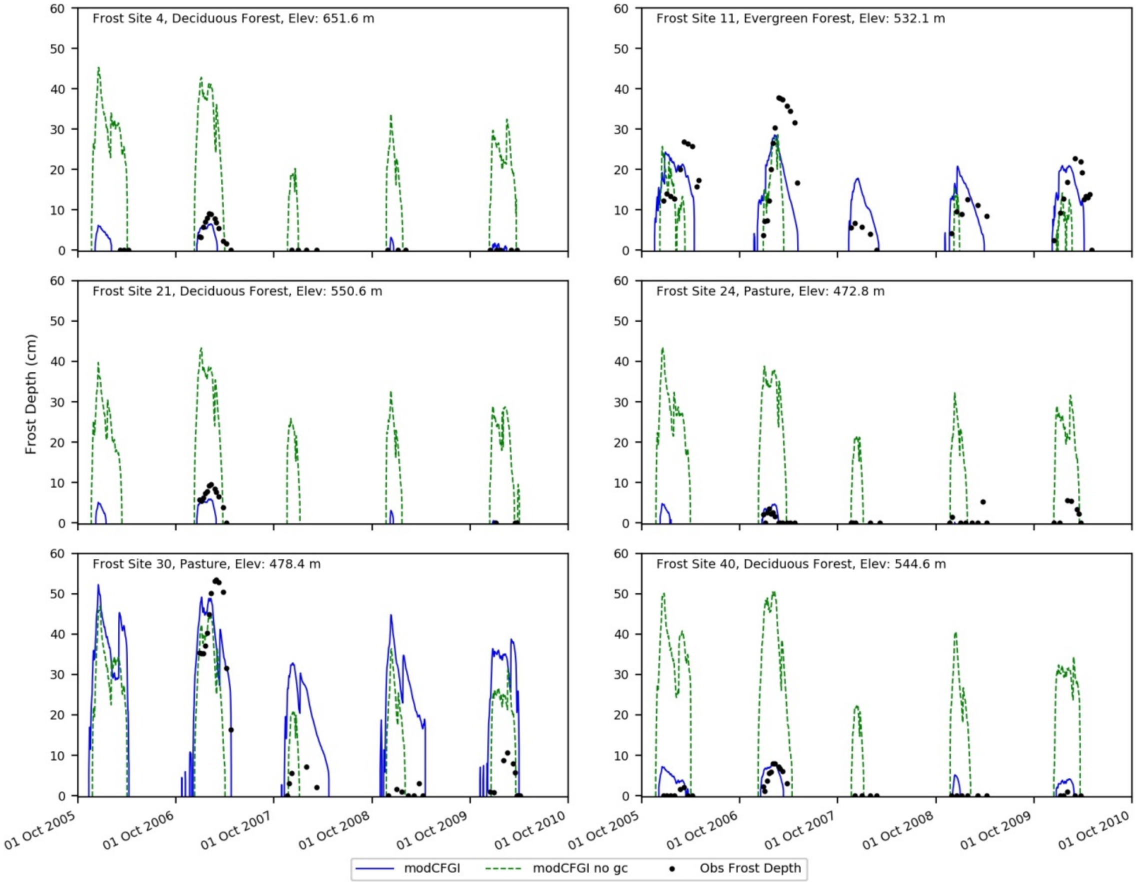

Figure 26. Observed frost depth compared against simulated (modCFGI with and without ground cover included) frost depth at all 6 selected frozen ground test sites within the W-3 watershed. The modCFGI model without ground cover is labelled as “modCFGI no gc”.

The sensitivity of the modCFGI results to soil moisture is also examined. Soil moisture does not affect the calculation of F, but it is included within the modified Berggren Equation (Eq. (51) and (52)) in the calculation of δ (Eq. (53)) and Ω_m (Eq. (54)). Soil moisture was simulated using a single layer Green and Ampt approach. However, no soil moisture measurements are available at any of the test sites to evaluate the accuracy of the simulated values. Sensitivity of the modCFGI model to volumetric soil moisture is tested by artificially setting the soil moisture to either the residual water content (θ_{low}) or the effective porosity (θ_{high}), which are the lower and upper bounds for soil moisture values within the model. Figure 27 shows the modelled frost depths from the modCFGI model using θ_{low}, θ_{high}, and the soil moisture from the Green and Ampt approach (θ_{sim}, which is identical to modCFGI in Figure 25 and Figure 26). Also shown are the observed frost depths for reference only. The frost depth from the θ_{sim} case is similar to the frost depth from the θ_{high} because the simulated soil moisture is usually close to the effective porosity. Frost depth increases when θ_{low} is used, which coincides with other studies (Fox, 1992; Willis et al., 1961). The timing of the frozen ground (when it begins and ends) is identical in all three of the simulations. The consistent timing occurs because soil moisture is not used to calculate F and the same $F_{threshold}$ (which controls when frozen ground begins) was used for all three simulations. This result highlights a deficiency in the modelling framework. Specifically, soil moisture should be considered for determining the initiation of frozen ground because wet soils have a higher specific heat capacity and require more energy loss to cool and freeze the soil (Kurganova et al., 2007).

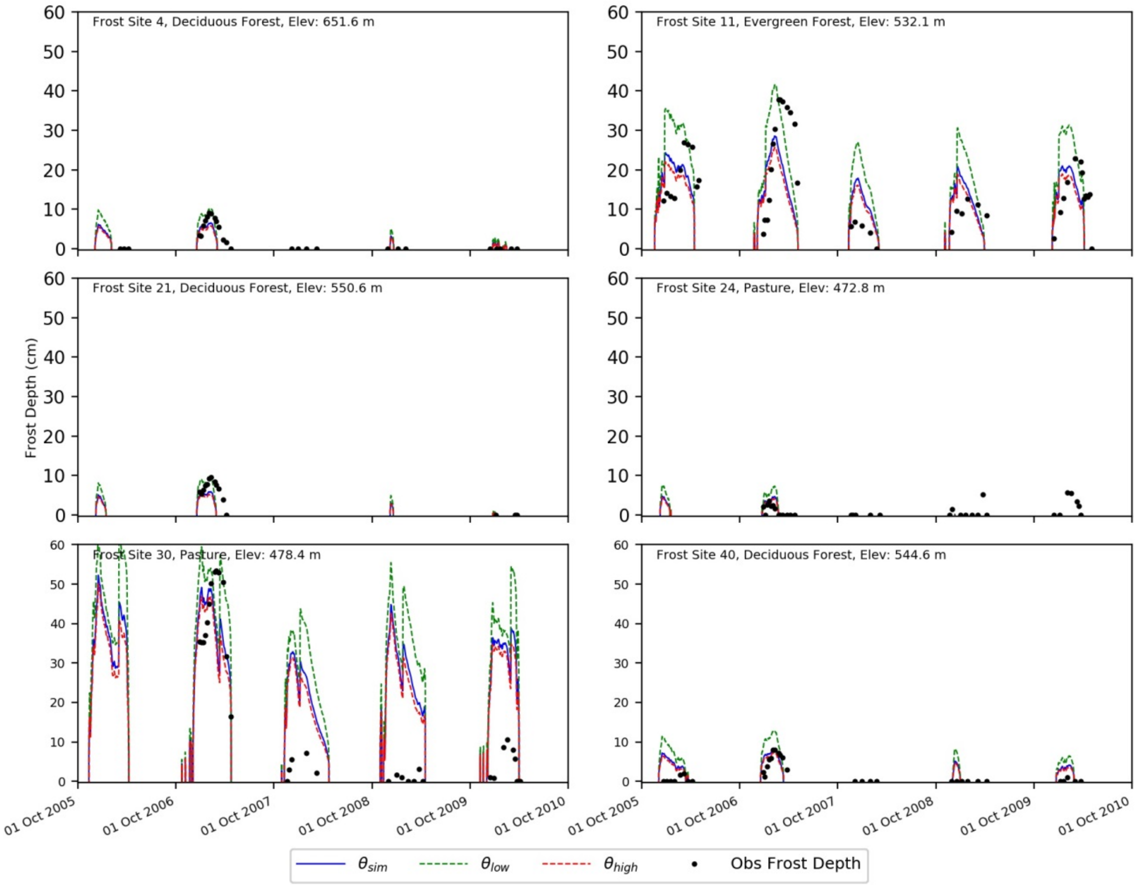

Figure 27. Simulated frost depths from the modCFGI model using simulated soil moisture (θ_{sim}), a constant high soil moisture (θ_{high}), and a constant low soil moisture (θ_{low}) at all 6 selected frozen ground test sites within the W-3 watershed.

4.5 Conclusions

The main purpose of this paper was to better estimate the spatial pattern of frozen ground for distributed watershed modelling by modifying an existing degree-day frozen ground model (CFGI), which uses a frost index value to determine whether the ground is frozen or not. The modifications to the CFGI model include: 1) use of a radiation-derived temperature index (RTI) snow model instead of a standard temperature-index (TI) snow model, 2) use of a radiation-derived proxy temperature (T_{rad}) instead of air temperature (T_a) in the calculation of the frost index, 3) inclusion of ground cover (litter, debris, grass, etc.) as an insulator of the ground from air temperatures, and 4) an option to use a version of the modified

Berggren Equation to calculate frost depths based on the frost index values. The CFGI and modCFGI models were tested using the GSSHA hydrologic model over a five-year period within the W-3 watershed, which is part of Sleepers River Experimental Watershed in Vermont. The model results were compared against snow depth at eight sites, snow water equivalent at two sites, and frost depth at six sites.

The primary conclusions of the paper are as follows:

1.) The RTI snow model produces much more complex spatial patterns of snow depth than the TI snow model for the W-3 watershed. The TI model, which is based on SNOW-17 (Anderson, 2006), only produces spatial variation using elevation. The RTI model accounts for elevation, hillslope orientation, canopy shading, and longwave radiation from the canopy through the use of the radiation-derived proxy temperature. It also includes a simple sublimation method based on solar radiation. Thus, its snow depths exhibit spatial heterogeneity based on elevation, slope/aspect, and land cover, all of which are known to affect the largescale distribution of observed snow depths (Fassnacht et al., 2017; Jost et al., 2007).
2.) Both the RTI model and TI model produce accurate results for the eight snow depth sites at W-3. Two of the eight sites also measure snow water equivalent, where the RTI and TI model also show similarly accurate results. The eight test sites have similar topographic attributes and primarily differ in their land covers, which include pasture, deciduous forest, and evergreen forest. Because the leaves have typically fallen prior to snow accumulation, all but the evergreen site behave similarly in snow accumulation and ablation.
3.) The modCFGI frost model produces more complex spatial patterns of frost depth than the CFGI frost model for the W-3 watershed. The CFGI model uses elevation to infer the spatial variation of air temperature. It also uses the TI model for snow depth, which also depends on elevation. Thus, the simulated frost depths at W-3 primarily reflect the watershed elevations. In contrast, the modCFGI model uses the radiation-derived proxy temperature to infer the energy available to heat the ground and the RTI model to simulate snow depth. Furthermore, it accounts for the

insulating effects of ground cover (in addition to snowpack), which also depends on the land cover. Thus, the frost depths simulated by the modCFGI model at W-3 depend on the local elevation, hillslope orientation, and land cover, all of which are known to affect the distribution of frozen ground (Fox, 1992; MacKinney, 1929; Wilcox et al., 1997; Willis et al., 1961).

4.) The modCFGI model produces more accurate frost depths than the CFGI for all but one of the six test sites in the W-3 watershed. Overall, the modCFGI model more accurately captures the inter-annual variability in frost depth at a given site and variability of frost depth between sites. Although both the CFGI and modCFGI capture the majority of frozen ground events observed, the modCFGI model has 15.2% better accuracy in capturing the presence of frozen ground, which is expected to be important for capturing runoff that is produced by frozen ground.

5.) A key reason for the difference in performance between the two frost models is that the modCFGI model includes the insulation of the ground by ground cover while the CFGI model does not. When ground cover is removed from the modCFGI model its results for W-3 are less accurate and the variability in simulated frost depth between the sites is limited. Ground cover is likely important in this watershed because it is relatively thick and is also present at all stages of the winter while snowpack is not.

Overall, the modCFGI model provides improved spatial representation of frozen ground while requiring only cloud cover estimates as additional forcing data (more forcing data may be required if soil moisture is simulated to obtain frost depth). Limited data requirements should make modCFGI well-suited for data sparse environments. Hydrologic models often need to account for the presence of frozen ground, which in data-sparse environments often means using simple degree-day approaches that typically vary frozen ground with elevation only (as was shown with the CFGI model). To calculate T_{rad} the modCFGI model does require cloud cover data, which are collected operationally at most airports within the U.S. If soil moisture is explicitly simulated within the hydrologic model the modCFGI model can also be used with the modified Berggren Equation to simulate frost depth, which requires information on soil type and an estimate of the thermal conductivity of the soil.

Five main avenues are available for future research. First, the modCFGI model should be generalized to include the effects of wind (as it relates to the snowpack) and more completely consider the role of soil moisture. Soil moisture is not considered when calculating the frost index, so it does not impact the initiation or duration of frozen ground. This limitation results from using a degree-day approach and may be important in some cases (Kurganova et al., 2007; Willis et al., 1961). Second, the modCFGI model should be tested further. Additional testing should consider other areas where snow and frozen ground are known to affect runoff, such as the Upper Midwest region of the United States. Additional testing should also better characterize the insulation properties of ground cover under different management scenarios. Third, the calculation of T_{rad} is simple and applicable in data-sparse environments, but other approaches for adjusting a temperature value based on topography and land cover are available (Fox, 1992; Kang, 2005; Webster et al., 2017) and could be further tested. Fourth, future research should also determine the effects of spatial heterogeneity of snow and frost depth on runoff and streamflow at both the local and watershed scales. Similar to Campbell et al. (2010), the RTI and modCFGI models could be used in data-sparse watersheds to investigate how changes in historic and future climate affect snow, frozen ground, and runoff. Finally, although this paper focuses on the simulation of frost depth in the context of watershed modelling, the methods described could also be used for agriculture, overland mobility modelling, and infrastructure where snow and frost depth are major concerns.

CHAPTER 5. CONCLUSIONS

5.1 Summary

This dissertation presented simple modifications to existing temperature-based models of snow and frozen-ground to improve the representation of available energy while limiting the required forcing data (forcing data is limited to temperature, precipitation, and cloud cover data). When tested at the watershed scale, the modifications were shown to improve the spatial simulation of snow and frozen ground produced by a distributed hydrologic model. The improvement in spatial snow simulation was also shown to improve streamflow simulation. Although the modifications are developed within the GSSHA hydrologic model, they can be applied to other numerical watershed models, frameworks, or applications.

Topography and land cover are known to affect the spatial distribution of the snowpack, but their roles are not fully realized in many pre-existing models. Many numerical snow models use air temperature as a surrogate for the available energy, but relying solely on air temperature neglects the role of shortwave radiation and limits the consideration of spatial variability in the available energy. This dissertation introduces the radiation-derived proxy temperature T_{rad} that is calculated from both the shortwave and incoming longwave radiation. The longwave component includes contributions from the air temperature (through a temperature-elevation relationship), cloud cover, and vegetation cover. The shortwave component accounts for variations in slope, aspect, terrain shading, vegetation shading, albedo of the snowpack, location on earth, time of year, and atmospheric scattering. Air temperature was replaced with T_{rad} within the commonly-used SNOW-17 (Anderson, 1973; 2006) snow model, creating the Radiation-derived Temperature Index (RTI) snow model. The RTI and original SNOW-17 model (referred to as TI snow model) were tested at two watersheds. When tested at Senator Beck Basin (SBB) in Colorado (an alpine watershed with high relief) the RTI model showed improvement in simulating the spatial pattern of snowpack. Specifically, the RTI model better captures differences in snowpack due to slope and aspect.

These improvements led to improved streamflow simulations. When tested at Sleepers River Experimental Watershed (SREW) in Vermont (a heavily-forested watershed), the RTI model produces much more complex spatial patterns of snow depth than the TI snow model because it accounts for longwave radiation from the canopy, canopy shading, elevation, and hillslope orientation.

Topography and land cover also are known to affect seasonal frozen ground, but they are not fully considered by many pre-existing models due to their use of air temperature as a surrogate for available energy. Air temperature was replaced by T_{rad} as the source of available energy within the Continuous Frozen Ground Index (CFGI) model (Molnau and Bissell, 1983), creating the modified CFGI model (referred to as modCFGI). The modCFGI also utilizes the RTI snow model to account for snow depth (which insulates the ground) and includes ground cover (i.e. litter depth) as an additional insulator of the ground. By utilizing T_{rad} and incorporating ground cover, the modCFGI produces more complex spatial patterns of frozen ground than the CFGI model when tested at SREW. When compared to frost depth data at six point sites, the modCFGI provided improved estimation of both presence and depth of frozen ground under varying land cover types.

The main contributions of this dissertation include the following:

1.) T_{rad} can be utilized within temperature-based index methods as a means to incorporate spatial heterogeneity of available energy at the snow and ground surface. T_{rad} accounts for the affects of topography and land cover on the net radiation balance, which are important drivers for both snow and frozen ground. When tested at SBB and SREW, the use of T_{rad} improves estimation of snow cover patterns. It also improves simulated temporal and spatial patterns of frozen ground at SREW. T_{rad} is not a physical quantity (one cannot measure T_{rad}), but it is a proxy temperature that can be used within temperature-based methods to represent available energy from net shortwave and longwave radiation.

2.) Improved simulation of the spatial distribution of snowpack results in improved simulation of streamflow at SBB. Also, calibrating the RTI snow model to snow covered area (SCA) instead of snow water equivalent (SWE) sites results in more accurate SCA and streamflow estimation. The snow simulation and streamflow results from SBB indicate that the RTI snow model better accounts for the spatial distribution of SWE and melting patterns within the watershed than the TI snow model.

3.) A method to include ground cover into a temperature-based frozen ground method was developed. Inclusion of ground cover as an insulator of the ground is the most important reason that the modCFGI model outperforms the CFGI model in the SREW test case. When ground cover is removed from the modCFGI model, the simulated frost depths between the SREW sites become more uniform (all have similar depths) and are less accurate. Ground cover is likely important in many forested watersheds because it is relatively thick and is present at all stages of the winter (while snowpack may not always be present).

Temperature-based snow and frozen ground models are often used in operational frameworks due to their limited data requirements, but they often neglect the effect of topographic attributes like aspect, slope, and shading as well as the effect of landcover on the available energy. Energy-balance snow and frozen ground models have the ability to capture the spatial variability of available energy, but require large amounts of forcing data (typically unavailable in most watersheds). The RTI snow model and modCFGI frozen ground model provide a compromise between temperature-based and energy-balance methods, where spatial heterogeneity of available energy from net radiation can be captured while limiting the forcing data requirements. With the use of fully-distributed hydrologic models becoming more common in planning and operational frameworks, the use of the RTI snow model and modCFGI frozen ground model may prove to be beneficial.

5.2 Future Avenues of Research

Several avenues are available for future research:

1.) The RTI model assumes a linear temperature-elevation relationship and neglects the effects of wind scour and emission of longwave radiation from nearby topography, all of which may cause errors in the simulation of SWE, SCA, and the subsequent streamflow. Inclusion of wind scour (using wind speed and direction data) and a more dynamic temperature-elevation relationship (using relative humidity measurements) may improve the snowpack simulations.
2.) The RTI model also neglects the effects of dust. Recent research has shown that the impacts of dust on surface albedo can be important, and radiative forcing by dust can have a primary role in snowmelt and the subsequent streamflow hydrographs (Painter et al., 2018; Skiles et al., 2015). Inclusion of dust in the albedo calculation within the RTI model could be a simple approach to simulate the affects of dust on the snowpack and runoff without requiring an energy balance snow model.
3.) Several factors influence the presence and depth of frozen ground. Soil moisture is not considered when calculating the frost index in the modCFGI model, so it does not impact the initiation or duration of frozen ground. The frozen ground threshold (used to determine when frozen ground initiates) could be set as a variable depending on initial soil moisture conditions.
4.) The insulating properties of ground cover were shown to be important considerations when simulating frozen ground using modCFGI. Additional testing should better characterize the insulation properties of various ground covers within modCFGI under different management scenarios. This research could lead to more applications of modCFGI in agriculture, overland mobility modelling, and infrastructure where snow and frost depth are major concerns.
5.) Future research should also determine if better capturing the spatial heterogeneity of frozen ground within a hydrologic model improves runoff and streamflow estimation at both the local and watershed scales. This study showed a simple method to simulate the presence of frozen ground, but did not explore how frozen ground impacts the runoff from a melting snowpack.

Building upon existing work (e.g. Zhao and Gray (1999)), more research is required to show when and how frozen ground reduces infiltration and results in increased runoff and streamflow.

6.) The scope of this research was limited to small mountain watersheds (SBB is 2.9 km^2; W-3 is 8.5 km^2). Spatial heterogeneity of the snowpack and frozen ground may be more varied in larger watersheds that exhibit more heterogeniety in topography and land cover. Applications of the RTI/modCFGI models should be explored in other regions with flatter topography where snow and frozen ground are known to affect runoff, such as the upper Midwest region of the United States. Streamflow estimation between the TI and RTI models may be more similar in larger basins where the attenuation of streamflow can smooth the deviations (Rango and Martinec, 1995). Future research should assess the differences in streamflow estimation between the TI and RTI models for larger snow-dominated basins.

7.) The RTI/modCFGI models could also be applied in land-cover and climate change scenarios. Similar to Campbell et al. (2010), the RTI and modCFGI models could be used (particularly in data-sparse watersheds) to investigate how changes in historic and future climate affect snow, frozen ground, and runoff. Deforestation due to land repurposing (i.e. conversion of forest to agriculture land), fire, and outbreaks of insect infestations may change the seasonal snowpack and presence of frozen ground, which might affect snowmelt runoff, sediment transport, and the general ecology of the watershed.

8.) The RTI and modCFGI models could be implemented within other hydrologic models. In this dissertation, the RTI and modCFGI models were tested within the GSSHA model, and the RTI snow model is currently being implemented into the Hydrologic Engineering Center - Hydrologic Modeling System (HEC-HMS; Scharffenberg and Fleming, 2006) by the U.S. Army Corps of Engineers (USACE). Once implemented, RTI will be an optional snow model for gridded implementations of HEC-HMS, which are currently being developed throughout the United States as part of the Corps Water Management System. The modCFGI model is scheduled to be included as a frozen ground option within HEC-HMS after the RTI model is fully-implemented.

Tentative plans have also been made to replace a continental-scale TI snow model for northern Eurasia (operated under an USACE contract) with the RTI model. This updated snow model will then help inform the Streamflow Prediction Tool (Follum et al., 2017; Snow et al., 2015; Wahl et al., 2016) operated by USACE to provide flow and flood inundation forecasts outside of the continental U.S.

9.) The proxy temperature T_{rad} could be utilized to simulate other hydrologic processes that vary spatially. One example is potential evapotranspiration (PET). The Hargreaves equation (Hargreaves and Samani, 1985) uses both air temperature and an empirical estimate of solar radiation to estimate PET. This approach may benefit from the use of T_{rad}, which could potentially provide better estimates of available energy and its spatial variability.

REFERENCES

Aguado, E., 1985. Radiation Balances of Melting Snow Covers at an Open Site in the Central Sierra Nevada, California. Water Resources Research, 21(11): 1649-1654.

Aldrich Jr, H.P., 1956. Frost penetration below highway and airfield pavements. Highway Research Board Bulletin (135), 124.

Allen, R.G., Walter, I.A., Elliott, R., Howell, T., Itenfisu, D. Jensen, M., 2005. The ASCE Standardized Reference Evapotranspiration Equation. ASCE.

Anderson, E.A., 1973. National Weather Service River Forecast System - Snow Accumulation and Ablation Model. Technical Memorandum NWS Hydro-17, 217 pp.

Anderson, E.A., 1976. A point of energy and mass balance model of snow cover. U.S. National Oceanic and Atmospheric Administration NOAA Technical Report NWS 19, Silver Spring, MD.

Anderson, E.A., 2006. Snow Accumulation and Ablation Model - SNOW-17, NWSRFS User Documentation. U.S. National Weather Service, Silver Springs, MD. http://www.nws.noaa.gov/oh/hrl/nwsrfs/users_manual/part2/_pdf/22snow17.pdf

Aquaveo, 2013. Watershed Modeling System Version 9.1.4, Provo, UT.

Ball, G.H., Hall, D.J., 1965. ISODATA, a novel method of data analysis and pattern classification. DTIC Document.

Barrett, A.P., 2003. National operational hydrologic remote sensing center snow data assimilation system (SNODAS) products at NSIDC. National Snow and Ice Data Center, Cooperative Institute for Research in Environmental Sciences.

Barros, A.P., Lettenmaier, D.P., 1993. Dynamic modeling of the spatial distribution of precipitation in remote mountainous areas. Monthly weather review, 121(4): 1195-1214.

Bayard, D., Stähli, M., Parriaux, A., Flühler, H. 2005. The influence of seasonally frozen soil on the snowmelt runoff at two Alpine sites in southern Switzerland. Journal of Hydrology 309(1), 66-84.

Beck, P.S., Atzberger, C., Høgda, K.A., Johansen, B., Skidmore, A.K., 2006. Improved monitoring of vegetation dynamics at very high latitudes: A new method using MODIS NDVI. Remote Sensing of Environment, 100(3), 321-334.

Bergen, J.D., 1968. Some observations on temperature profiles of a mountain snow cover. Res. Note RM-110. Rocky Mountain Forest and Range Experiment Station, Forest Service, U.S. Dept. of Agriculture.

Blöschl, G., Kirnbauer, R., Gutknecht, D., 1991. Distributed snowmelt simulations in an alpine catchment: 1. Model evaluation on the basis of snow cover patterns. Water Resources Research, 27(12): 3171-3179.

Bohn, T.J., Livneh, B., Oyler, J.W., Running, S.W., Nijssen, B., Lettenmaier, D.P., 2013. Global evaluation of MTCLIM and related algorithms for forcing of ecological and hydrological models. Agricultural and Forest Meteorology, 176: 38-49.

Bookhagen, B., Burbank, D.W., 2010. Toward a complete Himalayan hydrological budget: Spatiotemporal distribution of snowmelt and rainfall and their impact on river discharge. Journal of Geophysical Research, 115, F03019, doi:10.1029/2009JF001426.

Bras, R.L., 1990. Hydrology: An Introduction to Hydrologic Science. Addison-Wesley, Reading, Massachusetts, 643 pp.

Brown, J., 1966. Influence of vegetation on permafrost, In: Woods, K.B. (Ed.), Permafrost International Conference, National Academy of Sciences-National Research Council, NRC Div. Bldg., Ottawa, Canada, 6 pp.

Brubaker, K., Rango, A., Kustas, W., 1996. Incorporating radiation inputs into the snowmelt runoff model. Hydrological Processes, 10(10): 1329-1343.

Butcher, P.J., 2009. Incoporating radiation inputs into an operational snowmelt model. Graduate Theses and Dissertations, Paper 10694, Iowa State University, Ames, IA.

Campbell, J.L., Ollinger, S.V., Flerchinger, G.N., Wicklein, H., Hayhoe, K., Bailey, A.S., 2010. Past and projected future changes in snowpack and soil frost at the Hubbard Brook Experiment Forest, New Hampshire, USA. Hydrological Processes, 24, 2465-2480.

Carey, S.K., Woo, M.-k., 2005. Freezing of subarctic hillslopes, Wolf Creek Basin, Yukon, Canada. Arctic, Antarctic, and Alpine Research, 37(1), 1-10.

Carroll, T., Cline, D., Fall, G., Nilsson, A., Li, L., Rost, A., 2001. NOHRSC operations and the simulation of snow cover properties for the conterminous US. In: Proceedings of the 69th Annual Western Snow Conference, April 2001, Sun Valley, ID.

Cazorzi, F., Dalla Fontana, G., 1996. Snowmelt modelling by combining air temperature and a distributed radiation index. Journal of Hydrology, 181(1–4): 169-187.

Chen, R.S., Kang, E.S., Ji, X.B., Yang, Y., Zhang, Z.H., Qing, W.W., Bai, S.Y, Wang, L.D., Kong, Q.Z, Lei, Y.H, Pei, Z.X., 2007. Preliminary study of the hydrological processes in the alpine meadow and permafrost regions at the headwaters of Heihe River. Journal of Glaciology and Geocryology, 29(3), 387-396.

Cherkauer, K.A., Lettenmaier, D.P., 1999. Hydrologic effects of frozen soils in the upper Mississippi River basin. Journal of Geophysical Research, 104(D16): 19599-19610.

Chow, V.T., 1959. Open Channel Hydraulics. McGraw-Hill Book Company Inc., New York City, New York.

Colbeck, S. C. 1974. The capillary effects on water percolation in homogeneous snow. Journal of Glaciology. Vol. 13. No. 67. pp. 119-123.

Colbeck, S. C., Anderson, E. A. 1982. The permeability of a melting snow cover. Water Resources Research. Vol. 18, No. 4. pp. 904-908

Crawford, T.M., Duchon, C.E., 1999. An improved parameterization for estimating effective atmospheric emissivity for use in calculating daytime downwelling longwave radiation. Journal of Applied Meteorology, 38: 474-480.

Daly, S., Davis, R., Ochs, E., Pangburn, T., 2000. An approach to spatially distributed snow modelling of the Sacramento and San Joaquin basins, California. Hydrological processes, 14(18): 3257-3271.

De Roo, A., Odijk, M., Schmuck, G., Koster, E., Lucieer, A., 2001. Assessing the effects of land use changes on floods in the Meuse and Oder catchment. Physics and Chemistry of the Earth, Part B: Hydrology, Oceans and Atmosphere, 26(7), 593-599.

DeWalle, D.R., Rango, A., 2008. Principles of snow hydrology. Cambridge University Press.

Diebold, C.H., 1938. The effects of vegetation upon snow cover and frost penetration during the March 1936 floods. Journal of Forestry, 36(11), 1131-1137.

Doherty, J., Brebber, L., Whyte, P., 1994. PEST: Model-independent parameter estimation. Watermark Computing, Corinda, Australia, 122.

Downer, C.W., Ogden, F.L., 2004. GSSHA: Model to simulate diverse stream flow producing processes. Journal of Hydrologic Engineering, 9(3): 161-174.

Downer, C.W., Ogden, F.L., 2006. Gridded Surface Subsurface Hydrologic Analysis (GSSHA) User's Manual; Version 1.43 for Watershed Modeling System 6.1 (No. ERDC/CHL-SR-06-1). Engineer Research and Development Center, Coastal and Hydraulics Laboratory, Vicksburg, MS.

Downer, C.W., Ogden, F.L., Niedzialek, J.M., Liu, S., 2006. Gridded Surface/Subsurface Hydrologic Analysis (GSSHA) model: A model for simulating diverse streamflow producing processes. In: Singh, V.P. and Frevert, D.K. (eds) Watershed Models. Taylor & Francis, CRC Press, Boca Raton, FL, pp. 131-157.

Downer, C. W., 2007. Development of a Simple Soil Moisture Model in the Hydrologic Simulator GSSHA, ERDC-TN-SWWRP-07-8, U.S. Army Engineer Research and Development Center, Vicksburg, MS.

Dozier, J., Marks, D., 1987. Snow mapping and classification from Landsat Thematic Mapper data. Annals of Glaciology, 9(1): 97-103.

Duffie, J.A., Beckman, W.A., 1980. Solar engineering of thermal processes. Wiley, New York.

Dun, S., Wu, J., McCool, D., Frankenberger, J., Flanagan, D., 2010. Improving frost-simulation subroutines of the Water Erosion Prediction Project (WEPP) model. Transactions of the ASABE, 53(5), 1399-1411.

Dunn, S., Colohan, R., 1999. Developing the snow component of a distributed hydrological model: a step-wise approach based on multi-objective analysis. Journal of Hydrology, 223(1): 1-16.

Dunne, T., Black, R.D., 1970a. An experimental investigation of runoff production in permeable soils. Water Resources Research, 6(2), 478-490.

Dunne, T., Black, R.D., 1970b. Partial area contributions to storm runoff in a small New England watershed. Water Resources Research, 6(5), 1296-1311.

Dunne, T., Black, R.D., 1971. Runoff processes during snowmelt. Water Resour. Res., 7, 1160–1172.

Eagleson, P.S., 1970. Dynamic Hydrology. McGraw-Hill, New York.

ERDAS, I., 1999. ERDAS Field Guide. Atlanta, Georgia, 672: 94.

Essery, R., Rutter, N., Pomeroy, J., Baxter, R., Stähli, M., Gustafsson, D., Barr, A., Bartlett, P., Elder, K., 2009. SnowMIP2: An evaluation of forest snow process simulations. Bulletin of the American Meteorological Society, 90(8): 1120-1135.

Etchevers, P., Martin, E., Brown, R., Fierz, C., Lejeune, Y., Bazile, E., Boone, A., Dai, Y.-J., Essery, R., Fernandez, A., Gusev, Y., Jordan, R., Koren, V., Kowalczyk, E., Nasonova, N.O., Pyles, R.D., Schlosser, A., Shmakin, A.B., Smirnova, T.G., Strasser, U., Verseghy, D., Yamazaki, T., Yang, Z.-L, 2004. Validation of the energy budget of an alpine snowpack simulated by several snow models (SnowMIP project). Annals of Glaciology, 38(1): 150-158.

Fahey, T.J., Lang, G.E., 1975. Concrete frost along an elevational gradient in New Hampshire. Canadian Journal of Forest Research, 5(4), 700-705

Farouki, O.T., 1981. The thermal properties of soils in cold regions. Cold Regions Science and Technology, 5(1), 67-75.

Fassnacht, S. R., and Soulis, E. D. 2002. Implications during transitional periods of improvements to the snow processes in the land surface scheme-hydrological model WATCLASS. *Atmosphere-Ocean*, *40*(4), 389-403.

Fassnacht, S. R., Venable, N. B. H., Khishigbayar, J., and Cherry, M. L., 2013. The probability of precipitation as snow derived from daily air temperature for high elevation areas of Colorado, United States. *IAHS-AISH publication*, 65-70.

Fassnacht, S. R., López-Moreno, J. I., Ma, C., Weber, A. N., Pfohl, A. K. D., Kampf, S. K., and Kappas, M., 2017. Spatio-temporal snowmelt variability across the headwaters of the Southern Rocky Mountains. Front. Earth Sci., 11(3), 505-514.

Fatichi S, Vivoni ER, Ogden FL, Ivanov VY, Mirus B, Gochis D, Downer CW, Camporese M, Davison JH, Ebel B, Jones N., 2016. An overview of current applications, challenges, and future trends in distributed process-based models in hydrology. Journal of Hydrology, 537, 45-60.

Flerchinger, G., Saxton, K.E., 1989. Simultaneous heat and water model of a freezing snow-residue-soil system I, theory and development. Transactions of the ASAE, 32(2), 565-571.

Follum, M.L., Downer, C.W., 2013. Snow Water Equivalent Modeling Capabilities of the GSSHA Watershed Model. U.S. Army Corps of Engineers, Coastal and Hydraulic Laboratory Technical Report 13-4, Vicksburg, MS.

Follum, M.L., Downer, C.W., Niemann, J.D., 2014. Simulating the spatial distribution of snow pack and snow melt runoff with different snow melt algorithms in a physics based watershed model. AGU Fall Meeting, American Geophysical Union, San Francisco, CA.

Follum, M.L., Downer, C.W., Niemann, J. D., Roylance, S. M., and Vuyovich, C. M., 2015. A radiation-derived temperature-index snow routine for the GSSHA hydrologic model. J. Hydrol., 529, 723–736.

Follum, M.L., Tavakoly, A. A., Niemann, J. D., and Snow, A. D., 2017. AutoRAPID: A model for prompt streamflow estimation and flood inundation mapping over regional to continental extents. *JAWRA*, *53*(2), 280-299.

Follum, M.L., Niemann, J.D., Parno, J.T., Downer, C.W., 2018. A simple temperature-based method to estimate heterogeneous frozen ground within a distributed watershed model. Hydrology and Earth System Sciences, 22(5), 2669.

Fox, J.D., 1992. Incorporating freeze-thaw calculations into a water balance model. Water Resources Research, 28(9), 2229-2244.

Franz, K.J., Hogue, T.S., Sooroshian, S., 2008. Operational snow modeling: Addressing the challenges of an energy balance model for National Weather Service forecasts. Journal of Hydrology, 360(1): 48-66.

Fry, J.A., Xian, G., Jin, S., Dewitz, J.A., Homer, C.G., Limin, Y., Barnews, C.A., Helold, N.D., Wickham, J.D., 2011. Completion of the 2006 national land cover database for the conterminous United States. Photogrammetric Engineering and Remote Sensing, 77(9): 858-864.

Gerdel, R.W., 1954. The transmission of water through snow. Transactions American Geophysical Union, 35(3),: 475-485.

Gesch, D., Oimoen, M., Greenlee, S., Nelson, C., Steuck, M., Tyler, D., 2002. The national elevation dataset. Photogrammetric engineering and remote sensing, 68(1): 5-32.

Green, W., Ampt, G., 1911. Studies on soil physics. The Journal of Agricultural Science, 4(01), 1-24.

Gustafson, J.R., Brooks, P.D., Molotch, N.P., Veatch, W.C., 2010. Estimating snow sublimation using natural chemical and isotropic tracers across a gradient of solar radiation. Water Resources Research, 46(12), 1-14.

Harding, R. J., Pomeroy, J.W., 1996. The energy balance of the winter boreal landscape. J. Climate, 9, 2778-2787.

Hargreaves, G.H., Samani, Z.A., 1985. Reference crop evapotranspiration from temperature. Applied Engineering Agriculture, 1(2): 96-99.

He M., Hogue T.S., Margulis S.A., Franz K.J., 2012. An integrated uncertainty and ensemble-based data assimilation approach for improved operational streamflow predictions. Hydrology and Earth System Sciences, 16(3), 815-31.

He M., Hogue T.S., Franz K.J., Margulis S.A., Vrugt J.A., 2011. Characterizing parameter sensitivity and uncertainty for a snow model across hydroclimatic regimes. Advances in Water Resources, 34(1): 114-27.

Henneman, H.E., Stefan, H.G., 1999. Albedo models for snow and ice on a freshwater lake. Cold Regions Science and Technology, 29(1): 31-48.

Hock, R., 1999. A distributed temperature-index ice-and snowmelt model including potential direct solar radiation. Journal of Glaciology, 45(149): 101-111.

Hock, R., 2003. Temperature index melt modelling in mountain areas. Journal of Hydrology, 282(1–4): 104-115.

Idso, S.B., 1981. A set of equations for full spectrum and 8- to 14-µm and 10.5- to 12.5-µm thermal radiation from cloudless skies. Water Resources Research, 17(2): 295-304.

Jansson, P.E., 2001. Coupled heat and mass transfer model for soil-plant-atmosphere systems.

Jansson, P.E., Karlberg, L., 2010. Coupled heat and mass transfer model for soil-plant-atmosphere systems. Royal Institute of Technology, Stockholm, p. 454.

Jin M., Liang S., 2006. An improved land surface emissivity parameter for land surface models using global remote sensing observations. Journal of Climate, (12): 2867-81.

Johansen, O., 1977. Thermal conductivity of soils. CRREL-TL-637, Cold Regions Research and Engineering Laboratory, Hanover, NH.

Johnson, C.W., McArthur, R.P., 1973. Winter storm and flood analyses, northwest interior. Hydraulic Engineering and the Environment. ASCE, pp. 359-369.

Jordan, R., 1991. A one-dimensional temperature model for a snow cover: technical documentation for SNTHERM 89. U.S. Army Corps of Engineers, Cold Regions Research and Engineering Laboratory. Hanover, NH.

Jost, G., Weiler, M., Gluns, D.R., Alila, Y., 2007. The influence of forest and topography on snow accumulation and melt at the watershed-scale. Journal of Hydrology, 347(1), 101-115.

Jost, G., Moore, R., Smith, R., Gluns, D., 2012. Distributed temperature-index snowmelt modelling for forested catchments. Journal of Hydrology, 420-421: 87–101.

Julien, P. Y., Saghafian, B. 1991. A two-dimensional watershed rainfall-runoff model – CASC2D User's Manual. Colorado State Univ. 70 pp.

Kang, D.H., 2005. Distributed snowmelt modeling with GIS and CASC2D at California Gulch, Colorado. Colorado State University, Fort Collins, CO, 195 pp.

Kennedy, I., Sharratt, B., 1998. Model comparisons to simulate soil frost depth. Soil Science, 163(8), 636-645.

Kirnbauer, R., Bloeschl, G., Gutknecht, D., 1994. Entering the era of distributed snow models. Nordic Hydrology, 25(1): 1-24.

Koren, V., Schaake, J., Mitchell, K., Duan, Q.Y., Chen, F., Baker, J.M., 1999. A parameterization of snowpack and frozen ground intended for NCEP weather and climate models. Journal of Geophysical Research: Atmospheres (1984–2012), 104(D16), 19569-19585.

Kumar, M., Marks, D., Dozier, J., Reba, M., Winstral, A., 2013. Evaluation of distributed hydrologic impacts of temperature-index and energy-based snow models. Advances in Water Resources, 56: 77-89.

Kurganova, I., Teepe, R., Loftfield, N., 2007. Influence of freeze-thaw events on carbon dioxide emission from soils at different moisture and land use. Carbon Balance and Management, 2: 1-2.

Kustas, W.P., Rango, A., Uijlenhoet, R., 1994. A simple energy budget algorithm for the snowmelt runoff model. Water Resources Research, 30(5): 1515-1527.

Landry, C.C., Buck, K.A., Raleigh, M.S., Clark, M.P., 2014. Mountain system monitoring at Senator Beck Basin, San Juan Mountains, Colorado: A new integrative data source to develop and evaluate models of snow and hydrologic processes. Water Resources Research, 50(2): 1773-1788.

Lei, F., Koren, V., Smith, M., Moreda, F., 2007. A sensitivity study of an energy budget snow accumulation and ablation model. In: Paper J.6.4, American Meteorological Society, San Antonio, TX.

Lin, C., McCool, D., 2006. Simulating snowmelt and soil frost depth by an energy budget approach. Transactions of the ASABE, 49(5), 1383-1394.

Lindstrom, G., Bishop, K., Lofvenius, M.O., 2002. Soil frost and runoff at Svartberget, northern Sweden—measurements and model analysis. Hydrological Processes, 16, 3379–3392.

Liou, K.N., 2002. An introduction to atmpospheric radiation, second edition. Academic Press, New York.

Liston, G.E., Elder, K., 2006. A distributed snow-evolution modeling system (SnowModel). Journal of Hydrometeorology, 7(6): 1259-1276.

Luce, C.H., Tarboton, D.G., Cooley, K.R., 1998. The influence of the spatial distribution of snow on basin-averaged snowmelt. Hydrological Processes, 12(1011): 1671-1683.

Lundberg, A., Halldin, S., 1994. Evaporation of intercepted snow: analysis of governing factors. Wat. Resour. Res., 30, 2587-2598.

Lundquist, J.D., Dickerson-Lange, S.E., Lutz, J.A., Cristea, N.C., 2013. Lower forest density enhances snow retention in regions with warmer winters: A global framework developed from plot-scale observations and modeling. Water Resources Research, 49(10): 6356-6370.

MacKinney, A., 1929. Effects of forest litter on soil temperature and soil freezing in autumn and winter. Ecology, 10(3), 312-321.

McNamara, J.P., Kane, D.P., Hinzman, L.D., 1997. Hydrograph separation in an Arctic watershed using mixing model and graphical techniques. Water Resources Research, 33, 1707-1719.

Mhawej, M., Faour, R., Fayad, A., Shaban, A., 2014. Towards an enhanced method to map snow cover areas and derive snow-water equivalent in Lebanon. Journal of Hydrology, 513: 274–282.

Molnau, M., Bissell, V.C., 1983. A continuous frozen ground index for flood forecasting. Proceedings 51st Annual Meeting Western Snow Conference, Canadian Water Resources Association, Cambridge, Ontario, 109-119.

Molotch, N.P., Bales, R.C., 2006. Comparison of ground-based and airborne snow surface albedo parameterizations in an alpine watershed: Impacts on snowpack mass balance. Water Resources Research, 42(5): WR05410, doi:10.1029/2005WR004522.

Monteith, J., 1965. Evaporation and environment. Symposia of the Society for Experimental Biology, 4.

Monteith, J., 1981. Evaporation and surface temperature. Quarterly Journal of the Royal Meteorological Society, 107(451), 1-27.

Musselman, K., Molotch, N.P., Brooks, P.D., 2008. Effects of vegetation on snow accumulation and ablation in a mid-latitude sub-alpine forest. Hydrological Processes, 22(15), 2767-2776.

Nash, J.E., Sutcliffe, J.V., 1970. River flow forecasting through conceptual models part I — A discussion of principles. Journal of Hydrology, 10(3): 282-290.

National Centers for Environmental Information (NCEI), https://www.ncdc.noaa.gov/.

Nikolaev, I.V., Leong, W.H., Rosen, M.A., 2013. Experimental investigation of soil thermal conductivity over a wide temperature range. International Journal of Thermophysics, 34(6), 1110-1129.

Nyberg, L., Stähli, M., Mellander, P.E., Bishop, K., 2001. Soil frost effects on soil water and runoff dynamics along a boreal forest transact: 1. Field investigations. Hydrological Processes, 15, 909–926.

Ogden, F.L., Saghafian, B., 1997. Green and Ampt infiltration with redistribution. Journal of Irrigation and Drainage Engineering, 123(5), 386-393.

Ohmura, A., 2001. Physical basis for the temperature-based melt index method. J. Appl. Meteorol. 40, 753–761.

Painter, T.H., Barrett, A.P., Landry, C.C., Neff, J.C., Cassidy, M.P., Lawrence, C.R., McBride, K.E., Lang, G., 2007. Impact of disturbed desert soils on duration of mountain snow cover. Geophysical Research Letters, 34(12).

Painter, T.H., Skiles, S.M., Deems, J.S., Brandt, W.T. and Dozier, J., 2018. Variation in rising limb of Colorado River snowmelt runoff hydrograph controlled by dust radiative forcing in snow. *Geophysical Research Letters*, *45*(2), pp.797-808.

Pearson, G.A., 1920. Factors controlling the distribution of forest types, Part I. Ecology, 1(3), 139-159.

Pomeroy, J.W., 1988. Wind Transport of Snow, PhD Thesis, University of Saskatchewan.

Pomeroy, J.W., Gray, D.M., 1995. Snowcover accumulation, relocation and management. National Hydrology Research Institute Science Report No. 7. NHRI, Environment Canada, Saskatoon, 144 pp.

Pomeroy, J.W., Gray, D., Hedstrom, N., Janowicz, J., 2002. Prediction of seasonal snow accumulation in cold climate forests. Hydrological Processes, 16(18): 3543-3558.

Pomeroy, J.W., Marks, D., Link, T., Ellis, C., Hardy, J., Rowlands, A., Granger, R., 2009. The impact of coniferous forest temperature on incoming longwave radiation to melting snow. Hydrological Processes, 23(17): 2513-2525.

Pomeroy, J.W., Parviainen, J., Hedstrom, N., Gray, D.M., 1998. Coupled modelling of forest snow interception and sublimation. Hydrol. Process., 12: 2317-2337. doi:10.1002/(SICI)1099-1085(199812)12:15<2317::AID-HYP799>3.0.CO;2-X

Pomeroy, J.W., Schmidt, R.J., 1993. The use of fractal geometry in modelling intercepted snow accumulation and sublimation. in Proc. Eastern Snow Conference, Vol. 50, pp. 1-10.

Prata, A.J., 1996. A new long-wave formula for estimating downward clear-sky radiation at the surface. Quarterly Journal of the Royal Meteorological Society, 122(533): 1127-1151.

Prèvost, M., Barry, R., Stein, J., Plamondon, A.P., 1990. Snowmelt runoff modelling in a balsam fir forest with variable source are simulator (VSAS2). Water Resources Research, 25(5), 1067-1077.

Rango, A., Martinec, J. 1995. Revisiting the degree-day method for snowmelt computations. Journal of the American Water Resources Association. Vol. 31, No. 4. Pp. 657-669.

Rawls, W., Brakensiek, D., Saxton, K., 1982. Estimation of soil water properties. Transactions of the ASAE, 25(5), 1316-1320.

Rawls, W.J., Brakensiek, D., 1985 Prediction of soil water properties for hydrologic modelling, In: Watershed Management in the Eighties, ASCE, 293-299.

Rawls, W.J., Brakensiek, D.L., Miller, N., 1983. Green-Ampt infiltration parameters from soils data. Journal of Hydraulic Engineering, 109(1), 62-70.

Rekolainen, S., Posch, M., 1993. Adapting the CREAMS model for Finnish conditions. Hydrology Research, 24(5), 309-322.

Ricard, J.A., Tobiasson, W., Greatorex, A., 1976. The field assembled frost gage. United States Army Cold Regions Research and Engineering Laboratory, Hanover, NH.

Rinehart, A.J., Vivoni, E.R., Brooks, P.D., 2008. Effects of vegetation, albedo, and solar radiation sheltering on the distribution of snow in the Valles Caldera, New Mexico. Ecohydrology, 1(3), 253-270.

Rittger, K., Painter, T.H., Dozier, J., 2013. Assessment of methods for mapping snow cover from MODIS. Advances in Water Resources, 51: 367-380.

Sade, R., Rimmer, A., Litaor, M.I., Shamir, E., Furman, A., 2014. Snow surface energy and mass balance in a warm temperate climate mountain. Journal of Hydrology, 519: 848-862.

Sartz, R.S., 1973. Effect of forest cover removal on depth of soil freezing and overland flow. Soil Science Society of America Journal, 37(5), 774-777.

Scharffenberg, W.A. and Fleming, M.J., 2006. Hydrologic modeling system HEC-HMS: User's manual. US Army Corps of Engineers, Hydrologic Engineering Center.

Shamir, E., Georgakakos, K.P., 2006. Distributed snow accumulation and ablation modeling in the American River Basin. Advances in Water Resources, 29(4): 558-570.

Shanley, J.B., 2000. Sleepers River, Vermont: A water, energy, and biogeochemical budgets program site. Fact Sheet-166-99, U.S. Department of the Interior, U.S. Geological Survey.

Shanley, J.B., Chalmers, A., 1999. The effect of frozen soil on snowmelt runoff at Sleepers River, Vermont. Hydrological Processes, 13(13), 1843-1857.

Shanley, J.B., Sundquist, E.T., Kendall, C., 1995. Water, energy, and biogeochemical budget research at Sleepers River Research Watershed, Vermont. No. 2331-1258, U.S. Geological Survey, Open-File Reports Section [distributor].

Sharif, H.A., Sparks, L., Hassan, A.A., Zeitler, J., Xie, H., 2010. Application of a distributed hydrologic model to the November 17, 2004, Flood of Bull Creek Watershed, Austin, Texas. Journal of Hydrologic Engineering, 15(8): 651-657.

Shuttleworth, W.J., 1993. Evaporation. In: Maidment, D.R. (Ed.), Handbook of Hydrology. McGraw-Hill Inc., New York, pp. 4.6 and 4.31.

Sicart, J.E., Pomeroy, J.W., Essery, R.L.H., Hardy, J., Link, T., Marks, D., 2004. A sensitivity study of daytime net radiation during snowmelt to forest canopy and atmospheric conditions. Journal of Hydrometeorology, 5: 774-784.

Sicart, J.E., Pomeroy, J.W., Essery, R.L.H., Bewley, D., 2006. Incoming longwave radiation to melting snow: observations, sensitivity and estimation in northern environments. Hydrological Processes, 20: 3697-3708.

Singh, P. Spitzbart, G., Hübl, H., Weinmeister, H.W., 1997. Hydrological response of snowpack under rain-on-snow events: a field study. Journal of Hydrology, 202(1): 1-20.

Skiles, S.M., Painter, T.H., Deems, J.S., Bryant, A.C., Landry, C.C., 2012. Dust radiative forcing in snow of the Upper Colorado River Basin: 2. Interannual variability in radiative forcing and snowmelt rates. Water Resources Research, 48(7): W07522.

Skiles, S.M., Painter, T.H., Belnap, J., Holland, L., Reynolds, R.L., Goldstein, H.L., Lin, J., 2015. Regional variability in dust-on-snow processes and impacts in the Upper Colorado River Basin. Hydrologic Processes. doi: 10.1002/hyp.10569.

Skiles, S.M., Painter, T.H., Belnap, J., Holland, L., Reynolds, R.L., Goldstein, H.L., Lin, J., 2015. Regional variability in dust-on-snow processes and impacts in the Upper Colorado River Basin. Hydrologic Processes. doi: 10.1002/hyp.10569.

Smith, J.A., 1993. Precipitation. In: Maidment, D.R. (Ed.), Handbook of hydrology. McGraw-Hill Inc., New York, pp. 3.4.

Snow, A.D., Christensen, S.D., Swain, N.R., Nelson, E.J., Ames, D.P., Jones, N.L., Ding, D., Noman, N.S., David, C.H., Pappenberger, F. and Zsoter, E., 2016. A high-resolution national-scale hydrologic forecast system from a global ensemble land surface model. *JAWRA*, *52*(4), 950-964.

Stähli, M., 2017. Hydrological significance of soil frost for pre-alpine areas. Journal of Hydrology, 546, 90-102.

Stähli, M., Jansson, P-E., Lundin, L-C., 1999. Soil moisture redistribution and infiltration in frozen sandy soils. Water Resources Research 35(1), 95-103.

Stoner, J.D., Lorenz, D.L., Wiche, G.J., Goldstein, R.M., 1993. Red river of the north basin, Minnesota, North Dakota, and South Dakota. Journal of the American Water Resources Association, 29(4): 575-615.

Tou, J.T., Gonzalez, R.C., 1974. Pattern recognition principles. Pattern Recognition in Physics, 1.

TVA, 1972. Heat and mass transfer between a water surface and the atmosphere. Tennessee Valley Authority, Norris, TN.

USACE, 1956. Snow hydrology, summary report of the snow investigations. U.S. Army Corps of Engineers, North Pacific Division, Portland, OR.

Van Der Knijff, J., Younis, J., De Roo, A., 2010. LISFLOOD: a GIS-based distributed model for river basin scale water balance and flood simulation. International Journal of Geographical Information Science, 24(2), 189-212.

Vermette, S., Christopher, S., 2008. Using the rate of accumulated freezing and thawing degree days as a surrogate for determining freezing depth in a temperate forest soil. Middle States Geographer, 41, 68-73.

Vermette, S., Kanack, J., 2012. Modeling frost line soil penetration using freezing degree-day rates, day length, and sun angle. 69th Eastern Snow Conference, Frost Valley YMCA, Claryville, NY, USA.

Veatch, W., Brooks, P.D., Gustafson, J.R., Molotch, N.P., 2009. Quantifying the effects of forest canopy cover on net snow accumulation at a continental, mid-latitude site. Ecohydrology, 2(2), 115-128.

Vuyovich, C., Jacobs, J.M., 2011. Snowpack and runoff generation using AMSR-E passive microwave observations in the Upper Helmand Watershed, Afghanistan. Remote Sens. Environ. 115 (12), 3313–3321.

Wahl, K., 1992. Evaluation of trends in runoff in the western United States. Managing Water Resources during Global Change: 701-710.

Wahl, M, Follum M, Snow A, Tavakoly A., 2016. Developing hydrologic awareness. The Military Engineer, 108 (700).

Walter M.T., Brooks E.S., McCool D.K., King L.G., Molnau M., Boll J., 2005. Process-based snowmelt modeling: does it require more input data than temperature-index modeling?. Journal of Hydrology, 300(1-4): 65-75.

Wang, Q., Adiku, S., Tenhunen, J., Granier, A., 2005. On the relationship of NDVI with leaf area index in a deciduous forest site. Remote Sensing of Environment, 94(2), 244-255, 2005.

Webb, R.W., 2017. Using ground penetrating radar to assess the variability of snow water equivalent and melt in a mixed canopy forest, Northern Colorado. Frontiers of Earth Science. 11(3), 482-495.

Webster, C., Rutter, N., Jonas, T., 2017. Improving representation of canopy temperatures for modeling subcanopy incoming longwave radiation to the snow surface. Journal of Geophysical Research: Atmospheres 122(17), 9154-9172.

Wilcox, B.P., Newman, B.D., Brandes, D., Davenport, D.W., Reid, K., 1997. Runoff from a semiarid ponderosa pine hillslope in New Mexico. Water Resources Research, 33(10), 2301-2314.

Willis, W., Carlson, C., Alessi, J., Haas, H., 1961. Depth of freezing and spring run-off as related to fall soil-moisture level. Canadian Journal of Soil Science, 41(1), 115-123.

Woo, M., 1986. Permafrost hydrology in North America,.Atmos. Ocean., 24, 201–234.

Woo, M., Arain, M., Mollinga, M., and Yi, S., 2004. A two directional freeze and thaw algorithm for hydrologic and land surface modelling. Geophys. Res. Lett., 31, L12501, https://doi.org/10.1029/2004GL019475.

Wright, D.B., Smith, J.A., Baeck, M.L., 2014. Flood frequency analysis using radar rainfall fields and stochastic storm transposition. Water Resour. Res. 50 (2), 1592–1615.

Zanotti, F., Endrizzi, S., Bertoldi, G., Rigon, R., 2004. The GEOTOP snow module. Hydrol. Process. 18 (18), 3667–3679.

Zeinivand, H., De Smedt, F., 2009. Hydrological modeling of snow accumulation and melting on river basin scale. Water Resour. Management 23, 2271–2287.

Zhang, T., Barry, R.G., Armstrong, R.L., 2004. Application of satellite remote sensing techniques to frozen ground studies. Polar Geography 28:163–196.

Zhao, L., Gray, D.M., 1999. Estimating snowmelt infiltration into frozen soils. Hydrol. Process. 13, 1827-1842.

Zhenniang, Y., Fungzian, L., Zhihuai, Y., Qiang, W., 1994. The effect of water and heat on hydrological processes of a high alpine permafrost area. In Snow and Ice Covers: Interactions with the Atmosphere and Ecosystems, IAHS Publication 223, ed. E.G. Jones, T.D. Davies, A. Ohmura, and E.M. Morris, pp. 259-268.

APPENDIX

A list of symbols with descriptions is provided below. Because this dissertation includes three journal papers (Chapters 2, 3, and 4) some symbols do not have the same meaning in all of the chapters. Therefore, the numbers under the Chapter heading indicate the chapter(s) where that symbol is used. Blank spaces under the Chapter heading indicate that the symbol is valid for all chapters.

Symbol	Chapter	Description
A		daily decay coefficient
A_{obs}		the total observed snow covered area
A_{over}		area where the model predicts snow cover but no snow is observed
A_s		area of the cell covered by snow (fraction)
A_{TI}	[3, 4]	antecedent temperature index (°C)
A_{TIPM}	[3, 4]	antecedent snow temperature index parameter (fraction)
A_{under}		area where the model predicts no snow cover but snow is observed
A_v		seasonal melt adjustment
ATI	[2]	antecedent temperature index (°C)
D_{gc}		depth of ground cover (cm).
D_s		snow depth (cm)
E	[3]	excess water within the snowpack (mm)
E_c	[3, 4]	elevation of a cell (m)
E_g	[3, 4]	elevation of the temperature gage (m)
E_l		hourly lagged excess liquid water available during time step (mm)
$Elev_c$	[2]	elevation of a cell (m)
$Elev_g$	[2]	elevation of the temperature gage (m)

Symbol	Chapter	Description
F		frozen ground index (°C-days)
F_c		canopy cover (fractional)
$F_{threshold}$		frozen ground index when ground is considered frozen (°C-days)
H	[3]	thickness of the saturated layer at bottom of snowpack (m)
H	[4]	soil thickness (m)
JD		Julian day
K	[2]	reduction in the shortwave radiation (fraction) due to distance from the earth to the sun (K_r), atmospheric scattering (K_{atm}), absorption by clouds (K_c), vegetation (K_v), slope/aspect of terrain (K_s), and topographic shading (K_t)
K_{gc}		ground cover reduction coefficient (cm^{-1})
K_s	[4]	snow reduction coefficient (cm^{-1})
K_v	[3, 4]	vegetation transmission coefficient (fraction)
L		lag time for excess water to begin leaving the snowpack (hr)
L_{AI}	[3, 4]	leaf area index (m^2 m^{-2})
L_h	[3, 4]	liquid water holding capacity (fraction)
LAI	[2]	leaf area index (m^2 m^{-2})
$LW_\downarrow$	[2]	downwelling longwave radiation (W m^{-2})
$LW_\uparrow$	[2]	outgoing longwave radiation (W m^{-2})
$LW_{\downarrow,toc}$		downwelling longwave radiation at the top of canopy (W m^{-2})
M		melt amount (mm)
M_f		melt factor (mm °C^{-1} dt^{-1})
$M_{f,max}$		maximum melt factor (mm °C^{-1} (6 hr)$^{-1}$)
$M_{f,min}$		minimum melt factor (mm °C^{-1} (6 hr)$^{-1}$)

Symbol	Chapter	Description
$MBASE$	[2]	temperature above which snow begins to melt (°C)
N		cloud cover (fraction)
$N_{Mf,max}$	[3, 4]	maximum negative melt factor (mm $°C^{-1}$ $(6\ hr)^{-1}$)
NMF		negative melt factor (mm $°C^{-1}$ dt^{-1})
NMF_{max}	[2]	maximum negative melt factor (mm $°C^{-1}$ $(6\ hr)^{-1}$)
P	[2]	precipitation (mm)
P	[3, 4]	precipitation (m hr^{-1})
P_a		atmospheric pressure (mb)
P_{eff}		effective precipitation (m hr^{-1})
$PLWHC$	[2]	liquid water holding capacity (fraction)
$PXTEMP$	[2]	temperature at which precipitation is considered snow (°C)
Q		heat flux (W m^{-2})
Q_{ground}		ground heat flux (W m^{-2})
Q_{latent}		latent heat flux (W m^{-2})
$Q_{longwave}$		net longwave radiation (W m^{-2})
Q_{melt}		advected heat removed by meltwater (W m^{-2})
$Q_{precipitation}$		advected heat from precipitation (W m^{-2})
$Q_{sensible}$		sensible heat flux (W m^{-2})
$Q_{shortwave}$	[1]	net shortwave radiation (W m^{-2})
R		withdrawal rate for meltwater to leave the snowpack (hr^{-1})
R_a		available energy at the snow surface (W m^{-2})
$R_{LW\downarrow}$	[3, 4]	downwelling longwave radiation (W m^{-2})
$R_{LW\uparrow}$	[4]	outgoing longwave radiation (W m^{-2})
$R_{SW,0}$	[3, 4]	solar constant (1366 W m^{-2} from Liou, 2002)

Symbol	Chapter	Description
$R_{SW,net}$	[3, 4]	net shortwave radiation (W m^{-2})
$R_{SW\downarrow,flat}$		daily shortwave radiation for a flat cell on a cloud-free day (W m^{-2})
S_0	[2]	solar constant (1366 W m^{-2} from Liou, 2002)
S_{cf}	[3, 4]	under-catch adjustment factor (fraction)
S_l		previously stored excess liquid water held within the snowpack (mm)
S_{sub}		sublimation rate (cm hr^{-1})
$S_{sub,d}$		watershed-average daily maximum sublimation amount (cm d^{-1})
S_v		seasonal melt adjustment
SCF	[2]	under-catch adjustment factor (fraction)
$SW_{\downarrow}$		incident shortwave radiation (W m^{-2})
$SW_{\downarrow,\mathrm{day,noon}}$		shortwave radiation at noon on a flat surface for day of interest (W m^{-2})
$SW_{\downarrow,net}$	[2]	net shortwave radiation (W m^{-2})
$SW_{\downarrow,\mathrm{year,noon}}$		max shortwave radiation at noon on a flat surface over a year (W m^{-2})
T_a		air temperature (°C)
$T_{a,d}$		average daily air temperature (°C)
T_{canopy}		canopy temperature (°C)
T_g		air temperature at a gage (°C)
T_h	[3]	temperature at which precipitation is considered snow (°C)
T_{mbase}	[3, 4]	temperature above which snow begins to melt (°C)
T_{px}	[4]	temperature at which precipitation is considered snow (°C)
T_r		temperature of precipitation (°C)
T_{rad}		radiation-derived proxy temperature (°C)
$T_{rad,d}$		average daily proxy temperature (°C)
T_{sur}		snow surface temperature (°C)

Symbol	Chapter	Description
$TIPM$	[2]	antecedent snow temperature index parameter (fraction)
U		number of degree days in the freezing/thawing period (ºC-days)
W_i		ice portion of the snowpack (mm)
W_q		meltwater held by the snowpack (mm)
Z_d		depth of frozen ground (frost depth) (m)
$Z_{\max}$		maximum frost depth (m)
d		number of days since the last snowfall (days)
dt	[2]	model time step (hr)
e_{sat}		saturated vapor pressure (mb)
ε_{snow}		emissivity of snow (fraction)
g_c		grid cell resolution (m)
f_r		fraction of precipitation in the form of rain (fraction)
f_u		average wind function (mm mb^{-1} $(6\ h)^{-1}$)
k_s	[3]	saturated permeability of the snowpack (25×10^{-10} m^2 based on Colbeck and Anderson (1982))
n_{ch}	[3]	Manning's roughness coefficients for channel flow (s $m^{-1/3}$)
n_{ice}	[4]	amount of ice within soil profile (m^3 m^{-3})
n_{ov}	[3]	Manning's roughness coefficients for overland flow (s $m^{-1/3}$)
n_{total}	[4]	porosity of the soil (m^3 m^{-3})
r_h	[3, 4]	relative humidity (fraction)
rh	[2]	relative humidity (fraction)
q_{snow}		lateral flow of meltwater through the snowpack (m^3 s^{-1})
$q_{x,y}$		overland flow fluxes between cells (m^3 s^{-1})
ΔD_t		change in heat deficit due to temperature gradients (mm of SWE)

Symbol	Chapter	Description
Δt	[3, 4]	model time step (hr)
Φ		downward slope between cells
ϑ	[3]	lapse rate (°C m^{-1})
$\emptyset$	[4]	lapse rate (°C km^{-1})
$\mathit{\Omega}_{dry}$		thermal conductivity of dry soil (J m^{-1} h^{-1} °C^{-1})
$\mathit{\Omega}_{ice}$		thermal conductivity of ice (J m^{-1} h^{-1} °C^{-1})
$\mathit{\Omega}_{m}$		mean thermal conductivity of the frozen/unfrozen soil (J m^{-1} h^{-1} °C^{-1})
$\mathit{\Omega}_{s}$		thermal conductivity of solids within soil (J m^{-1} h^{-1} °C^{-1})
$\mathit{\Omega}_{sat}$		thermal conductivity of saturated soil (J m^{-1} h^{-1} °C^{-1})
$\mathit{\Omega}_{water}$		thermal conductivity of water (J m^{-1} h^{-1} °C^{-1})
α	[2]	albedo of the snowpack (fraction)
α_s	[3, 4]	albedo of the snowpack (fraction)
$\propto$		hydraulic constant for water ($\propto = 5.47 \times 10^6$ m^{-1} s^{-1}, Colbeck (1974))
δ		latent heat of fusion of the soil (J m^{-3})
δ_f		latent heat of fusion of water (0.334 MJ kg^{-1} at 0°C)
ε_a		air emissivity (fraction)
ε_c		canopy emissivity (fraction)
ϵ	[3]	the residuals between simulated and observed values
θ	[2]	lapse rate (°C m^{-1})
θ	[3]	porosity of the snowpack (m^3 m^{-3})
λ		dimensionless coefficient that accounts for changes in sensible heat
ρ		dry soil density (kg m^{-3})
ρ_d		threshold density for destructive metamorphism (gm cm^{-3})
ρ_n		density of newly fallen snow (gm cm^{-3})

Symbol	Chapter	Description
ρ_x		density of the snowpack (gm cm^{-3})
σ		Stefan-Boltzmann Constant ($6.12 \cdot 10^{-10}$ mm K^{-1} hr^{-1}; $5.67 \cdot 10^{-8}$ W m^{-2} K^{-4})
φ	[2]	angle of incidence (radians)
φ	[3, 4]	reduction in the shortwave radiation (fraction) due to distance from the earth to the sun (φ_r), atmospheric scattering (φ_{atm}), absorption by clouds (φ_c), vegetation (φ_v), slope/aspect of terrain ($K\varphi_s$), and topographic shading (φ_t)
ω		soil water content (% of dry weight)